Probing the Surface Interaction Mechanisms of Air Bubbles and Oil Droplets with Hydrophobic Polymers, Asphaltenes and Bitumen

by

Diling Yang

A thesis submitted in partial fulfillment of the requirements for the degree of

Doctor of Philosophy

in

Chemical Engineering

Department of Chemical and Materials Engineering

University of Alberta

Abstract

Interfacial interactions among solid particles, gas bubbles and liquid drops play a critical role in numerous interfacial phenomena and biophysical and industrial processes, such as drug and gene delivery in biological systems, froth flotation and oil/water separation in mining and oil extraction industry. Polymers, asphaltenes, bitumen, gas bubbles, and liquid droplets are commonly involved in numerous engineering processes. It is of both fundamental and practical importance to characterize the interfacial interaction mechanisms of these species underlying the relevant industrial processes. In this thesis, the surface forces among bubbles, hydrophobic polymers, asphaltenes and bitumen in complex aqueous media have been directly quantified to reveal their interaction mechanisms.

Polystyrene (PS) of different molecular weights have been used as model hydrophobic polymers, and their interactions with air bubbles and oil droplets in aqueous solutions have been investigated using the bubble probe atomic force microscope (AFM) technique. The measured forces were analyzed by a theoretical model based on Reynolds lubrication theory and augmented Young−Laplace equation by including the influence of disjoining pressure. Despite the surfaces of PS of different molecular weights showing similar hydrophobicity (i.e., water contact angle in the air), differences were detected in the strength of their hydrophobic (HB) interactions with air bubbles and oil droplets. It is found that molecular chain mobility plays an important role in surface hydrophobic interactions and surface hydrophobicity. It is also found that the hydrophobic interactions between PS and air bubbles or oil drops can be significantly suppressed due to the presence of surface-active species such as surfactants in the aqueous solutions.

The surface forces of air bubbles, asphaltenes and asphaltenes-toluene droplets in various aqueous solutions have been quantified using an integrated thin film drainage apparatus and bubble probe AFM. The effects of asphaltenes concentration, pH, salinity, presence of Ca^{2+} and surfactants have been investigated. In solutions of high salinity (i.e., 100 mM NaCl), the HB interaction plays a critical role in the attachment of air bubbles and asphaltenes surfaces or oil droplets, by overcoming the repulsive van der Waals forces (VDW) and electrical double layer (EDL) interactions. Increasing the asphaltenes concentration in oil droplets enhances their HB attraction with bubbles due to strengthened asphaltenes adsorption and their aggregation at the interface of aqueous and oil media. Increasing aqueous solution pH weakens the HB interaction as the asphaltenes-toluene surfaces become more negatively charged and less hydrophobic under higher pH. Under low salinity conditions (i.e., 1 mM NaCl), the strong repulsive EDL and VDW interactions inhibit the bubble-oil droplet contact. Introducing Ca^{2+} ions and surfactants leads to strong steric repulsion, preventing the contact of bubbles and asphaltene-oil droplets.

The interaction forces between air bubbles and various bitumen surfaces in complex aqueous media have also been systematically measured. AFM imaging results show that the bitumen surfaces become rougher in aqueous solutions of high NaCl and $CaCl_2$ concentrations and a strongly alkaline environment. Surface force measurements demonstrate the impact of ionic strength, solution pH and presence of surfactants on the bubble–bitumen interaction and attachment. In solutions of low salinity, the EDL repulsion dominates the bubble-bitumen interaction and prevents the bubbles from attaching to the bitumen surfaces, and such effects are further enhanced with increasing

solution pH. Under high salinity conditions, the EDL interactions are significantly suppressed, and the HB interaction overcomes the VDW repulsion, leading to the bubble-bitumen attachment. Increasing the solution pH weakens the bubble-bitumen HB attraction interaction. It is also found that the apparent HB interaction can be strengthened with the addition of calcium ions, contributing to the bubble-bitumen attachment. Interestingly, the addition of a small amount of surfactants to the aqueous solutions suppresses the bubble-bitumen attachment, due to the weakened hydrophobic interaction and interfacial steric interaction, even under high salinity conditions.

This thesis work has advanced the fundamental understanding of surface interaction mechanisms among bubbles, hydrophobic polymers, asphaltenes, bitumen, and oil droplets in complex aqueous solutions at the nanoscale. The results offer useful insights on how to effectively modulate such interfacial interactions in oil production, water treatment and other interfacial processes.

Preface

This thesis is an original work conducted by Diling Yang, containing published content from peer-reviewed journals.

Part of Chapter 1 of this thesis has been published as: (1) Yang, D.; Peng, X.; Peng, Q.; Wang, T.; Qiao, C.; Zhao, Z.; Gong, L.; Liu, Y.; Zhang, H.; Zeng, H., Probing the interfacial forces and surface interaction mechanisms in petroleum production processes, *Engineering,* 2022. (2) Qiao, C.[#]; Yang, D.[#]; Mao, X.; Xie, L.; Gong, L.; Peng, X.; Peng, Q.; Wang, T.; Zhang, H.; Zeng, H., Recent advances in bubble-based technologies: Underlying interaction mechanisms and applications, *Applied Physics Reviews*, 2021, 8, 011315: 1-35. I was responsible for the manuscript composition.

Chapter 2 of this thesis has been published as Yang, D.; Xie, L.; Mao, X.; Gong, L.; Peng, X.; Peng, Q.; Wang, T.; Liu, Q.; Zeng, H.; Zhang, H.; Probing Hydrophobic Interactions between Polymer Surfaces and Air Bubbles or Oil Droplets: Effects of Molecular Weight and Surfactants, *Langmuir* 38.17 (2021): 5257-5268. I was responsible for materials synthesis, data collection and analysis, as well as the manuscript composition. Dr. Lei Xie and Dr. Xiao hui Mao assisted with the AFM force measurement and the material characterization. Dr. Lu Gong, Dr. Xuwen Peng, Dr. Qiongyao Peng, Tao Wang and Dr. Qi Liu contributed to the manuscript revision. Dr. Hao Zhang and Dr. Hongbo Zeng were the corresponding authors and were involved in the experimental design and manuscript composition.

Chapter 3 has been submitted as Yang, D.; Zhao, Z.; Gong, L.; Sun, Y.; Peng, X.; Peng, Q.; Wang, T.; Liu, Q.; Zhang, H.; Zeng, H.; Surface Interaction Mechanisms of Air

Bubbles, Asphaltenes and Oil Drops in Aqueous Solutions with Implications for Interfacial Engineering Processes, *Journal of Colloid and Interface Science*, 2023. I was responsible for material synthesis, experimental design, data collection and analysis, as well as manuscript composition. Dr. Ziqian Zhao helped with the ITFDA experiment. Dr. Lu Gong assisted with the AFM force measurement and data analysis. Dr. Yongxiang Sun assisted with the zeta potential experiment. Dr. Xuwen Peng, Dr. Qiongyao Peng, Tao Wang and Dr. Qi Liu contributed to the manuscript revision. Dr. Hao Zhang and Dr. Hongbo Zeng were the corresponding authors and were involved in the experimental design and manuscript composition.

Chapter 4 of this thesis has been submitted as Yang, D.; Qiao, C.; Mao, X.; Wang, J.; Xie, L.; Chen, J.; Peng, X.; Peng, Q.; Wang, T.; Liu, Q.; Zhang, H.; Zeng, H.; Probing the Surface Forces between Air Bubbles and Bitumen Surfaces: Effects of Solution Chemistry, *Separation and Purification Technology*, 2023. I was responsible for materials synthesis, data collection and analysis, as well as the manuscript composition. Dr. Xiao hui Mao and Dr. Lei Xie assisted with the AFM force measurement. Dr. Jingyi Wang assisted with the imaging experiment. Dr. Jingsi Chen helped to conduct the TGA experiment. Dr. Chenyu Qiao, Dr. Xuwen Peng, Dr. Qiongyao Peng, Tao Wang and Dr. Qi Liu contributed to the manuscript revision. Dr. Hao Zhang and Dr. Hongbo Zeng were the corresponding authors and were involved in the experimental design and manuscript composition.

Dedicate to

my family members

Acknowledgements

First and foremost, I would like to express my sincere gratitude to Dr. Hao Zhang for his great supervision, insightful guidance and all the support throughout my entire PhD study. I am also grateful to Dr. Hongbo Zeng and his whole research group for the training of various experimental techniques and assistance with all the experiment work. I appreciate their creative ideas and suggestions that provide me with a great learning experience during my research study, and especially their inspiring encouragement when I was confronted with research difficulties. The two professors' enthusiasm and dedication to scientific research always inspire me to fight for my career goal as a dedicated researcher.

I must express my gratitude to Dr. Lei Xie and Dr. Xiaohui Mao for their constructive guidance on my surface force experiments. Besides, I would like to thank all the group members in Dr. Zeng's lab and my co-authors, especially Dr. Lu Gong, Chenyu Qiao, Ziqian Zhao, Dr. Jingsi Chen, Dr. Jingyi Wang, Yongxiang Sun, Dr. Xuwen Peng, Dr. Qiongyao Peng, and Tao Wang for all their kind support on my research work.

Finally, I would like to thank my family members. Thanks to my parents for their love, caring, support and sacrifices in educating me and preparing me for my future.

The lab facilities used in this research and part of the research work have been supported by the Natural Sciences and Engineering Research Council of Canada (NSERC), Canada Foundation for Innovation (CFI), and the Department of Chemical and Materials Engineering at the University of Alberta. I am very grateful to all the above great support.

Table of Contents

List of Tables

List of Figures

List of Abbreviations

AFM	atomic force microscopy
PS	polystyrene
ITFDA	integrated thin film drainage apparatus
VDW	van der Waals
EDL	electrical double layer
Tg	glass transition temperature
SAGD	steam-assisted gravity drainage
BBTs	bubble-based technologies
p	pressure
R	radius
NBs	nanobubbles
SFG	sum-frequency generation
HB	hydrophobic
SFA	surface force apparatus
DLVO	Derjaguin-Landau-Verwey-Overbeek
RICM	reflection interference contrast microscopy
OT	optical tweezer

MBI	multiple beam interferometry
FECO	fringes of equal chromatic order
A_H	Hamaker constant
h	separation distance
κ	inverse Debye length
ε_0	the vacuum permittivity
ε	dielectric constant
φ	respective surface potentials
σ	respective surface charge density
C_0	constant relevant to the surface wettability
D_0	the decay length of hydrophobic (HB) interaction
SRYL	Stokes–Reynolds–Young–Laplace
γ	interfacial tension
PFO	perfluorooctane
CTAC	cetyltrimethylammonium chloride
SDS	sodium dodecyl sulfate
MW	molecular weights
OTS	octadecyltrichlorosilane

r	the radical coordinate
μ	the dynamic viscosity
Π	overall disjoining pressure
θ	the static water contact angle
rms	root-mean-square
NaOH	sodium hydroxide
NaCl	Sodium chloride
HCl	hydrogen chloride
$CaCl_2$	Calcium chloride
SiO_2	silicon dioxide
k_B	the Boltzmann constant
e	the fundamental charge of an electron
TGA	thermogravimetric analysis
CHNS	Elemental Analysis
FTIR	Fourier transformation infrared spectroscopy
SI	Supporting information
ΔG	Free energy

CHAPTER 1. Introduction

1.1 Background

The colloidal interactions among bubbles, oil droplets, polymers, asphaltenes and bitumen in aqueous media play important roles in many engineering processes such as mineral flotation, bitumen extraction, oil/water separation, and wastewater treatment. Over the past few decades, much effort has been devoted to investigating the physicochemical characteristics and interaction behaviors of bubbles, oil droplets, polymers, asphaltenes and bitumen, which advanced the knowledge to improve the controllability and performance of relevant engineering processes. Nevertheless, there are still some challenging problems that remain to be solved.

Despite the petroleum industry's significant technological developments for more than a century, oil production processes still present challenging issues. For example, bitumen is liberated and extracted from oil sands by 1) using warm water and then, through flotation and froth treatment processes, achieving oil/water/solid separation in surface mining operation; or 2) using high-temperature steam via in situ extraction (e.g., steam-assisted gravity drainage (SAGD) recovery).[1-3] During these extraction processes, one of the most common issues is the fouling of organic and inorganic species on pipelines and other equipment. Such fouling issues can reduce the efficiency of the production process and increase maintenance costs. Additionally, the formation of stable oil-water emulsions causes problems during oil production, transportation, and processing. Stable oil-water emulsions pose significant challenges in various stages of oil production, including oil/water separation, process water cleaning, and tailings water treatment. The presence of saline water in crude oil generally leads to corrosion, fouling, and other operational issues in refining and processing equipment. Stable water-in-oil emulsions also

impact the quality of the final oil product. Inefficient separation of oil and water can lead to environmental contamination and health hazards.

These challenging interfacial phenomena are mainly driven and influenced by the molecular/surface forces of the various objects (e.g., different molecules, emulsion drops, and mineral particles) interacting at the oil/water/solid/gas interfaces in the relevant petroleum operations (Figure 1.1). Thus, characterizing and quantifying the intermolecular and surface forces involved are critical for a complete understanding of these challenging interfacial issues and of the underlying interfacial interaction mechanisms, which can facilitate the development of new materials, effective chemicals, and improved technologies to solve these challenges in relevant engineering processes.

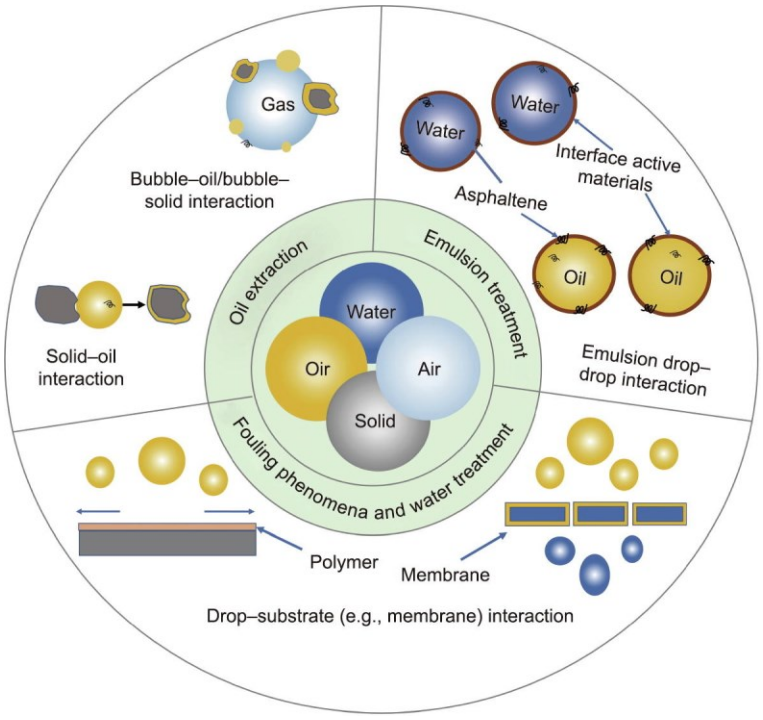

Figure 1.1. Schematic illustration of different interactions among various components (e.g., emulsion drops, mineral solids, gas bubbles, and chemical additives) at the water/oil/solid/gas

interfaces in selected petroleum operations (e.g., oil extraction, emulsion treatment, fouling and antifouling phenomena, and water treatment).

1.1.1 Air bubble

Gas bubbles widely exist in nature and numerous industrial processes. The physicochemical characteristics of bubbles such as large specific surface area, low density, and hydrophobicity make them an ideal platform for developing colloidal and interfacial technologies. Over the past century, much effort has been devoted to investigating the physical and chemical characteristics of bubbles and the intermolecular and surface interactions involved in bubble-containing systems. Many practical bubble-based technologies (BBTs) such as air flotation have been developed and applied in engineering, biomedical, and material fields. The physical characteristics and behaviors of bubbles play a key role in various BBTs. Firstly, the bubble size could impact the characteristics, interaction behaviors, and lifetime of bubbles. Different sizes and the related lifetime of the bubbles in liquid phase are summarized in Figure 1.2a. The macro bubble rise rapidly toward the liquid surface and burst to be the short lifetime due to the buoyancy force and relatively low gas dissolution rate. With the features of rapidly floating speed and not bring other impurities, the macro bubbles are commonly used in fermenters, gas-liquid reactors, and ore-flotation equipment.[4] The pressure difference Δp between gas phase of a bubble and bulk liquid phase is inversely related to the bubble size, as given by the Young-Laplace equation.[5]

$$\Delta p = p_g - p_l = \frac{2\gamma}{R} \tag{1.1}$$

where p_g and p_l are the pressures of interior and exterior parts of the bubble, respectively, γ is surface tension of the liquid phase (usually water), and R is the radius of bubble.

For the micro bubbles and nanobubbles (NBs), the effect of buoyancy force is not very significant, so their velocity in bulk liquid phase is generally slow. However, the high interior pressure of these small bubbles contributes to a fast gas dissolution rate, which can cause them to shrink and collapse in the bulk liquid phase.[6-8] But some studies showed the nanobubbles could exhibit ultra-long lifetime that could be up to one month in certain cases on the solid surface and in bulk aqueous media.[7, 9] There are some hypotheses proposed to explain the reasons, the most accepted opinion is that the adsorbed contaminants or surface-active species lower the Laplace pressure and stable the bubbles.[7, 10-11]

The surface properties of bubbles dominate their behaviors in fluid media and play a key role in practical applications. One of the most important properties of bubbles is surface hydrophobicity. That is because the gas phase in bubbles is incapable of forming hydrogen bonds with water molecules at the surface, and the water molecules near the bubble surface are prone to reorientate and reconstruct an ordered structure with many dangling hydroxyl groups (–OH) pointing at the bubble surface, as illustrated in Figure 1.2(b). Recently, nonlinear optical technologies such as sum-frequency generation (SFG) spectroscopy have demonstrated the existence of dangling –OH groups and ordered hydrogen bond networks near air bubble surfaces. This provides direct experimental evidence to support theoretical studies and has improved our understanding of the origin of bubble hydrophobicity.[10-12] The hydrophobicity allows bubbles to interact with other objects through hydrophobic (HB) interaction and perform specific tasks in various engineering applications.[12]

Another important property of the air bubbles is their surface charge, as shown in Figure 1.2(c), As mentioned above, the ordered water layers near bubble surfaces have many dangling – OH groups, of which the charges pointing toward bubble surfaces are more likely negative, therefore, the dipole moments of water molecules in the vicinity of bubbles could contribute to their surface charges. Many previous studies proposed that the surface charges of bubbles might arise from adsorption of OH^- ions.[13] The OH- ions arising from dissociation of water molecules prefer to adsorb on bubble surfaces due to their small radius and high polarity. The charge property of bubble is usually characterized by zeta potential, which is defined as the electrical potential at slipping plane in the electric double layer (EDL) structure.[14] According to the classical Derjaguin-Landau-Verwey-Overbeek (DLVO) theory, the zeta potential of bubble has important influences on the bubble stability and interactions between bubbles and other objects, playing a key role in many industrial processes, including flotation, bitumen extraction, and wastewater treatment.[15-16]

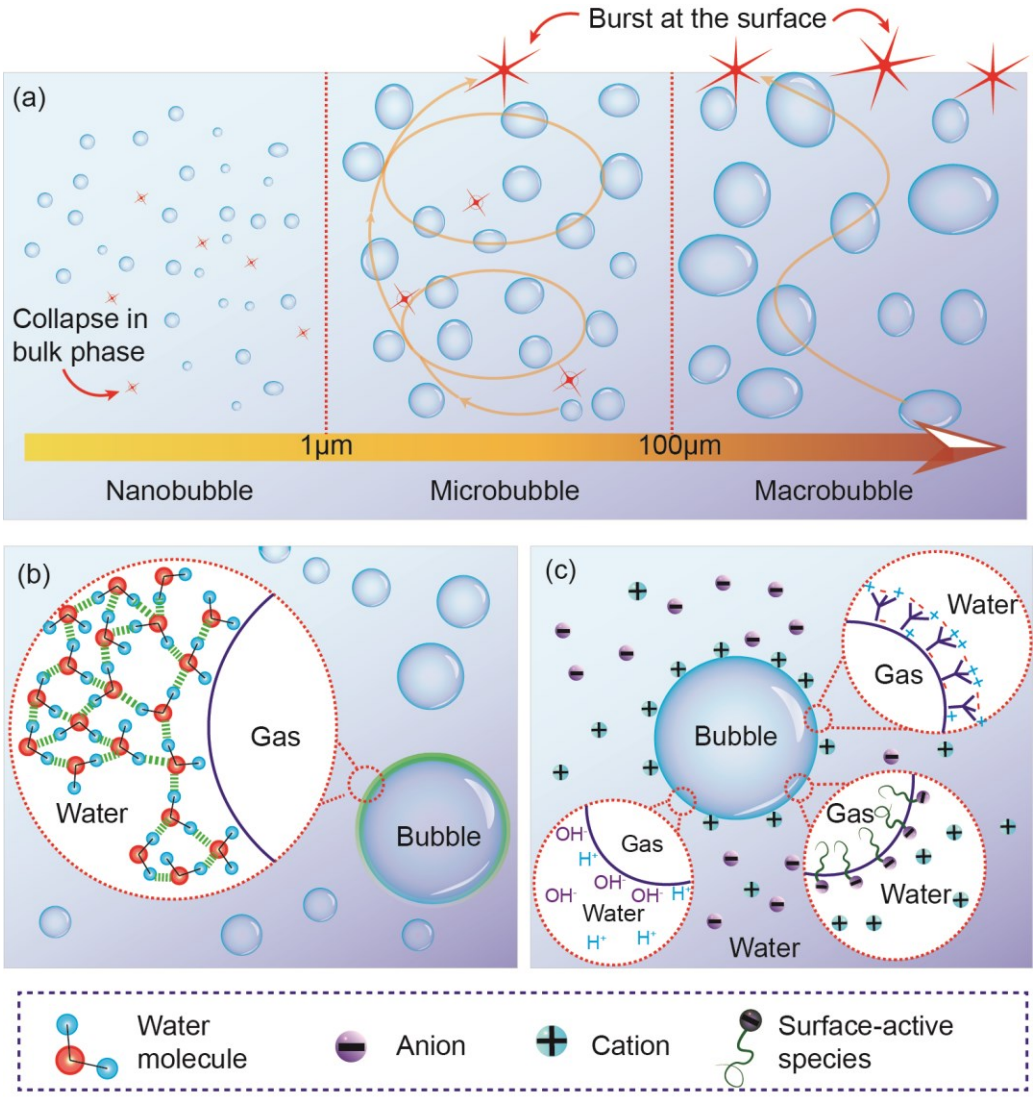

Figure 1.2. Schematics of (a) the relationship between size and lifetime of bubbles [Reproduced and adapted with permission from T. Temesgen et al., Adv. Colloid Interface Sci. 246, 40–51 (2017).5 Copyright 2017 Elsevier], (b) the possible origin of hydrophobicity of bubble surface, and (c) possible origins of surface charges of bubbles in water.

1.1.2 Hydrophobic Interactions

As motioned above, the hydrophobic nature of air bubbles allows them to attach to other hydrophobic species in various engineering applications. Hydrophobic interaction plays an

important role in many industrial processes, biological and technological systems. Understanding the fundamental hydrophobic interaction mechanisms provides potential approaches for modulating relevant interfacial interactions in a variety of engineering applications.[17-19] Much effort has been devoted to investigating the surface forces between bubbles and other objects (e.g., another bubble, oil droplet, particle, or flat surface). With the invention of atomic force microscope (AFM) in 1986, different AFM techniques such as the colloidal probe AFM and bubble probe AFM have been developed for quantifying colloidal forces.[20] Due to the hydrophobic nature of bubbles, bubble probe AFM is a powerful and ideal technique for investigating the fundamental hydrophobic interaction mechanism. By measuring the forces between bubbles and chemical-modified surfaces (e.g., mica, silica, and gold substrate), the effects of solution salinity, surface micro-/nano-structure, and molecular-level heterogeneity of surface hydrophobicity on the hydrophobic interaction have been investigated. By using this technique, previous studies have systematically investigated the effects of surface-active impurities,[21] electrolytes,[22] pH,[23] and hydrodynamic conditions[24] on the interaction behaviors of bubbles (e.g., deformation, coalescence) in complex aqueous environment. These studies showed that varying the solution conditions could generally change the surface mobility of bubbles and consequently affect their stability and the related hydrophobic interaction.

Surface functionalization has been widely applied to modify the surface properties of different materials in many engineering applications, thus the hydrophobic interaction between bubbles and these functionalized surfaces could be modulated. For example, chemical reagents such as activators, collectors, and depressants have been widely used by the mining industry to modify the surface hydrophobicity of selected mineral surfaces. It is noted that previous studies have showed that the strength of HB interaction between air bubbles and hydrophobic surfaces

does not always follow a monotonic correlation with the surface hydrophobicity (i.e., water contact angle), and tuning the surface nanoscale structures (e.g., surface chemistry, heterogeneity, molecular mobility) provides a facile approach to modulate the HB interactions.

Polymers, especially hydrophobic polymer, are widely applied in various engineering and bioengineering applications. However, the quantitative characterizations of the interactions between air bubbles or oil droplets and hydrophobic polymers remain limited. Understanding the interactions between hydrophobic polymers and deformable objects (e.g., gas bubbles, oil droplets) and characterizing the effects of water chemistry, molecular weight of hydrophobic polymers, and the presence of surfactant additives, is of both fundamental and practical importance.

1.1.3 Emulsion treatment

Water-in-oil, oil-in-water, and even more complex (e.g., water-in-oil-in-water, oil-in-water-in-oil) emulsions commonly exist in various petroleum production processes. Stable emulsions are generally undesired in the petroleum industry, as they can cause technical challenges such as difficulty separating oil and water, fouling, and corrosion issues (due to the presence of ions such as Cl^-). Understanding the interaction mechanisms of the emulsions in petroleum production is of great importance for developing effective approaches for demulsification and enhancing oil/water separation. Direct quantification of the molecular/surface forces of the different objects involved in the emulsion interactions in petroleum engineering has long been experimentally difficult, particularly at the molecular or nanoscopic scale, and could not be achieved until advances were made in nanomechanical

technologies such as the surface forces apparatus (SFA) and AFM. The experimental difficulties were mainly due to the complex chemical composition of crude oil, as well as the highly deformable oil/water interfaces of the emulsions; it was very challenging to experimentally correlate the forces, deformation of surfaces, and separation distance during emulsion interactions. The development of the bubble/drop probe AFM technique and its coupling with reflection interference contrast microscopy (RICM) have made it experimentally feasible to simultaneously probe surface forces with better than nanonewton-scale resolution and measure the spatiotemporal evolution (i.e., drainage dynamics) of confined thin liquid films down to nanometer-scale thickness for the interactions of highly deformable emulsion drops and bubbles. In this section, we provide some examples from our previous studies to show how the forces involved in emulsion interactions can be quantified using the relevant nanomechanical technologies.

1.1.4 Surface-active species

The stabilization and destabilization of emulsions in petroleum production are highly relevant to the adsorption of interface-active species (e.g., natural surfactants, asphaltenes, and fine solids) to oil/water interfaces resulted in a rigid interfacial film, which can significantly change the interfacial properties (e.g., interfacial tension and interfacial rheology) and influence the surface interactions of emulsion droplets. Which can cause many challenging issues such as fouling phenomena and environmental concerns. Thus, characterizing the interaction forces involved in the phenomena relevant to fouling/antifouling issues and water treatment is of great significance.

The presence of surface-active species has great influence on the zeta potential of droplets. Surface-active species prefer to adsorb on droplets surfaces, while their charged head groups usually stay in aqueous phase and thus change the zeta potential of droplets.[25] The adsorption of negatively charged surface-active species generally makes the zeta optional of droplets more negative; while the adsorption of positively charged surface-active species would cause an opposite influence. Surface-active species can also modify the surface properties of other objects. For example, polymer adsorption on mineral surfaces has been found to significantly affect bubble-mineral interaction and attachment, which may suppress the gas flotation of mineral particles adsorbed with hydrophilic polymers.

Asphaltenes are commonly accepted as a typical interface-active species that contributes to the stabilization of emulsions in petroleum production. The drop probe AFM technique was used to determine the interaction forces between two oil droplets and between two water-in-oil droplets with and without asphaltenes in different aqueous solutions. The strong steric repulsive force arising from the asphaltene films adsorbed at the oil/water interface could efficiently suppress the coalescence behavior. To better understand the emulsion interactions, the intermolecular interactions among the interface-active species (i.e., asphaltenes) at the oil/water interfaces were also directly quantified using an SFA, and it found that the asphaltene molecules/nanoaggregates had a stronger tendency to be in a swelling conformation in a relatively good solvent (i.e., heptol with higher toluene fractions), which led to increased steric repulsion between the opposing swelling asphaltene surfaces.[26] In order to gain a comprehensive understanding of emulsion interactions in petroleum production processes, it is crucial to characterize the effects of various factors such as solution salinity, pH, type of ions, as well as asphaltenes concentration and other interface-active compounds on these surface interactions.

1.1.5 Bitumen extraction

Depending on the geological conditions of the oil reservoirs and oil properties (e.g., light, medium, or heavy oil), oil is extracted or recovered by the petroleum industry using various methods. The oil sands industry has been extracting and producing bitumen by either using open-pit mining technology for reserves up to 75 m deep—which consists of large-scale excavation, crushing, mixing with warm water, hydro transport (liberation), flotation, and froth treatment processes—or using in situ extraction methods such as the SAGD recovery method by injecting high-temperature steam into oil sands deposits (mostly more than 200 m deep). As the warm-water-based open-pit mining method results in challenging tailings water issues, the oil industry has also explored the feasibility of other extraction technologies, such as non-aqueous extraction methods involving organic solvents. In the water-based bitumen extraction processes, the interactions among bitumen, mineral solids, air bubbles, and the surrounding fluid media (i.e., water and organic solvents) significantly determine the efficiency of the abovementioned large-scale industrial interfacial processes. Thus, quantifying these interaction forces and understanding the underlying interfacial interaction mechanisms are of both fundamental and practical importance in developing more efficient and controllable oil-extraction processes and technologies.

During bitumen aeration, or the so-called bitumen flotation process, liberated bitumen is aerated to float to the upper region of the fluid, which is a very important step for collecting the bitumen product and determining the bitumen recovery and product quality.[2] Hence, it is very important to determine the interaction mechanisms among the air bubbles and bitumen under various solution conditions and investigate the effects of environmental conditions. Over the past

few years, several studies have characterized the interaction forces involving bitumen, asphaltenes, solid surfaces, and gas bubbles using SFA and AFM techniques.[27-28] These quantitative measurements found that the interaction forces are strongly dependent on the solution conditions (e.g., pH, salt type, and salinity in aqueous media) and organic solvent.[29-32]

1.2 Surface force measurements

Several nanomechanical tools have been developed for measuring intermolecular and surface forces, such as the surface forces apparatus (SFA),[33-37] [4–8], the atomic force microscope (AFM),[37] optical tweezer (OT),[38-39] the osmotic stress device,[40] and the force balance.[41] Among these techniques, the SFA and AFM have been widely applied to measure the interaction forces of various molecules, particles, emulsion drops, gas bubbles, and substrates in complex fluids from the molecular level to the nano- and micro-scales.[26, 29, 42-48] Many studies have contributed to the quantification of interaction forces among different species in crude oil, such as asphaltenes, mineral particles, bitumen, air bubbles, and chemical additives (e.g., flocculants and antifoulants).[29, 31, 49-54] In this chapter, we briefly review the basics of the typical interaction forces affecting different objects during oil production processes, the working principles of two commonly used nanomechanical tools (i.e., SFA and AFM), and how we can apply these nanomechanical tools to directly probe the interfacial forces in selected petroleum production processes.

1.2.1. Surface forces apparatus (SFA)

Since the classical Derjaguin–Landau–Verwey–Overbeek (DLVO) theory was reported in the 1940s for describing the stability of colloids, many nanomechanical techniques have been developed and widely applied to measure the molecular and surface forces of different components, such as the SFA, AFM, and OT.[42, 55-57] The SFA technique was pioneered by Tabor, Winterton, and Israelachvili in the late 1960s to early 1970s and was then modified and significantly advanced by Israelachvili. Since the 1970s, Israelachvili and coworkers have applied the SFA technique to quantify the physical forces (both normal and lateral forces) of a wide range of materials and biological systems in vapors and complex fluid media.[35-36, 42, 58] Many non-covalent interactions (e.g., van der Waals (VDW), electrical double layer (EDL), hydration, hydrophobic, cation-π, and anion-π interactions) were first experimentally quantified by using the SFA technique. [32-33, 39,32, 53, 58-61] Figure 1.3 provides an illustration of the setup for surface force measurements between two curved surfaces using the SFA, which are mounted in a crossed-cylinder configuration.[62] A picture of an SFA2000 chamber is shown in Figure 1.3(a). The SFA can be used to directly quantify the forces of two interacting surfaces in vapors, organic media, or aqueous solution media that are correlated to the absolute separation distance.[63] This tool is particularly important for measuring the interaction forces of soft materials such as biopolymers, polymers, surfactants, and petroleum materials (e.g., asphaltenes and bitumen). In SFA measurements, the absolute separation distance and the surface deformation are determined through an optical technique called multiple beam interferometry (MBI) by monitoring the wavelength shifts of the fringes of equal chromatic order (FECO), as shown in Figures 1.3(b) and (c), which is generally difficult to achieve using other force measurement techniques.[64] The normal forces are determined using Hooke's law by monitoring the spring deflection based on

the difference between the driven distance and the actual surface-surface separation change, as monitored using the FECO patterns. Taking asphaltenes as an example, the SFA can be used to measure the interactions between two asphaltene layers; between an asphaltene layer and a solid substrate surface or different coatings; or the interaction force changes between two substrate surfaces associated with the dynamic adsorption of asphaltenes from a solution medium, as illustrated in Figure 1.3(d). Such experimental configurations can be directly adopted to measure the forces of other substances (e.g., surfactants, polymers, bitumen, and nanoparticles).

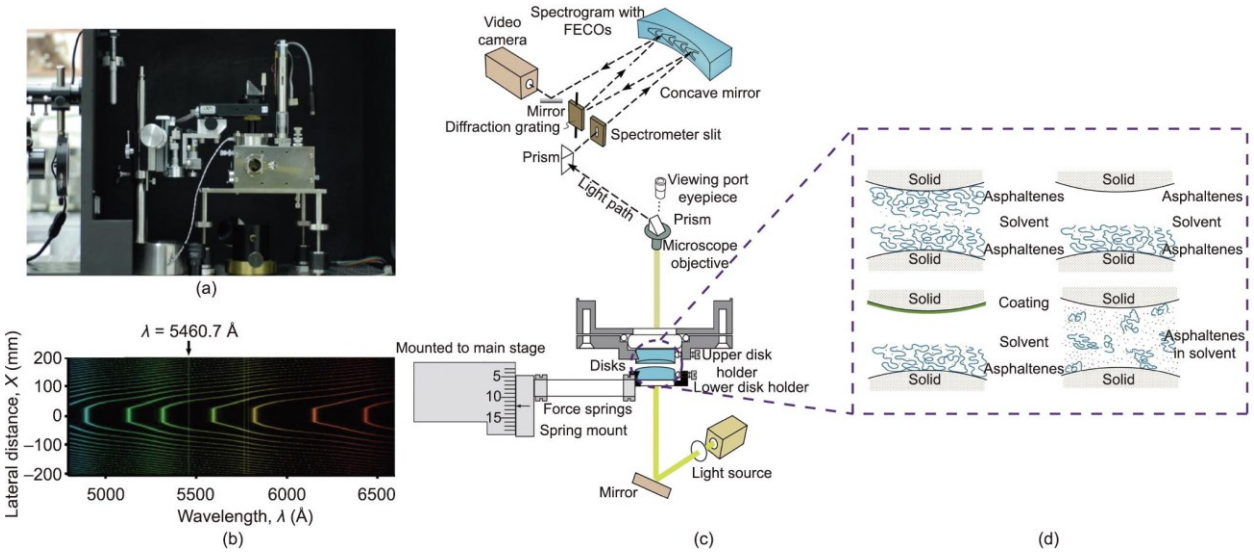

Figure 1.3. Illustration of the setup for surface force measurements between two curved surfaces using the SFA. (a) Picture of a SFA2000 chamber. (b) Typical picture of the FECO fringes obtained using MBI, corresponding to the interaction position when two curved surfaces are in contact. (c) Schematic of the sample alignment and light path in a typical SFA measurement. (d) Four commonly used experimental configurations for quantifying the forces of: asphaltenes versus asphaltenes (asphaltenes are used as a model material for illustration); asphaltenes versus a solid substrate; asphaltenes versus a coating; and two solid surfaces associated with the dynamic adsorption of asphaltenes. Reproduced from Ref. [62], with permission.

1.2.2. Atomic force microscope (AFM)

AFM is another powerful nanomechanical tool that has been widely used for characterizing the nanoscopic surface topographic features of various materials and for measuring the molecular and surface forces in vapors or complex fluid media.[57, 65] Figure 1.4 provides an illustration of the working principles of the AFM. Various AFM probes have been used for imaging and force measurements, including: a sharp tip, a colloid probe made by gluing a colloidal particle to a tipless cantilever, and bubble and drop probes made by attaching a gas bubble or liquid droplet to a tipless cantilever, as shown in Figure 1.4.[44-46, 66-75] The colloid probe enables the surface force measurements of various particle materials (e.g., minerals, polymers, and cells). Furthermore, the more recently developed bubble/drop probe techniques allow researchers to directly quantify the interaction forces of highly deformable objects such as water-in-oil or oil-in-water emulsions and the gas bubbles commonly present in petroleum production and other engineering processes. Recently, Zeng and coworkers coupled the colloid/drop/bubble probe AFM technique with reflective interferometry, achieving simultaneous measurements of surface forces and monitoring of the nanoscopic spatiotemporal evolution of the confined thin liquid film of bubbles, drops, colloids, and substrates.[20, 76] When measuring the forces using an AFM, a sharp AFM tip or a colloid/bubble/drop probe is placed on top of the desired sample and is then driven to approach the sample until the cantilever reaches a desired deflection with a selected contact time. The cantilever is then driven to move away from the sample to finish the approaching-separation force measurement cycle.[77-78] The interaction forces are determined based on Hooke's law by monitoring the deformation of the AFM cantilever (acting as a force spring), using a quartered photodiode to detect the laser reflection from the back side of the cantilever (Figure 1.4).[79]

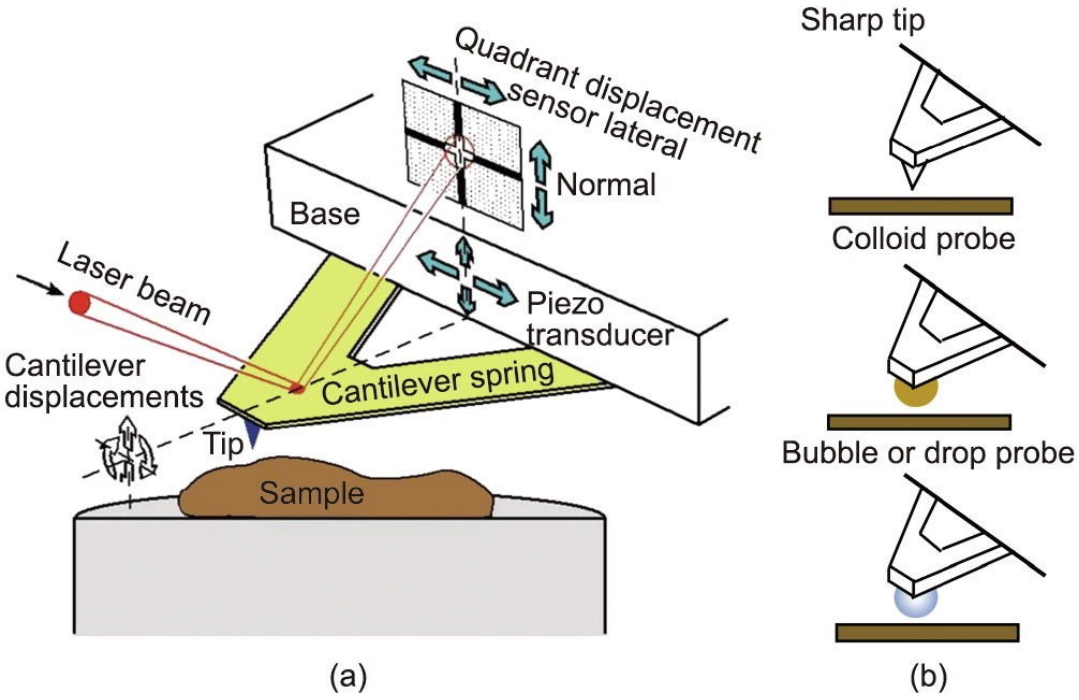

Figure 1.4. (a) Schematic of a typical experiment setup for imaging surface topography at the nanoscale or for force measurements using a sharp nano tip with an AFM. (b) Three commonly used AFM probes. Reproduced from Ref. 79 with permission.

1.3 Theoretical model

Force-distance profiles obtained from experimental measurements using nanomechanical tools generally need to be theoretically analyzed through colloidal interaction models, which provide useful information on the properties of the interacting materials and their interaction mechanisms. In a typical petroleum production process, many interaction forces—such as the VDW, EDL, and hydrophobic interactions—can influence the interaction behaviors of the different components involved.[80] VDW and EDL interactions are generally depicted by the classical Derjaguin–Landau–Verwey–Overbeek (DLVO) theory,[81] which has been widely

applied to analyze many colloidal and interfacial phenomena such as stability of colloidal suspensions. VDW forces are widely present in various materials and engineering systems, and the VDW forces of macroscopic objects of different geometries can be derived using the Hamaker approach or, more rigorously, using the Lifshitz theory.[20, 81] For the VDW interactions of two planar surfaces, the VDW force per unit area (also known as the VDW disjoining pressure) is given by Eq. (1.2), where A_H is the so-called Hamaker constant for two objects in a surrounding medium (e.g., an aqueous solution) and h is their separation distance.

$$\prod_{vdw} = -\frac{A_H}{6\pi h^3(r,t)} \tag{1.2}$$

Another important interaction is the EDL force, which is strongly dependent on the salinity, pH, ion type, pH of the aqueous media, and surface charge properties of the interacting objects. For material systems of different geometries, the equations for the EDL interactions are in different mathematical forms.[65, 81] The EDL forces of two parallel flat surfaces per unit area are given by Eq. (1.3) and (1.4) for the constant potential and constant charge cases, respectively,[57, 81] where κ is the inverse Debye length, ε_0 is the vacuum permittivity, ε is the dielectric constant of the aqueous solution, φ_1 and φ_2 are the respective surface potentials of materials 1 and 2, and σ_1 and σ_2 are the respective surface charge densities of materials 1 and 2.[81] For the interactions of two curved surfaces, the VDW and EDL interactions are related to the interaction energy of two parallel planar surfaces through the Derjaguin approximation.[57, 81]

$$\prod_{EDL} = \frac{2\varepsilon_0\varepsilon\kappa^2\left[\left(e^{+\kappa h}+e^{-\kappa h}\right)\varphi_1\varphi_2-\left(\varphi_1^2+\varphi_2^2\right)\right]}{\left(e^{+\kappa h}-e^{-\kappa h}\right)^2} \text{ (constant potential case)} \tag{1.3}$$

$$\prod_{EDL} = \frac{2}{\varepsilon_0\varepsilon}[\sigma_1\sigma_2 e^{-\kappa h}+(\sigma_1^2+\sigma_2^2)e^{-2\kappa h}] \text{ (constant charge case)} \tag{1.4}$$

For a symmetric configuration, the two surfaces are of the same material, and the above two equations can be simplified to Eq. (1.5) and (1.6), respectively.

$$\prod_{EDL} = \frac{2\varepsilon_0 \varepsilon \kappa^2 \varphi^2 \left[\left(e^{+\kappa h} + e^{-\kappa h} \right) - 2 \right]}{\left(e^{+\kappa h} - e^{-\kappa h} \right)^2} \text{ (constant potential case)} \tag{1.5}$$

$$\prod_{EDL} = \frac{2\sigma^2 e^{-\kappa h}}{\varepsilon_0 \varepsilon} \left[1 + 2e^{-\kappa h} \right] \text{ (constant charge case)} \tag{1.6}$$

In the early 1980s, Israelachvili and Pashley experimentally quantified the hydrophobic interactions of two hydrophobic surfaces in aqueous media via the self-assembly of two surfactant monolayers using an SFA.[59] In this work, the correlation between the hydrophobic interaction force per unit surface area and the separation distance was proposed to be exponential, given by Eq. (1.7) for two parallel planes, where C_0 is a constant (unit: $N \cdot m^{-1}$) relevant to the surface wettability of the objects, and D_0 is the decay length of hydrophobic (HB) interaction.

$$\prod_{HB} = -\frac{C_0}{2\pi D_0} \exp\left(-\frac{h(r,t)}{D_0} \right) \tag{1.7}$$

For interactions involving highly deformable liquid droplets and gas bubbles, under the influence of the interaction forces, the surfaces of droplets or bubbles readily deform while the confined liquid film drains off between the objects. The Stokes–Reynolds–Young–Laplace (SRYL) model, which couples the Stokes–Reynolds lubrication equation and the augmented Young–Laplace equation, has been commonly used to analyze the interaction process and the force results obtained.[82-83] The Stokes–Reynolds lubrication equation, given by Eq. (1.8),[84-87] describes the thin liquid film drainage between two interacting surfaces, where h(r,t) is the confined liquid film thickness, r is the distance between a selected position and the bubble

central axis, t is time, μ is the dynamic viscosity of the surrounding liquid, and p(r,t) is the excessive hydrodynamic pressure in the confined liquid film (as compared with the bulk liquid).

$$\frac{\partial h(r,t)}{\partial t} = \frac{1}{12\mu r}\frac{\partial}{\partial r}\left(rh^3 \frac{\partial p(r,t)}{\partial r} \right) \tag{1.8}$$

The augmented Young–Laplace equation describes the surface deformation of bubbles or drops by including the effects of disjoining pressure. Eqs. (1.9–1.11) show the augmented Young–Laplace equation for the interactions of gas bubbles or liquid droplets in different configurations, where R_b is the bubble/drop radius, R_p is the particle radius, $R_{bb} = 2(1/R_{b1}+1/R_{b2})^{-1}$ is the equivalent radius for bubble/drop 1 interacting with bubble/drop 2 with radii R_{b1} and R_{b2} respectively, $\gamma_{bb} = 2(1/\gamma_{b1}+1/\gamma_{b2})^{-1}$ is the equivalent interfacial tension for bubble/drop 1 interacting with bubble/drop 2 with interfacial tension γ_{b1} and γ_{b2} respectively, $R_{bp} = (1/R_b+1/R_p)^{-1}$, γ is the interfacial tension, and Π[h(r,t)] is the total disjoining pressure.[65, 81, 87-88]

$$\frac{\gamma_{bb}}{2r}\frac{\partial}{\partial r}\left(r\frac{\partial h(r,t)}{\partial r} \right) = \frac{2\gamma_{bb}}{R_{bb}} - p(r,t) - \Pi\left[h(r,t) \right] \text{(bubble/drop-bubble/drop)} \tag{1.9}$$

$$\frac{\gamma}{r}\frac{\partial}{\partial r}\left(r\frac{\partial h(r,t)}{\partial r} \right) = \frac{2\gamma}{R_b} - p(r,t) - \Pi\left[h(r,t) \right] \text{ (drop/bubble-plane)} \tag{1.10}$$

$$\frac{\gamma}{r}\frac{\partial}{\partial r}\left(r\frac{\partial h(r,t)}{\partial r} \right) = \frac{2\gamma}{R_{bp}} - p(r,t) - \Pi\left[h(r,t) \right] \text{(drop/bubble-spherical particle)} \tag{1.11}$$

The total disjoining pressure usually arises from different interactions such as the VDW, EDL, HB, and steric interactions involved in the interacting systems, as shown in Eq. (12):

$$\Pi\left[h(r,t) \right] = \Pi_{VDW} + \Pi_{EDL} + \Pi_{HB} + \Pi_{Steric} + ... \tag{1.12}$$

The overall interaction forces can be described by Eq. (13)[89] [65]:

$$F(t) = 2\pi \int_0^{\infty} \left[p\left(h(r,t)\right) + \prod\left(h(r,t)\right) \right] \cdot r dr \tag{1.13}$$

1.4 Objectives

Air bubbles, hydrophobic polymers, asphaltenes, bitumen, and oil droplets are commonly involved in various industrial processes, such as oil production and transportation, oil/water separation, bitumen extraction, bitumen flotation, and wastewater treatment. The colloidal interactions among these species drive the relevant interfacial phenomena in these industrial operations. Quantitative characterization of the surface interactions will not only improve the fundamental understanding of these interfacial phenomena, but also provide potential methods to modulate the relevant colloidal interactions in these industrial processes. However, despite the significant progress achieved over the past few decades, the quantification of the surface forces among air bubbles, hydrophobic polymers, asphaltenes, bitumen, and oil droplets still remains very limited.

The main objective of this proposed research is to reveal the fundamental interaction mechanisms among bubbles, droplets, bitumen, asphaltenes, and hydrophobic polymers in complex aqueous media. The effects of aqueous chemistry (e.g., pH, salinity, type of salts, and presence of surfactants) on their surface interactions are systematically investigated. More specifically, this thesis work has focused on the following three areas.

(1) Probing the interaction forces and characterizing the surface interaction mechanisms, particularly hydrophobic interaction, between deformable air bubbles/oil drops and hydrophobic

polymers in aqueous solutions of varying water chemistry. Polystyrene of different molecular weights are used as model hydrophobic polymers.

(2) Quantifying the surface forces and interaction mechanisms of air bubbles, asphaltenes and asphaltenes-toluene droplets in aqueous solutions. The effects of asphaltenes concentration, pH, salinity, type of ions (e.g., Ca^{2+} ions) and presence of surfactants on these surface interactions will be systematically examined.

(3) Characterizing the surface interaction mechanisms between air bubbles and bitumen surfaces in complex aqueous media. The influence of solution salinity, pH, addition of divalent salts and surfactants on bubble-bitumen interactions will be systematically investigated.

CHAPTER 2. Probing Hydrophobic Interactions between Polymer Surfaces and Air Bubbles or Oil Droplets: Effects of Molecular Weight and Surfactants

2.1 Introduction

Hydrophobic interaction, also known as hydrophobic effect, generally describes the strong attraction between hydrophobic moieties in aqueous media, which is not included in the classical Derjaguin−Landau−Verwey−Overbeek (DLVO) theory.[19, 79, 90-92] Hydrophobic interaction is one of the most important physical interactions in many water-based biological and technological systems, and it plays a critical role in numerous interfacial phenomena in engineering applications,[93-95] such as self-assembly of surfactants and amphiphilic polymers,[96-97] cell manipulation,[98] protein purification,[99] drug and gene delivery,[100] froth flotation,[101] and oil/water separation.[102-105] Polymers, deformable bubbles, and liquid droplets are commonly involved in these engineering processes. Thus, it is of both fundamental and practical importance to unravel the basic physical law underlying the hydrophobic interactions of polymers, gas bubbles, and liquid droplets.

It is generally accepted that the hydrophobic moieties (or surfaces) are incapable of forming hydrogen bonds with the adjacent water molecules, which results in relatively ordered orientation of the water molecules near the hydrophobic moieties (or surfaces) and the decrease in the overall entropy of the system.[17-19] Consequently, the significant loss in entropy, which is unfavorable from the thermodynamic consideration, pulls the hydrophobic moieties or surfaces to cluster together and minimizes their surface area exposed to water, which is manifested as a strong attraction.[90, 106-107] From this perspective, it has been increasingly acknowledged that the hydrophobic interaction is an entropy-driven process closely related to the water structure effect

(e.g., orientation, hydrogen bonding network) surrounding the hydrophobic substances, even though the origin and nature of hydrophobic effects are still incompletely understood.[108] From this point of view, the hydrophobic interaction could be potentially modulated by altering a series of factors such as water chemistry and surface properties of hydrophobic materials.

Significant progress has been achieved on improving the fundamental understanding of hydrophobic interaction over the last few decades. Much effort has been devoted to quantifying the hydrophobic interactions between two hydrophobic surfaces in aqueous media, mainly using nano-mechanical tools such as surface forces apparatus (SFA) and atomic force microscopy (AFM).[90, 107] The development of the bubble/drop probe AFM technique, coupled with theoretical computation, has enabled the quantification of hydrophobic interaction involving highly deformable objects including gas bubbles and oil droplets.[72, 74, 109] Nevertheless, the range and magnitude of the hydrophobic force differ a great deal in the experimental results obtained from different material systems.[19] Previous studies also showed that surface hydrophobicity, which is commonly characterized by a water contact angle, may not be the only dominant parameter determining hydrophobic interaction and that hydrophobic materials with unique specificity in surface nanoscale structure and surface chemistry may exhibit different ranges of hydrophobic interaction, leading to different degrees of a water structuring effect at the interface.[106] Among the hydrophobic materials or surfaces investigated previously such as monolayers of small surfactant-like molecules through physical self-assembly or chemical grafting, hydrophobic polymers have received relatively much less attention for their hydrophobic interaction, which, however, are widely used in diverse engineering applications. It still remains unclear how the factors, such as water chemistry, molecular weight of polymers,

and the presence of surfactant additives, affect the interactions between hydrophobic polymers and deformable objects (e.g., gas bubbles, oil droplets), which is the main focus of this work.

In this work, polystyrene (PS) of different molecular weights was chosen as the model hydrophobic polymer. The interaction forces of smooth PS surfaces and air bubbles and oil droplets (perfluorooctane (PFO) as a model oil) have been measured in aqueous solutions using the bubble/drop probe AFM technique. A theoretical model based on the Reynolds lubrication theory and augmented Young−Laplace equation was used to analyze the measured forces and the contributions of various surface forces (e.g., van der Waals, electrical double layer, and hydrophobic interactions) to the overall disjoining pressure. Three surface-active species including cetyltrimethylammonium chloride (CTAC), Pluronic F-127, and sodium dodecyl sulfate (SDS) were chosen as model surfactants. The effects of the presence of these surfactants and ethanol to the aqueous solutions on the surface forces between PS and air bubbles or oil droplets were also investigated. The results in this work have improved the fundamental understanding of the hydrophobic interaction mechanism between hydrophobic polymers and deformable air bubbles and oil droplets, with useful implications for modulating the interactions of polymers, gas bubbles, and oil droplets and related interfacial phenomena in a wide range of engineering processes.

2.2 Materials and Methods

2.2.1 Materials

Styrene ($\geqslant$ 99%) was purchased from Sigma-Aldrich, Canada. Polystyrene (PS) with different molecular weights (MW 590, 810, 1110, 2330, 46300, 1000000, denoted as PS590, PS810, PS1110, PS2330, PS46300, and PS1M, respectively) was purchased from Polymer

Source Inc., Canada. Perfluorooctane (PFO) was purchased from Sigma-Aldrich, Canada. NaCl was provided by Fisher Scientific, Canada. Silicon wafers with silicon dioxide layers (SiO2/Si wafers, SiO2 layer thickness ~ 500 nm) were obtained from Nano FAB, University of Alberta, Canada. The PS solutions (0.5 wt %) were prepared by dissolving the corresponding polymers in toluene (Fisher Scientific, 99.9%). The NaCl aqueous solutions were prepared by dissolving a suitable amount of highest-purity anhydrous NaCl (Sigma-Aldrich, 99.999+%) in Milli-Q water with a resistance of ⩾18.2 MΩ cm. Cetyltrimethylammonium chloride (CTAC) 25 wt % aqueous solution was purchased from Sigma-Aldrich, Canada. Pluronic F-127 and sodium dodecyl sulfate (SDS) powder were obtained from Sigma-Aldrich, Canada.

2.2.2 Preparation and Characterization of PS Surfaces.

In this work, PS solution was prepared by dissolving a desired PS sample in a good organic solvent (i.e., toluene) (Fisher Scientific, 99.9%) at a concentration of 0.5 wt %. The PS surfaces were prepared by spin-coating 2−3 drops of the PS solution on a silica substrate (1 × 1cm2) at ~2000 rpm. The prepared PS surfaces were stored under vacuum overnight to remove the solvent prior to the characterizations. The fabricated PS surfaces were charactered by AFM imaging using a Dimension Icon AFM with a silicon AFM tip (silicon nitride, nominal resonant frequency ~ 150 kHz, nominal spring constant ~ 0.7 N/m) via the tapping mode. The surface hydrophobicity was determined by measuring the static water contact angle using a sessile drop method via a contact angle goniometer (ramé-hart instrument, Succasunna, NJ). For each PS sample, six measurements were conducted on three independently prepared polymer surfaces to ensure the data repeatability.

2.2.3 Surface Force Measurements using the Bubble/Drop Probe Atomic Force Microscope (AFM).

The bubble/drop probe AFM technique was applied to measure the interaction forces between PS surfaces and air bubbles (Figure 2.1A) in aqueous solutions. The detailed experimental setup for the bubble/drop probe AFM technique has been reported previously.[74, 76, 91] Briefly, in a typical force measurement using the bubble/droplet probe AFM, the bottom glass slide of a fluid cell was treated to be partially hydrophobic (with a static water contact angle around 50°) by immersing in 10 mM octadecyltrichlorosilane (OTS) in toluene for ~10 s for anchoring air bubbles or oil droplets. A customized tipless rectangular silicon AFM cantilever (400 × 70 × 2 μm) with a circular patch of gold (radius of 32.5 μm) was hydrophobized by immersing in 10 mM dodecanethiol in ethanol overnight for easily picking up air bubbles or oil droplets from the glass surface.[110] The spring constant of the cantilever was determined to be a typical value of 0.3−0.4 N/m using the Hutter and Bechhoefer method.[111] The gas bubbles were generated by carefully pumping a small amount of air through a custom-made ultrasharp glass pipet into the aqueous solution. Oil droplets were generated on the glass slide using a similar method. The bubble or drop probe was prepared by carefully lowering the hydrophobized AFM cantilever to contact the bubble or oil droplet of suitable size and then elevating the bubble or oil droplet from the glass surface. The interaction forces between the PS surfaces and bubbles or oil droplets were measured by driving the air bubbles or oil droplets toward and away from the PS surfaces by a piezo-actuator under a range of velocities from 1 to 30 μm/s. During a force measurement, time variation of the cantilever deflection was recorded, which could be further converted to forces using the spring constant based on Hooke's law. The actual variation of the cantilever-substrate separation with time was also recorded by the AFM software.

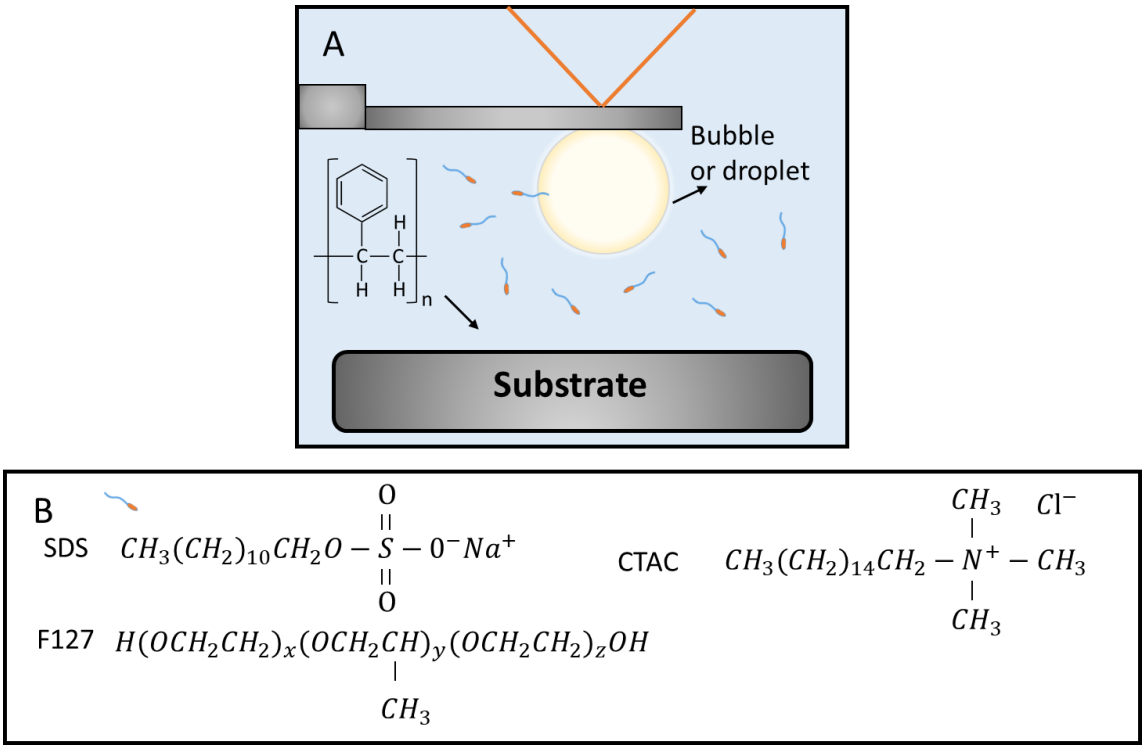

Figure 2.1. (A) Experimental setup for measuring the interaction forces between bubble/droplet and PS fabricated surface. (B) The molecular formula of three types of surface-active species.

A theoretical model based on the Reynolds lubrication theory and augmented Young−Laplace equation (SRYL) was applied to analyze the measured force data and determine the separation distance between deformable droplets or bubbles and the polymer surfaces during force measurements in the schematic shown in Figure 2.1.[112-116] Assuming tangentially immobile hydrodynamic boundary conditions at the oil/water, air/water, and solid/water interfaces,[76, 86, 117] the thickness of the water film confined between the drop or bubble and the substrate surface can be expressed by the Reynolds lubrication theory as shown in eq 2.1.

$$\frac{\partial h(r,t)}{\partial t} = \frac{1}{12\mu r}\frac{\partial}{\partial r}\left(rh^3 \frac{\partial p(r,t)}{\partial r} \right) \tag{2.1}$$

where *h(r,t)* is the film thickness, r is the radical coordinate, μ is the dynamic viscosity of water and *p(r,t)* is the excessive hydrodynamic pressure relative to the bulk solution.

The droplet/bubble deformation during the surface interactions is correlated to the hydrodynamic pressure, disjoining pressure, and Laplace pressure, as described by the augmented Young−Laplace equation by including the effects of disjoining pressure.[117-118]

$$\frac{\gamma}{r}\frac{\partial}{\partial r}\left(r\frac{\partial h(r,t)}{\partial r}\right)=\frac{2\gamma}{R_0}-p(r,t)-\Pi\left[h(r,t)\right] \tag{2.2}$$

Here, γ is the interfacial tension, R_0 is the radius of the droplet/bubble and Π is the overall disjoining pressure due to surface forces.[47, 106, 119-122]

The overall disjoining pressure is contributed by various surface interactions such as the van der Waals (vdW) interaction(Π_{VDW}), electrical double layer interaction (EDL), and hydrophobic (HB) interaction, which are given by eqs 2.3, 2.4, and 2.5, respectively,[74, 79] where A_H is the Hamaker constant for air bubbles (or liquid droplets) interacting with polymer surfaces in a liquid medium, κ^{-1} is the Debye length, φ_1 and φ_2 are the surface potentials of air bubbles (or liquid droplets) and polymer surfaces, respectively, D_0 is the decay length of the hydrophobic interaction, and C is a constant (N/m) related to the static water contact angle θ on the substrate and interfacial tension shown in eq 2.6. [33, 123]

$$\prod_{vdw}=-\frac{A_H}{6\pi h^3(r,t)} \tag{2.3}$$

$$\prod_{EDL}=\frac{2\varepsilon_0\varepsilon\kappa^2\left[\left(e^{+\kappa h}+e^{-\kappa h}\right)\varphi_1\varphi_2-\left(\varphi_1^2+\varphi_2^2\right)\right]}{\left(e^{+\kappa h}-e^{-\kappa h}\right)^2} \tag{2.4}$$

$$\Pi_{HB} = -\frac{C_0}{2\pi D_0}\exp\left(-\frac{h(r,t)}{D_0}\right) \tag{2.5}$$

$$C = 2\pi\gamma\left(1-\cos\theta\right) \tag{2.6}$$

The overall interaction force between an air bubble and a solid surface F(t) was calculated by integrating the hydrodynamic pressure p and the disjoining pressure Π as follows.[83, 113, 124]

$$F(t) = 2\pi\int_0^\infty \left[p\left(h(r,t)\right)+\Pi\left(h(r,t)\right)\right]\cdot r dr \tag{2.7}$$

2.3 Results and Discussion

2.3.1 Characterization of PS Surfaces.

The PS surfaces were characterized by AFM imaging, and the topographic AFM images of PS of different molecular weights (PS590, PS810, PS1110, PS2330, PS46300, and PS1M) are shown in Figure 2.2A−F, respectively. The AFM images in air indicate that the fabricated PS surfaces were very smooth, and the root-mean- square (rms) roughness ranges from about 0.15 nm−0.26 nm. Thus, the influence of surface roughness on the surface force measurements could be neglected in this work.

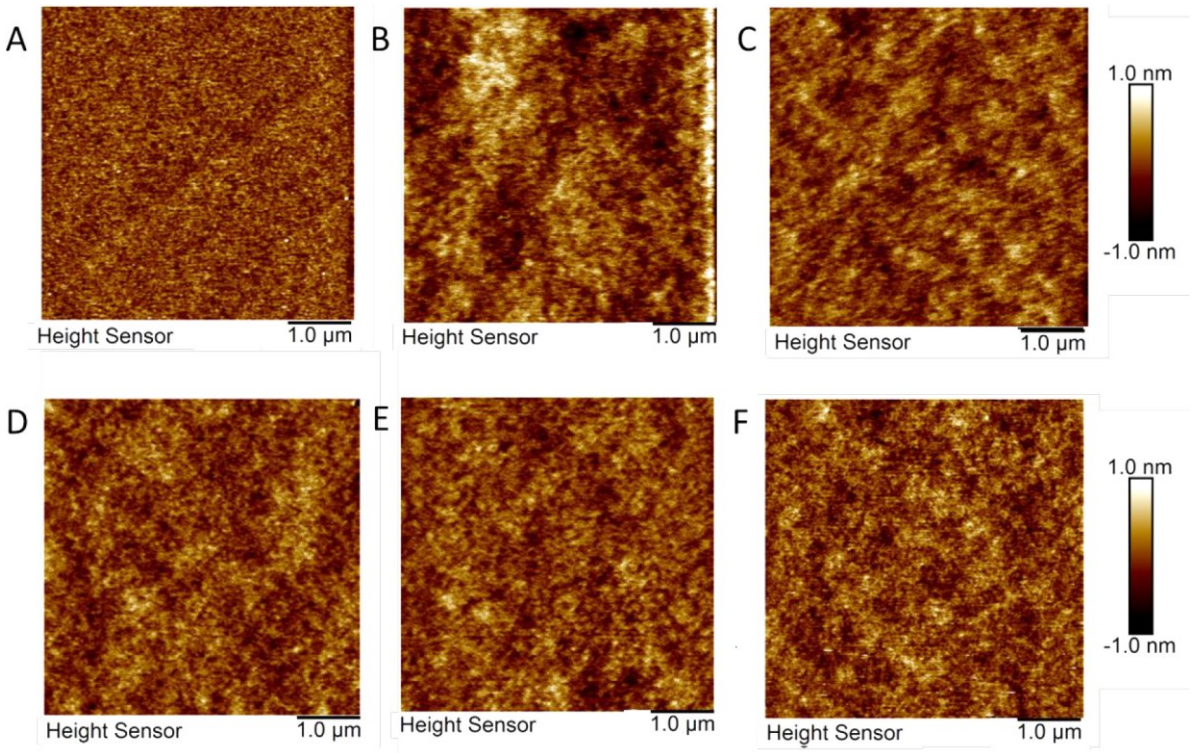

Figure 2.2. Topographic AFM images of PS surfaces of different molecular weights in air: (A) PS590, (B) PS810, (C) PS1110, (D) PS2330, (E) PS46300, and (F) PS1M, which show the root-mean-square (rms) roughness of 0.17, 0.26, 0.20, 0.20, 0.20, and 0.22 nm, respectively. The scan size of the images was 5 µm × 5 µm.

The surface morphologies of the PS surfaces were also imaged in a 1 M NaCl aqueous solution (the same solution conditions used in surface force measurements) in the tapping mode using the PeakForce QNM technique of the Bruker ICON AFM. The topographic AFM images of PS of different molecular weights (PS590, PS810, PS1110, PS2330, PS46300, and PS1M) are shown in Figure 2.3A−F, respectively. The rms roughness of the PS590 and PS810 surfaces is 0.47 and 0.53 nm, respectively, and the rms roughness of the PS1110, PS2330, PS46300, and PS1M surfaces is 0.27, 0.28, 0.24, and 0.29 nm, respectively. The AFM imaging results in aqueous solutions show that the surface roughness of two PS surfaces of relatively lower MW

(PS590 and PS810, with Tg lower than the room temperature 23 °C) slightly increased, while the surface roughness of glassy polymers (PS1110, PS2330, PS46300, and PS1M) did not obviously change, suggesting that the polymer surfaces were stable in the 1 M NaCl solutions. It is also noted that the PeakForce QNM AFM imaging results in Figure 2.3 show that there were no nanoscopic gas bubbles on all the PS surfaces, agreeing with our previous results that nanobubbles would be present on PS surfaces in aqueous solutions of low salinity but would not be noticeable on PS surfaces in aqueous solutions of high salinity.[61, 120, 125] The AFM imaging results further indicate that the possible substrate-supported nanobubbles on the surface force measurements between PS surfaces and air bubbles or oil droplets in NaCl solutions of high salinity (i.e., 1 M) can be neglected in this work.

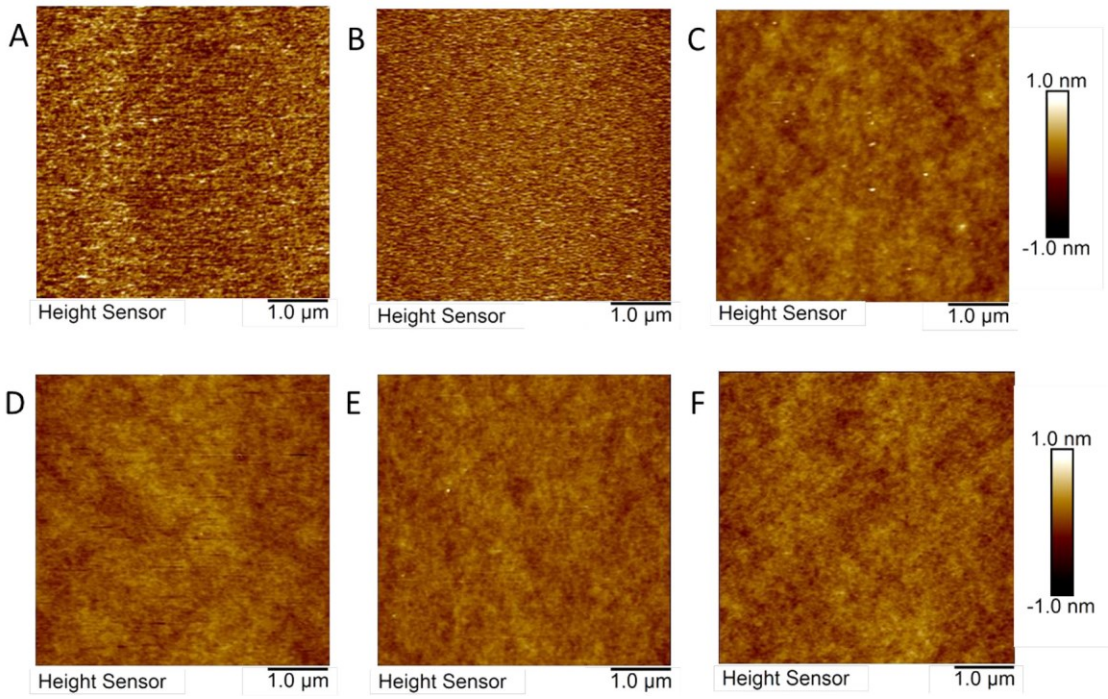

Figure 2.3. Topographic AFM images of PS surfaces of six different molecular weights in a 1 M NaCl solution. (A) PS590, (B) PS810, (C) PS1110, (D) PS2330, (E) PS46300, and (F) PS1M,

which show the rms roughness of 0.47, 0.53, 0.27, 0.28, 0.24, and 0.29 nm, respectively. The scan size of the images was 5 μm × 5 μm.

The optical images of water contact angles on PS590, PS810, PS1110, PS2330, PS46300, and PS1M surfaces in air are shown in Figure 2.4A−F, respectively. All the fabricated PS surfaces show a static water contact angle of ~90°, indicating that these PS surfaces of different molecular weights show similar surface wettability.

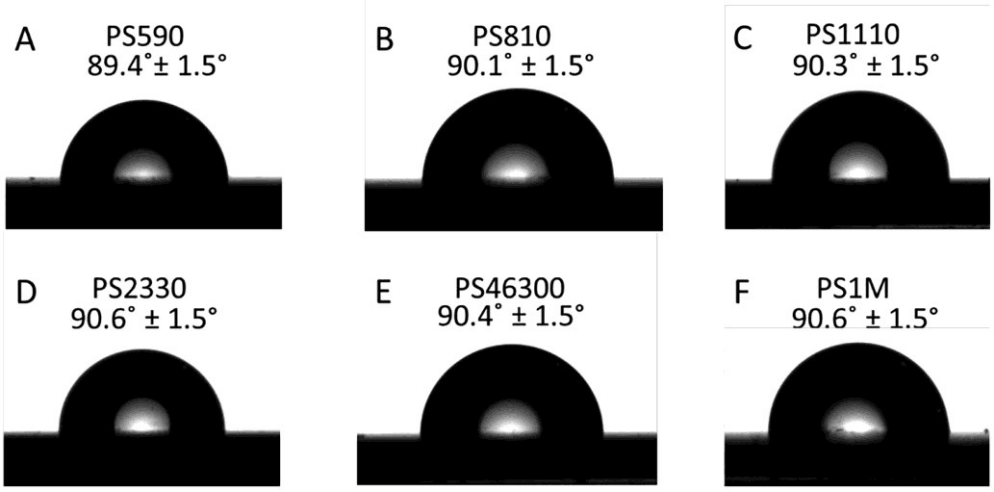

Figure 2.4. Optical images of static water contact angles on PS surfaces of different molecular weights (PS590, PS810, PS1110, PS2330, PS46300, and PS1M) in air.

2.3.2 Surface Forces between PS and Air Bubbles or PFO Droplets.

2.3.2.1 The Effect of Polymer Molecular Weight.

The interaction forces between PS surfaces of different molecular weights and air bubbles or droplets of a model oil PFO have been measured using the bubble/drop probe AFM technique, and the influence of the addition of surfactants and ethanol (miscible with water but with lower molecular polarity) to the aqueous solution on the surface forces has also been investigated. In

this work, the salinity conditions of all the aqueous solutions were fixed at 1 M NaCl, which was mainly based on the following considerations. (1) The Debye length for the electrical double layer (EDL) interaction in 1 M NaCl is less than 1 nm, and the EDL would be significantly suppressed so the role of hydrophobic interaction in the overall surface forces could be clearly highlighted. (2) Both our previous studies and the AFM imaging results in this work show that no nanobubbles could be noticed on the PS surfaces in 1 M NaCl, which eliminate the influence of surface nanobubbles on the intrinsic hydrophobic interaction between PS and air bubbles or oil droplets.[61, 120, 125] Thus, the measured surface forces arise from the intrinsic interactions between PS surfaces and air bubbles or oil droplets.

Figure 2.5A−C shows the representative force profiles between air bubbles and low molecular weight PS surfaces (i.e., PS810, PS2330) and a high molecular weight PS surface (i.e., PS46300) in a 1 M NaCl solution, respectively. The interaction force profiles for the PS590, PS1110, and PS1M cases are shown in Figure S2.1A−C, respectively. During these force measurements, the EDL interaction was significantly suppressed by the high salinity aqueous solution conditions, and thus only the VDW interaction and other possible non-DLVO forces contribute to their interactions. It is noted that the VDW interaction between air bubbles and PS surfaces in aqueous solutions is repulsive. When the air bubble was driven close to the fabricated PS substrate, the repulsive forces were first measured as shown in all the force profiles in Figure 2.5 and Figure S2.1, which were mainly due to the repulsive VDW interaction and possible hydrodynamic interaction. After a certain critical repulsion was reached, the air bubbles jumped into contact with the PS surfaces (so-called jump-in behaviors) in the force measurements for all the PS surfaces. Since the VDW forces and possible hydrodynamic interaction were repulsive when the bubbles approached the PS surfaces, such jump-in behaviors were believed to arise

from the attractive hydrophobic interaction between the air bubbles and PS surfaces. It is noted that the driving velocity of the bubble probe during force measurements was fixed at 1 μm/s, so the hydrodynamic interactions could be neglected, as compared to other surface interactions involved.[76, 91] According to eq 2.3 for the VDW interactions, all the cases of PS surfaces with different molecular weights would experience the same repulsive VDW forces with air bubbles in aqueous solutions. The force profiles in Figure 2.5 were analyzed using the SRYL model, and the decay length of the hydrophobic interaction D_0 was fitted to be about 0.67, 0.73, and 0.73 nm for PS810, PS2330, and PS46300, respectively. Similar analysis was applied to the force profiles in Figure S2.1, which gave the fitted decay length of the hydrophobic interaction D0 ~ 0.67, 0.73, and 0.75 nm for PS590, PS1110, and PS1M, respectively. Interestingly, the above results indicate that PS590 and PS810 show similar strength of the hydrophobic interaction with air bubbles, while they show a slightly weaker hydrophobic interaction than that of PS1110, PS2330, PS46300, and PS1M. The PS1110, PS2330, PS46300, and PS1M surfaces possess a similar hydrophobic interaction with air bubbles. The evolution of the bubble profiles during the approaching process in the PS-bubble force measurements for the PS810, PS2330, and PS46300 cases was also shown in Figure 2.5D−F, respectively. Right before the "jump-in" behaviors, the minimal separation distance of the confined thin water film of the three cases was determined to be 6.3, 7.4, and 7.4 nm, respectively. For the PS2330 and PS46300 cases, a pimple shape was observed in the center region of the bubbles right before jumping into contact with the PS surfaces, and similar drop profiles were also observed for the PS1110 and PS1M cases.

The disjoining pressure profiles due to the various surface forces (e.g., VDW, hydrophobic interactions (HB)) for the PS810, PS2330, and PS46300 cases are also shown in Figure 2.5G−I, respectively. The results indicate that the disjoining pressure due to the hydrophobic attraction

Π_{HB} overcomes the repulsive VDW interaction (Π_{VDW}), which is the driving interaction for the bubble attachment to hydrophobic polystyrene. At a certain critical separation (h_{min}), the attractive overall disjoining pressure just exceeded the Laplace pressure inside the air bubble, and the bubble would jump into contact with the PS surface.

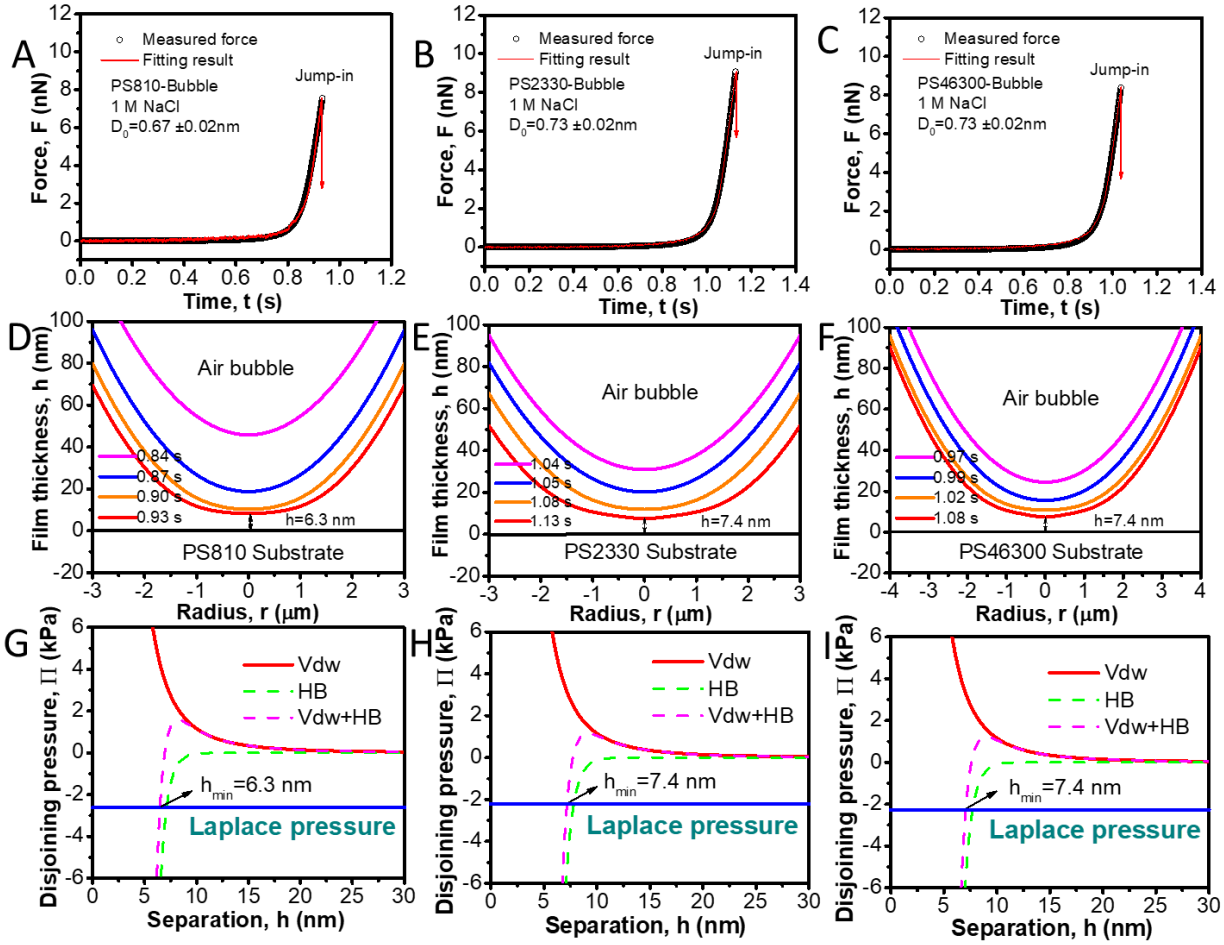

Figure 2.5. (A–C) Interaction force curves measured between air bubbles and PS surfaces of different molecular weights: (A) PS810 (bubble radius R0 = 59 μm), (B) PS2330 (R0 = 69 μm), and (C) PS46300 (R0 = 69 μm). Open symbols are the experimentally measured data, and the red curves are the theoretical fitting results based on the SRYL model. (D–F) Evolution of the bubble profiles during the bubble-PS approaching process where the red curve denotes the

bubble profiles at the minimal separation before the "jump-in" behavior. (G–I) Disjoining pressure profiles due to different surface interactions (i.e., VDW and HB) for the (G) PS810, (H) PS2330, and (I) PS46300 cases, respectively.

When a PFO oil droplet approaches hydrophobic PS surfaces in aqueous solutions of high salinity, their interaction behaviors are very similar to those between an air bubble and PS surfaces. The interaction force profiles between PFO droplets and PS810 and PS2330 in a 1 M NaCl solution are shown in Figure 2.6A, B, respectively. The jump-in behavior was also observed during the approaching process of the two cases, which was mainly driven by the attractive hydrophobic interaction, by overcoming the repulsive VDW interaction. The decay length of hydrophobic interaction was determined to be $D_0 \sim 0.62$ nm during the PFO-PS810 interaction, which is slightly smaller than that of the PFO-PS2330 case with $D_0 \sim 0.69$ nm. Figure 2.6C, D shows the evolution of the PFO droplet profiles during the approaching process for the PS810 and PS2330 cases, respectively, which shows that the minimal separation before the jump-in behavior for the two cases was 5.7 and 6.5 nm, respectively. At such critical separation distances, the pimple shape in the center region of the bubble could develop, induced by the attractive hydrophobic interaction between the oil drop and the hydrophobic polymer surfaces. Figure 2.6E, F shows the disjoining pressure profiles due to the VDW and hydrophobic interactions between PFO droplets and PS810 and PS2330 surfaces, respectively, during their approaching process. At the critical separation (h_{min}), the overall attractive disjoining pressure exceeded the Laplace pressure inside the PFO droplet, leading to the attachment of the oil droplet and PS surface. The force profiles and evolution of the oil drop profiles during the interactions between PFO droplets and PS surfaces of other molecular weights (PS590, PS1110, PS46300, and PS1M) are shown in Figure S2.2. PS590 showed similar interaction behavior as PS810,

while PS1110, PS46300, and PS1M showed similar interaction behaviors as PS2330. Overall, PS590 and PS810 showed slightly weaker hydrophobic interaction with PFO droplets, as compared to PS1110, PS2330, PS46300, and PS1M.

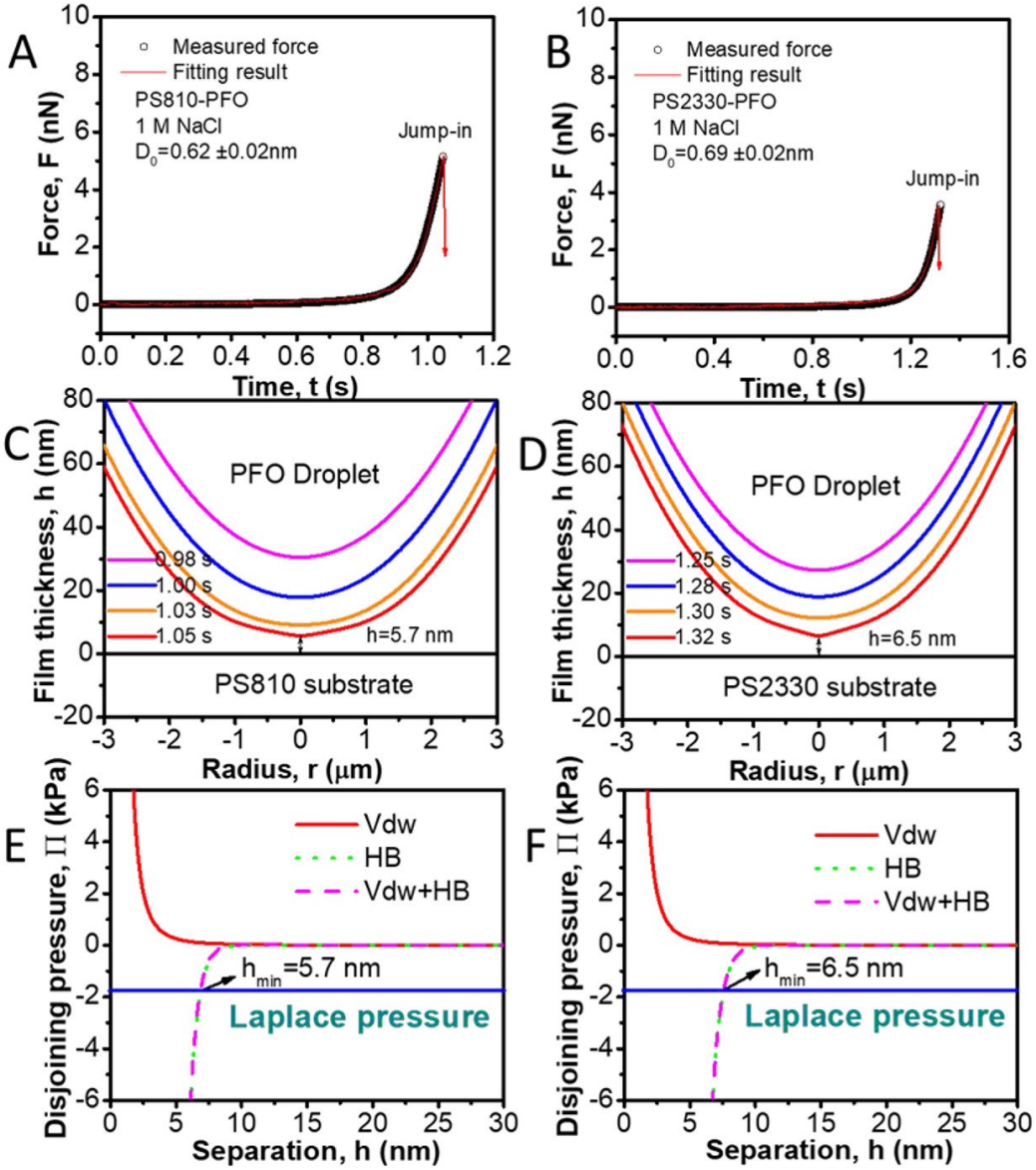

Figure 2.6. (A,B) Interaction force curves measured between model oil droplet (PFO droplet) and PS surfaces of different molecular weights: (A) PS810 (droplet radius R0 = 65 μm) and (B) PS2330 (R0 = 59 μm). Open symbols are the experimentally measured force data, and the red

curves are the theoretical computation results based on the SRYL model. (C,D) Evolution of the oil droplet profiles during the PS-drop approaching process for (C) PS810 and (D) PS2330, and the red curve denotes the bubble profile at the minimal separation right before "jump in" phenomena. (E,F) Disjoining pressure profiles arisen due to the different surface forces (i.e., VDW and HB) involved in the interactions of PFO droplets with (E) PS810 and (F) PS2330.

As shown in Table S2.1, the glass transition temperature Tg of PS590 and PS810 is −45 °C and −2 °C, respectively. At room temperature (23 °C), PS590 and PS810 are viscous liquids. The Tg of PS1110, PS2330, PS46300, and PS1M is higher than the room temperature, and they are in the glassy solid state at room temperature.[126-128] The measured water contact angles of the PS surfaces are almost the same, showing the same surface wettability. Interestingly, in aqueous solutions of high salinity, the direct surface force measurements in this work demonstrate that PS590 and PS810 show slightly weaker hydrophobic interactions with air bubbles and PFO droplets as compared to the glassy PS1110, PS2330, PS46300, and PS1M. Such slightly weaker hydrophobic interactions of viscous PS of low molecular weights could be likely contributed by the following factors. (1) The viscous PS of low molecular weight displays more flexible chain mobility than that of glassy PS with high molecular weight. (2) The PS590 and PS810 surfaces show the increased rms roughness in 1 M NaCl as compared to that in air which might be due to the cation-π interaction between relatively flexible PS590 and PS810 chains at the polymer/water interface and the Na+ ions in the aqueous solution, while the surface roughness of the glassy PS surface does not obviously change. These two factors could potentially cause a weakened water structuring/ordering effect of the water molecules close to viscous PS surfaces of low molecular weights, thus leading to the slightly weaker hydrophobic interactions with air bubbles and oil droplets compared to the glassy PS of high molecular weights.

2.3.2.2 The Effect of Solvent.

In many practical applications, water is mixed with another solvent of lower polarity such as ethanol as the fluid media for the relevant industrial processes. Thus, it is of both fundamental and practical importance to understand how the presence of another miscible solvent (with water) influences the interactions between deformable objects such as air bubbles and hydrophobic polymers. In this work, ethanol was chosen as a model solvent and mixed with water. It is noted that the solubility of salt in a water−ethanol mixture decreases with increasing ethanol content. The solubility of NaCl in pure ethanol and pure water is 0.65 g/L (~11 mM) and 360 g/L (~6.15 M), respectively, at room temperature.[129] In this work, the surface forces between the air bubble and PS1M were measured in water and a water−ethanol mixture (with 10 vol % ethanol), with the NaCl concentration fixed at 1 M, and the force profiles are shown in Figure 2.7A,B, respectively. During the force measurement, jump-in behavior was observed, mainly driven by the attractive hydrophobic interaction by overcoming the repulsive VDW force. The decay length of the hydrophobic interaction was found to be $D_0 \sim 0.68$ nm for the PFO-PS1M case in 1 M NaCl with 10% ethanol, which was smaller than that for the bubble-PS1M case in a 1 M NaCl solution without ethanol ($D_0 \sim 0.75$ nm). This result indicates that the hydrophobic interaction between the air bubble and PS1M in the pure 1 M NaCl aqueous solution is stronger than that in the 1 M NaCl aqueous solution with 10 vol % ethanol. The evolution of the bubble profiles during the approaching process for the case without ethanol and the case with 10 vol % ethanol is shown in Figure 2.8C, D, respectively. The minimal separation before the jump-in behavior for the two cases was 7.4 and 6.3 nm, respectively. The profiles of the disjoining pressure arisen from the different surface forces involved (i.e., VDW, HB) for the two cases are shown in Figure 2.8E, F, respectively. These results indicate that when the overall attractive disjoining pressure

exceeds the Laplace pressure inside the bubble, the bubble would jump into contact with the PS surfaces in both cases, and the HB disjoining pressure for the pure 1 M NaCl case is stronger than that for the case with the addition of 10 vol % ethanol. The presence of 10 vol % ethanol in the aqueous solution could possibly weaken the hydrogen bonding network and structuring/ordering of the water molecules close to the PS surface, thus weakening the hydrophobic interaction with the air bubbles.

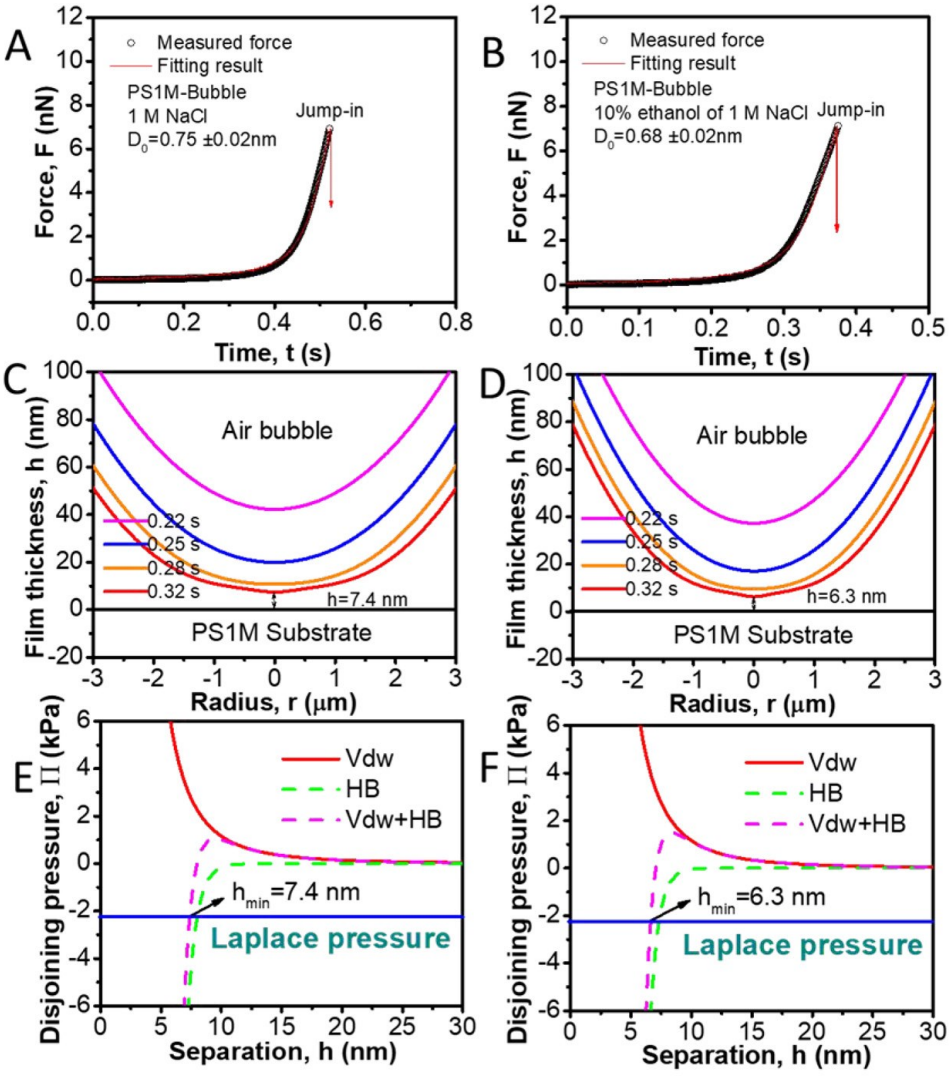

Figure 2.7. (A) Interaction force curves measured between an air bubble (bubble radius R0 = 69 μm) and the PS1M surface in a 1 M NaCl solution. (B) Interaction force curves measured

between an air bubble (R0 = 63 μm) and the PS1M surface in a 1 M NaCl solution with 10 vol % ethanol. Open symbols stand for the experimentally measured force data, and the red curves are the theoretical calculation results based on the SRYL model. (C,D) Evolution of the bubble profiles during the PS-bubble approaching process for the two cases, and the red curve denotes the bubble profile at the minimal separation right before the "jump in" phenomena. (E,F) Disjoining pressure profiles arisen due to the different surface forces (i.e., VDW and HB) involved in the interactions between PS1M surfaces and air bubbles in (E) a 1 M NaCl aqueous solution and (F) a 1 M NaCl aqueous solution with 10 vol % ethanol.

2.3.2.3 The Effect of Surfactants.

Surface-active species widely exist in aqueous media in engineering processes, which can significantly influence the surface properties (e.g., hydrophobicity, surface charges) of gas bubbles and liquid droplets, thus influencing the interaction behaviors of these deformable objects with other substrates. In this work, three surface-active species including CTAC, Pluronic F-127, and SDS were chosen as model surfactants to investigate the effect of the surfactants on the hydrophobic interaction between bubbles (or oil droplets) and PS surfaces via direct force measurements using the bubble/drop probe AFM technique. The molecular structures of these three surfactants are shown in Figure 2.1B. During the force measurements, the approaching velocity of the bubble/drop probe was set at 1 μm/s, and the maximum load force was fixed at 35 nN. During the interaction between air bubbles (or PFO droplets) and the PS1M surface in a 1 M NaCl solution (Figure 2.7, Figure S2.2), the jump-in behavior and attachment of PS-bubble (or PS-oil droplet) were observed. In contrast, Figure 2.8A, C, E shows the interaction force profiles measured between air bubbles and PS1M surfaces in a 1 M NaCl solution with the addition of 0.3 mM CTAC, 0.3 mM FC-127, and 1 mM SDS, respectively.

Figure 2.8B, D, F shows the interaction force profiles between PFO droplets and PS1M surfaces in a 1 M NaCl solution in the presence of 0.3 mM CTAC, 0.3 mM FC-127, and 1 mM SDS, respectively. The results in Figure 2.8 demonstrate that with the addition of the three types of surfactants (i.e., CTAC, Pluronic F-127, and SDS), only pure repulsion was detected between PS1M surfaces and air bubbles or PFO droplets, and no jump-in behavior and PS-bubble (or PS-oil droplet) attachment were observed. During the above interaction force measurements, the EDL repulsion was significantly suppressed under high salinity conditions (1 M NaCl), thus the VDW forces and hydrophobic interaction play important roles in the surface forces between the PS1M surfaces and air bubbles or PFO droplets. Without the surface-active species, the attractive hydrophobic interaction was sufficiently strong and could overcome the repulsive VDW force to drive the air bubble or oil droplet to jump into contact with the PS surfaces (Figure 2.7, Figure S2.2). Interestingly, in contrast, the addition of CTAC, FC-127, or SDS to the aqueous solution could completely suppress the attachment of the hydrophobic polymer and air bubbles or oil droplets. These surface-active species could adsorb to the surfaces of the air bubble or oil droplet and PS surfaces, and the interfacial film of these adsorbed surface-active species could lead to an additional strong steric repulsion that would prevent the attachment of the bubbles or oil droplets and the PS surfaces, as detected in the AFM force measurements in Figure 2.8.

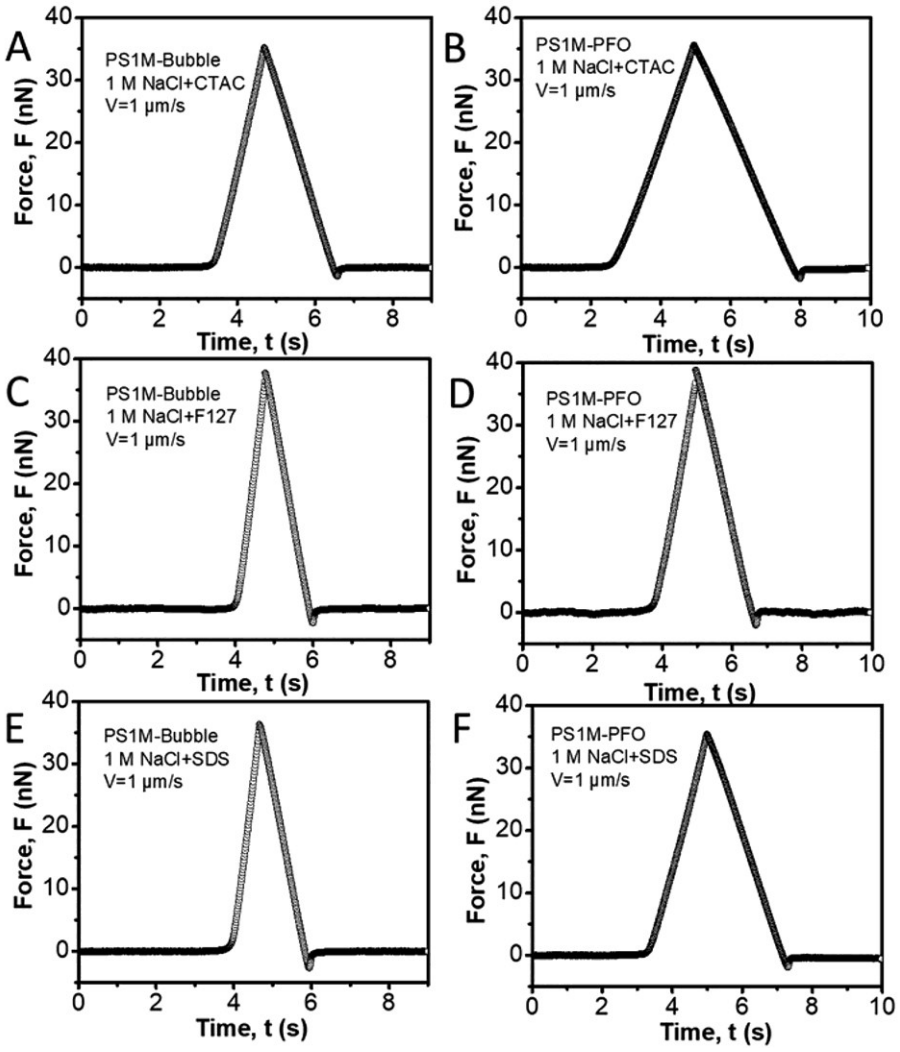

Figure 2.8. Interaction force profiles measured between air bubbles (bubble radius R0 = 69 μm) and PS1M surfaces in 1 M NaCl with different surfactants: (A) 0.3 mM CTAC, (C) 0.3 mM FC-127, and (E) 1 mM SDS. Interaction force profiles between PFO droplets (drop radius R0 = 63 μm) and PS1M surfaces in 1 M NaCl with different surfactants: (B) 0.3 mM CTAC, (D) 0.3 mM FC-127, and (F) 1 mM SDS.

2.3.2.4 The Effect of Approaching Velocity (Hydrodynamic Conditions).

Hydrodynamic conditions play an important role in many colloidal and interfacial phenomena. The above force measurements were all conducted at low driving velocity of the

bubble/drop probe, in which the hydrodynamic pressure could be neglected compared with the other interactions involved. In this work, the effect of hydrodynamic conditions on the measured surface forces was investigated by varying the driving velocity of the bubble/drop probe. Figure 2.9A shows the force profiles measured between air bubbles and PS1M in 1 M NaCl at different driving velocities of 5, 10, and 30 μm/s. With an increasing approaching velocity of the air bubbles from 5 μm/s to 30 μm/s, strong repulsion needs to be overcome before the bubbles could jump into contact with the PS1M surfaces. Thus, the repulsive hydrodynamic pressure places an additional resistance to impede the attachment of bubbles and hydrophobic polymers, while the hydrophobic interaction between air bubbles and PS1M surfaces is sufficiently strong to overcome the repulsive VDW and hydrophobic interactions to achieve the bubble-polymer attachment.

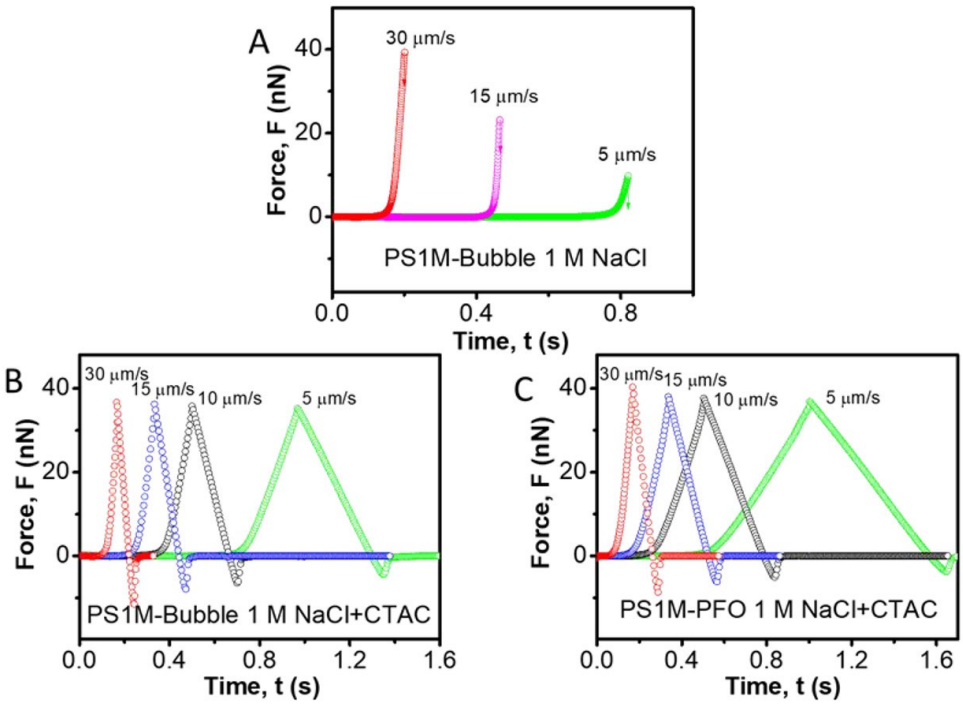

Figure 2.9. Interaction force profiles measured (A) between air bubbles (bubble radius R0 = 65 μm) and PS1M surfaces in 1 M NaCl (without surfactants), (B) between air bubbles (bubble

radius R0 = 69 μm) and PS1M surfaces, and (C) between PFO droplets (drop radius R0 = 71 μm) and PS1M surfaces at different interaction velocities in a 1 M NaCl solution with 0.3 mM CTAC.

The interaction forces of PS1M and air bubbles or PFO droplets in 1 M NaCl with 0.3 mM CTAC solution were also measured under different approaching velocities (i.e., 5, 10, 15, 30 μm/s) of the bubble/drop probe, as shown in Figure 2.9B,C. Compared with the results with an approaching velocity of 1 μm/s (Figure 2.8), it can be seen that increasing the approaching velocity of the bubbles and oil droplets could not lead to the bubble/drop attachment to the hydrophobic polymer surfaces. It is noted that obvious adhesion was detected during the separation process, and the adhesion became stronger under higher driving velocity. Such adhesion detected during the separation process of the bubble/droplet from the hydrophobic polymer surfaces was due to a so-called hydrodynamic suction effect, which was not caused by the bubble/droplet- polymer adhesive contact. The above results indicate that in addition to surface forces, hydrodynamic interactions play an important role in influencing the interactions between polymers and deformable gas bubbles or liquid droplets.

2.4 Conclusions

In this work, the interaction forces between a model hydrophobic polymer, polystyrene of different molecular weights, and air bubbles or oil droplets in aqueous solutions have been systematically characterized for the first time. A high salinity condition (1 M NaCl) was used to eliminate the presence and effect of possible nanobubbles on the PS surfaces and suppress the electrical double layer interaction to clearly highlight the role of the hydrophobic interaction in the overall surface interactions. The effects of polymer molecular weight, solvent (i.e., addition of ethanol to water), the presence of surface-active species (surfactants), and hydrodynamic

conditions were investigated. The direct force measurements and theoretical calculations, based on the Reynolds lubrication theory and augmented Young−Laplace equation by including the effect of disjoining pressure, reveal the critical roles of the surface forces and hydrodynamic interactions in the interactions between hydrophobic PS surfaces and deformable bubbles/droplets. PS surfaces of different molecular weights possess the same surface hydrophobicity. It was found that the PS590 and PS810 showed slightly weaker hydrophobic interactions with air bubbles or PFO droplets, compared to PS of higher molecular weight (i.e., PS1110, PS2330, PS46300, and PS1M). Such slightly weaker hydrophobic interaction of viscous PS of low molecular weights is possibly due to (1) more flexible chain mobility of PS with low molecular weight in the viscous state at room temperature (i.e., PS590 and PS810) and (2) increased surface roughness of PS590 and PS810 surfaces in 1 M NaCl as compared to that of the PS surfaces of higher molecular weight (i.e., PS1110, PS2330, PS46300, and PS1M). It was found that the hydrophobic interaction between PS1M and air bubbles in a 1 M NaCl aqueous solution with 10 vol % ethanol was weaker than that in the pure aqueous solution. The above effects (e.g., molecular weights of polymers, addition of miscible solvent of lower polarity to water) on the hydrophobic interactions are most likely achieved by influencing the structuring/ordering of water molecules close to the hydrophobic surfaces. The addition of three types of surfactants (i.e., CTAC, FC-127, or SDS) to the aqueous media was able to completely suppress the attachment of the hydrophobic polymer and air bubbles or oil droplets, which was most likely caused by the additional steric repulsion due to the adsorbed surface-active species at various bubble/polymer/oil interfaces. It was also found that, in addition to the various surface forces, hydrodynamic conditions also significantly influence the interactions of hydrophobic polymers and deformable objects (bubbles, droplets). The higher the approaching velocity of

bubbles or oil droplets to the polymer surfaces, the stronger the hydrodynamic repulsion, which could work jointly with the surface forces (e.g., VDW, EDL, and HB interactions) to influence the related colloidal and interfacial phenomena. Our results have improved the fundamental understanding of the interaction mechanisms between hydrophobic polymer surfaces and highly deformable bubbles or oil droplets. This work provides useful implications on developing effective approaches for modulating the related colloidal interactions in various engineering applications by tuning the solution chemistry, surface properties of substrates, or hydrodynamic conditions.

2.5 Supporting Infromation

2.5.1 The glass transition temperature (Tg) of PS with different molecular weights.

Table S2.1.The glass transition temperature (Tg) of PS with different molecular weights. [130-132]

Polymer MW and polydispersity (*Mw/Mn*)	Glass transition temperature，Tg（℃）
PS 590 (≤ 1.1)	~ -46
PS 810 (≤1.12)	~ -2
PS 1110 (≤1.12)	~ 32
PS 2330 (≤ 1.1)	~ 69
PS 46300 (≤1.03)	~ 88
PS 1M (≤ 1.1)	~ 107

2.5.2 Interaction force curves

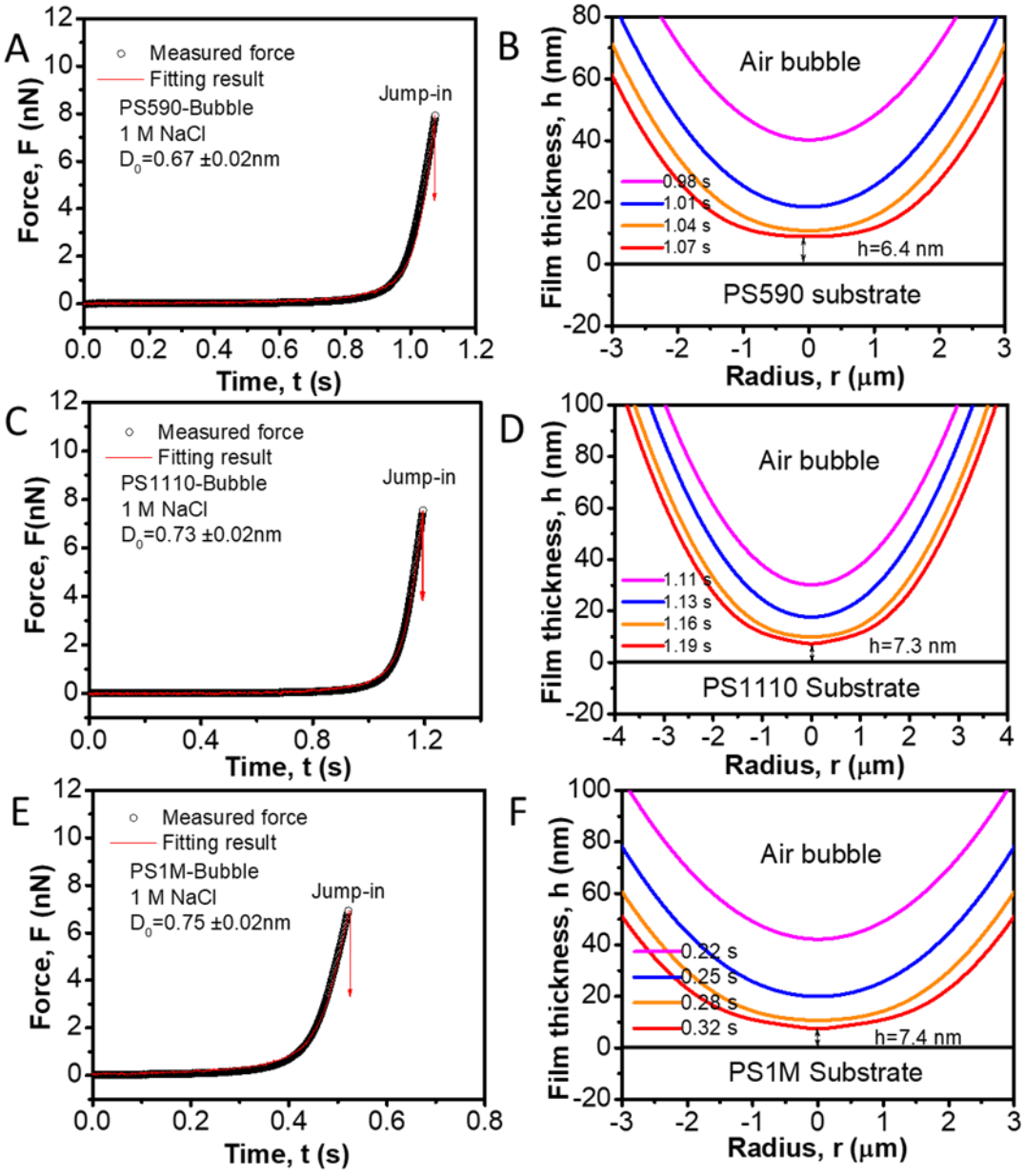

Figure S2.1. (A, C, E) Interaction force curves measured between air bubbles and PS surfaces of different molecular weights: (A) PS590 (bubble radius R_0 = 65 μm), (C) PS1110 (R_0 = 64 μm), and (E) PS1M (R_0 = 69 μm). Open symbols are the experimentally measured data and the red curves are the theoretical fitting results based on the SRYL model. (B, D, F) Evolution of the

bubble profiles during the bubble-PS approaching process where the red curve denotes the bubble profiles at the minimal separation before "jump in" behavior.

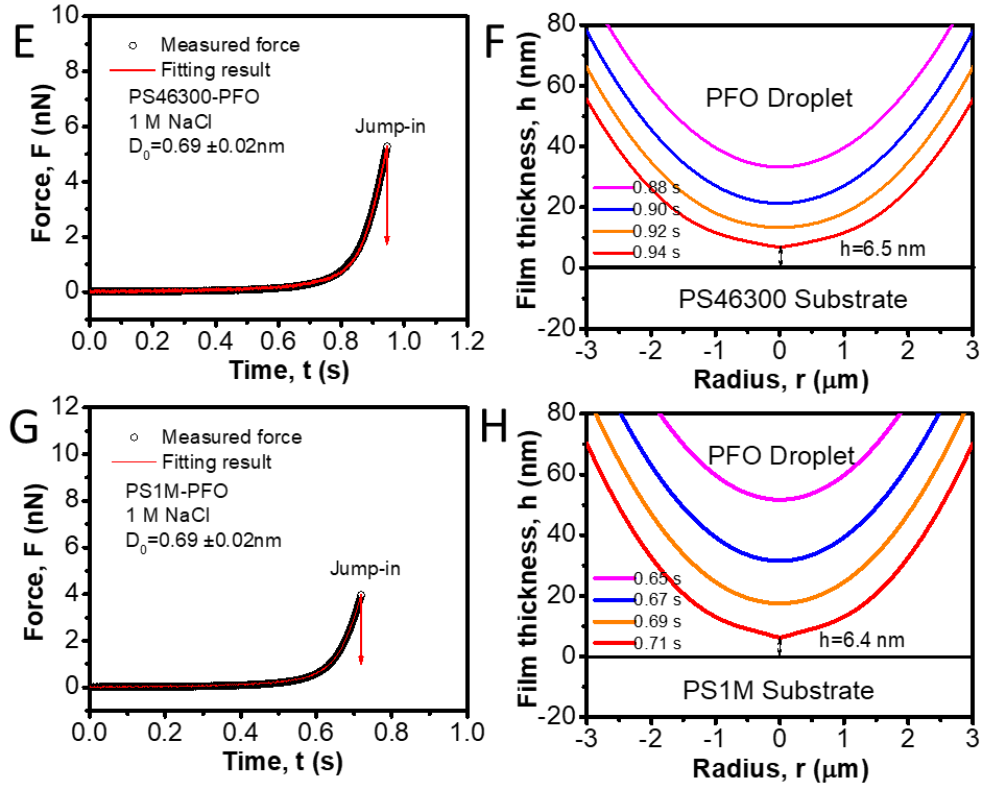

Figure S2.2. (A, C, E, G) Interaction force curves measured between PFO droplet and PS surfaces of different molecular weights: (A) PS590 (radius R_0 = 63 μm), (C) PS1110 (R_0 = 62 μm), (E) PS46300 (R_0 = 69 μm), and (G) PS1M (R_0 = 70 μm). Open symbols are the experimentally measured data and the red curves are the theoretical fitting results based on the SRYL model. (B, D, F, H) Evolution of the droplet profiles during the PFO-PS approaching process where the red curve denotes the bubble profiles at the minimal separation before "jump in" behavior.

CHAPTER 3. Surface Interaction Mechanisms of Air Bubbles, Asphaltenes and Oil Drops in Aqueous Solutions with Implications for Interfacial Engineering Processes

3.1 Introduction

Asphaltenes are frequently present in crude oils and many oil-based products, as one of the most problematic components. Asphaltenes are known as a solubility class, with good solubility in aromatic solvents such as toluene but poor solubility in alkane solvents like heptane or pentane. Asphaltenes commonly adsorb to oil/water/solid interfaces in various engineering processes, which alters their characteristics such as oil/water interfacial tension and surface wettability of minerals.[133-138] The wetting property of mineral surfaces and the formation and destabilization of oil-water emulsions significantly impact oil production processes. Thus, the adsorption of interface-active species (e.g., asphaltenes) to the oil/water/solid interfaces and their interfacial interactions have attracted much attention,[79, 109, 139-142] which is crucial to industrial processes such as bitumen extraction in both a fundamental and practical sense,[44, 143] froth flotation,[144] oil/water separation, and water treatment.[102-105, 145] The interfacial activities of asphaltenes are generally attributed to the presence of heteroatoms (i.e., N, O, and S) and associated polar groups (e.g., carboxyl).[146-150] The presence of interface-active asphaltenes can significantly influence the interaction forces of solid particles, water-oil emulsion drops, chemical additives and bubbles involved in various engineering processes, which are further impacted by the aqueous conditions such as salinity, ion type and pH.[88, 151-154] Froth flotation has been widely applied for solid/oil/water separation

processes to remove undesired solid or liquid components (e.g., asphaltene-coated minerals or oil residues), mainly driven by the forces among gas bubbles, solid particles, oil drops or organic species in the surrounding fluid media. [155] Therefore, it is critical to quantify the surface forces of air bubbles and oil-contaminated solids or oil droplets containing interface-active species like asphaltenes.

Over the past two decades, various nanomechanical tools such as surface forces apparatus (SFA) and atomic force microscope (AFM) have been applied to measure the intermolecular forces of systems involving asphaltenes and asphaltene-model-compounds in various fluid media.[31-32, 44, 88, 156-161] The SFA technique was employed to quantitatively characterize the surface forces of asphaltenes in both organic and aqueous media, which demonstrated that asphaltenes modified the wettability of mineral surfaces and that the solution salinity and pH affected the interactions forces of asphaltenes.[26, 31-32] Colloidal probe AFM was used to measure the surface forces of asphaltenes and silica in aqueous media, and the results showed that the surface charge characteristics of silica were modified due to the adsorption of asphaltenes.[151] Another AFM technique, so-called drop/bubble probe AFM, has been used to quantify how oil droplets interacted in aqueous media or water droplets interacted in oil media, or a liquid drop interacted with a solid substrate when the systems contained asphaltenes; these measurements are directly linked to how emulsions with asphaltenes interact in complicated fluid media as well as their stabilization mechanism at the nanoscale.[88, 156] Nevertheless, the quantitative understanding of the interactions among gas bubbles, asphaltenes and emulsion droplets with asphaltenes remains very limited.

In this research, the surface forces of air bubbles and asphaltenes in various water solutions have been characterized by employing an integrated thin film drainage apparatus (ITFDA), and the forces of air bubbles and oil droplets with asphaltenes in aqueous solutions have been quantified through a bubble probe AFM technique. The effects of solution salinity, pH, type of ions, asphaltenes concentration and interface-active species like surfactants on these surface interactions were also investigated. The experimentally obtained surface force results were theoretically analyzed using a model on the basis of expanded Young-Laplace equation and Reynolds lubrication theory. This study has advanced the fundamental understandings of bubble-asphaltenes and bubble-oil drop interaction mechanisms, with useful implications for bubbles and emulsion interactions in various chemical, environmental and petroleum engineering processes such as oil/water/solid separation and oily water treatment.

3.2 Materials and Methods

3.2.1 Materials

The asphaltenes used in this research were separated from Athabasca bitumen using a method reported previously.[26] Salts including sodium chloride and calcium chloride, ACS reagent grade, were obtained from Fisher Scientific. Silicon wafers with a layer of about 500 nm silicon dioxide were provided by the NanoFAB, University of Alberta. Milli-Q water with a resistivity of $\geqslant$18.2 MΩ·cm was used to make aqueous solutions. Hydrochloric acid and sodium hydroxide (both are ACS reagent grade) were provided by Fisher Scientific for adjusting aqueous pH. Sodium dodecyl sulphate (SDS) powder and

cetyltrimethylammonium chloride (CTAC, 25 wt % in water) were provided by Sigma-Aldrich, Canada.

3.2.2 Preparation of Asphaltene Surface

In this work, asphaltenes were first dissolved in toluene at various concentrations, and the asphaltenes-in-toluene solutions were sonicated for 20 minutes. The asphaltenes solutions were then filtered using 0.2 μm PTFE membrane. Asphaltenes surfaces were prepared by spin-coating 100 ppm asphaltenes solution on silica substrate at 2000 rpm for 40 s to prepare uniform films. The prepared asphaltenes films were stored under vacuum for over 12 hours to remove residual toluene.

3.2.3 Air Bubble-Asphaltenes Surface Force Measurements using Integrated Thin Film Drainage Apparatus (ITFDA)

In order to characterize the interactions of air bubbles and asphaltenes, the surface forces of air bubbles and asphaltenes surfaces under various aqueous solution conditions were measured via an ITFDA. The typical experimental procedure for measuring the forces between an air bubble and a flat substrate using an ITFDA is illustrated in Fig. 3.1A. Briefly, an air bubble was produced using a gastight syringe and attached to a glass capillary tube with inner radius 0.74 ± 0.05 mm submerged in a glass cell containing the desired aqueous solution. The flat substrate sample was fixed on the sample holder which was supported by a bimorph cantilever. When the bubble approached the sample surface driven by a motorized actuator, the forces experienced by the sample substrate would cause the deflection of the bimorph with piezoelectric property, leading to an electrical potential response which was further translated into the force information between the air bubble and substrate based on a pre-calibrated relation of force and electrical potential

response of the bimorph. The interaction cycle of the bubble and substrate surface was monitored using a camera. In a typical measurement, a bubble was moved to approach a flat asphaltenes surface at a speed of 100 μm/s until contact, and the bimorph spring detected almost negligible signal (Figure 3.1B(1)). Then the air bubble was driven to further press against the asphaltenes surface till a desired position was reached, and the bimorph spring simultaneously detects the forces through the electrical potential signals (Figure 3.1B(2)). The air bubble was kept in contact with the asphaltenes surface at the desired position for 5 s; during this period, the force of two interacting surfaces was constant (Figure 3.1B(3)). The bubble was then retracted from the asphaltenes surface at a speed of 100 μm/s, and the interaction forces decreased and turned from repulsive to attractive (from positive to negative values), while the bubble was elongated consequently as visualized from the camera (Figure 3.1B(4)). When the driven force exceeded some critical value, the bubble would suddenly detach from the asphaltenes surface (Figure 3.1B(5)), and then its surface adhesion force was determined.

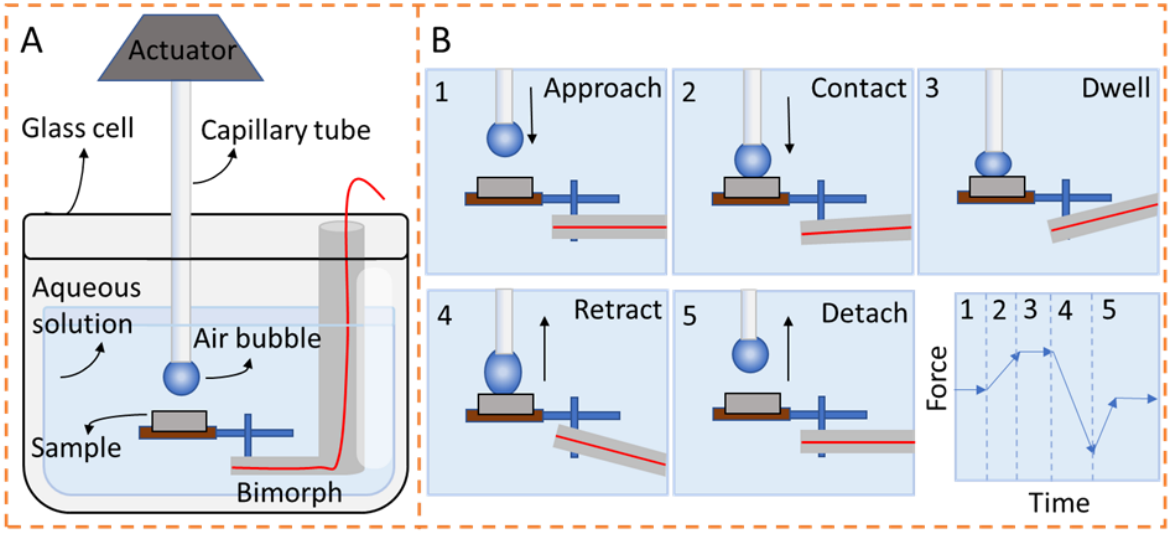

Figure 3.1. (A) Schematic of typical experimental setup for measuring the forces when an air bubble interacts with a flat substrate surface (sample) using an integrated thin film drainage apparatus (ITFDA). (B) Schematics of a typical experiment protocol of measuring the bubble-substrate interaction forces.

3.2.4 Zeta Potential Measurements

A Malvern Zetasizer Nano ZSP device was used to determine the zeta potential values of toluene droplets with different concentrations of asphaltenes suspended in aqueous media. The toluene-in-water emulsion suspensions were obtained by introducing 0.5 mL of asphaltenes-in-toluene solutions (of various asphaltenes concentrations) to 10 mL NaCl solution, which was tightly sealed and then under sonication for 20 min.

3.2.5 Air Bubble-Oil Drop Surface Force measurements via AFM

A bubble probe AFM technique, based on an Asylum Research MFP-3D AFM system supported on a Nikon Ti-U inverted microscope, was employed to measure the interaction forces between air bubbles and toluene droplets containing asphaltenes across an aqueous solution medium. Figure 3.2 shows the illustration of a typical experimental configuration for measuring surface forces using a bubble probe AFM technique. In a typical bubble/drop force experiment, the bottom glass slide of a fluid cell was immersed in 10 mM octadecyltrichlorosilane (OTS) in toluene for a short time (e.g., 10 s) to achieve a water contact angle of 30° to 50°, which was used to anchor air bubbles and toluene droplets. Air bubbles or toluene droplets were obtained by purging air or toluene using an ultrasharp glass capillary into a desired aqueous medium and then immobilized

on hydrophobized glass surface in the fluid cell. A custom-made tipless silicon cantilever (rectangular shape: 400 μm × 70 μm × 2 μm) was used for preparing the bubble probe, and its end carried a round patch (radius 32.5 μm) deposited with 30 nm gold film which was hydrophobized by immersion in 10 mM 1-decanethiol-in-ethanol solution for over 12 hours so it would have higher surface hydrophobicity than the glass substrate to picking up air bubble.[74] The spring constant of the AFM cantilever was calibrated using the Hutter method.[111] A bubble probe was prepared by driving the tipless cantilever to get close to and then attach a suitable bubble (radius 35−90 μm) supported on the glass substrate, and then to carefully lift the bubble as illustrated in Figure 3.2B. All the surface force tests were carried out under a fixed driving speed (i.e., 1 μm/s) to reduce the effect of hydrodynamic interaction, and the highest compression load was 10 nN.[74] The changes of surface forces with time and the cantilever displacement were recorded by the Asylum Research software as further theoretically analyzed using a model below.

It is noted that in this study, our main focus was to characterize the interactions of air bubbles, asphaltenes and asphaltenes-toluene droplets in aqueous media. To ensure that our measurements were conducted under conditions that were representative of the quasi-equilibrium state, we aged the asphaltenes surfaces and asphaltene-toluene droplets in desired aqueous solutions for a certain time (i.e., 20 min) before conducting the surface force measurements. In this work, for each experimental condition, all force measurements were repeated at least three times using three independently prepared samples of air bubbles, asphaltenes surfaces, or asphaltenes-toluene droplets to ensure data reproducibility.

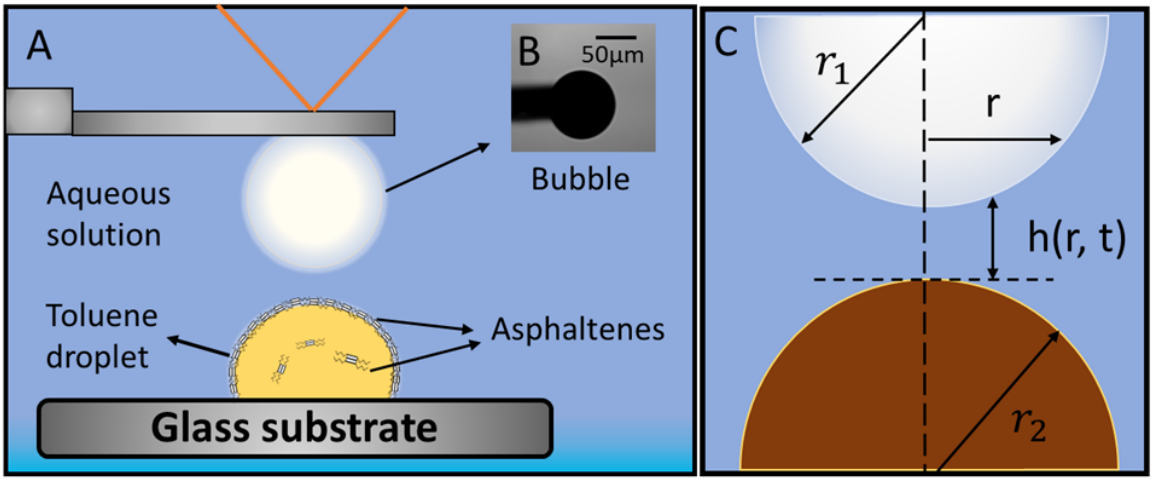

Figure 3.2. (A) Illustration of representative experiment configuration for measuring the forces of a bubble and a toluene droplet containing asphaltenes by employing the bubble probe AFM technique. (B) A picture showing an air bubble probe (radius ~53 μm). (C) Illustration of confined water film profile with between an air bubble (radius r_1) and a toluene droplet (radius r_2) with gap distance thickness $h(r, t)$ which varies with time t and radial coordinate r.

3.2.6 Theoretical Model for Analyzing the Surface Forces

The experimentally measured force data using AFM was theoretically analyzed using a Stokes-Reynolds-Young-Laplace (SRYL) model based on Reynolds lubrication theory and extended Young-Laplace equation by taking account of the disjoining pressure effects.[72-74, 162] Assuming the interface of bubble and droplet with the surrounding fluid has immobile hydrodynamic boundary condition, the dynamic drainage process and change of confined water film thickness $h(r, t)$ between bubble and toluene droplet can be analyzed using the Reynolds lubrication equation (i.e., eq 3.1),[82, 84, 87, 163]

$$\frac{\partial h(r,t)}{\partial t} = \frac{1}{12\mu r}\frac{\partial}{\partial r}\left(rh^3 \frac{\partial p(r,t)}{\partial r} \right) \tag{3.1}$$

where μ is viscosity of the liquid medium, *h(r, t)* is the bubble-droplet distance or liquid film thickness, *r* is the separation between a selected location and the central axis as illustrated in Figure 3.2C, *t* is time, and *p(r, t)* is the excessive hydrodynamic pressure within the confined aqueous film as compared to the bulk liquid medium. Previous studies have shown that when asphaltenes are present in the oil phase suspended in an aqueous phase, asphaltenes tend to build up a viscoelastic "protective" layer at the oil/water interface because of their strong intermolecular attraction and self-aggregation which stabilizes the emulsion droplets.[26, 140, 164] Therefore, when air bubbles interact with an oil droplet containing asphaltenes, the surface deformation of the bubble will be much more significant than the asphaltene-toluene drop, in other words, the asphaltene-toluene drop could be approximately considered as a relatively "rigid particle" compared to the air bubble. The bubble surface deformation is correlated to the Laplace pressure within the bubble, hydrodynamic pressure *p(r, t)*, and overall disjoining pressure *Π* via the extended Young-Laplace equation as shown in eq 3.2,[86, 163]

$$\frac{\gamma}{r}\frac{\partial}{\partial r}\left(r\frac{\partial h(r,t)}{\partial r} \right) = \frac{2\gamma}{R_0} - p(r,t) - \Pi\left[h(r,t) \right] \tag{3.2}$$

where γ is the air/water surface tension, $R_0 = (1/r_1 + 1/r_2)^{-1}$ is the harmonic mean of bubble radius r_1 and droplet radius r_2, *p(r, t)* is the hydrodynamic pressure, and $\Pi\left[h(r,t) \right]$ is the overall disjoining pressure. The overall disjoining pressure *Π* arises from various surface interactions such as electrostatic double layer (EDL), van der Waals (VDW), and hydrophobic (HB) interactions, as shown in eq 3.3,[79, 109]

$$\Pi\left[h(r,t)\right] = \Pi_{VDW} + \Pi_{EDL} + \Pi_{HB} + ... \tag{3.3}$$

where Π_{VDW}, Π_{EDL}, and Π_{HB} are the disjoining pressures arising from the VDW, EDL, and HB forces, respectively. Π_{VDW} and Π_{EDL} are two ubiquitous interactions in the DLVO theory for colloidal systems. Π_{VDW} arises from the VDW interaction and can be given by eq 3.4,[74]

$$\Pi_{VDW} = -\frac{A_H}{6\pi h^3(r,t)} \tag{3.4}$$

where A_H is the Hamaker constant that can be calculated based on the Lifshitz theory. The Hamaker constant for materials 1 and 2 interacting in medium 3, A_{132}, can be estimated using an approximated expression shown in Eq 3.5.[79]

$$A_H \approx \frac{3}{4}k_B T\left(\frac{\varepsilon_1-\varepsilon_3}{\varepsilon_1+\varepsilon_3}\right)\left(\frac{\varepsilon_2-\varepsilon_3}{\varepsilon_2+\varepsilon_3}\right) + \frac{3h\nu_e}{8\sqrt{2}}\frac{\left(n_1^2-n_3^2\right)\left(n_1^2-n_3^2\right)}{\sqrt{\left(n_1^2+n_3^2\right)}\sqrt{\left(n_2^2+n_3^2\right)}\left\{\sqrt{\left(n_1^2+n_3^2\right)}+\sqrt{\left(n_2^2+n_3^2\right)}\right\}} \tag{3.5}$$

where k_B is the Boltzmann constant, T is thermodynamic temperature, h_p is Planck's constant, υ_e is the electronic absorption frequency, ε_i is the dielectric constant of material *i*, and n_i is the refractive index of the material *i*. The Hamaker constant for the air bubble-water-toluene (with asphaltenes) system was estimated as -1.28×10^{-20} J using the parameters in Table S3.1, suggesting the VDW interaction is repulsive.[74, 79]

The EDL interaction is mostly influenced by charge characteristics of surfaces and electrolyte condition of the aqueous solutions.[165] For the asymmetric air bubble-water-toluene (with asphaltenes) system, the Π_{EDL} is given by eq 3.6,[166-167]

$$\Pi_{EDL} = \frac{2\varepsilon_0\varepsilon\kappa^2\left[\left(e^{+\kappa h}+e^{-\kappa h}\right)\varphi_1\varphi_2 - \left(\varphi_1^2+\varphi_2^2\right)\right]}{\left(e^{+\kappa h}-e^{-\kappa h}\right)^2} \tag{3.6}$$

where 1/κ is the Debye length and $1/\kappa = (2\rho_0 e^2 / \varepsilon_0 \varepsilon k_B T)^{-1/2}$ (for the 1:1 salt case); ρ_0 is the ion number density in the aqueous solution; φ_1 and φ_2 are the surface potentials of the air bubble and toluene droplet (with asphaltenes), respectively; *e* is the elementary charge, ε_0 is the vacuum permittivity and ε is the dielectric constant of the liquid medium.

The disjoining pressure arising from hydrophobic interaction for the bubble-water-oil droplet system is given by eq 3.7,[74]

$$\prod_{HB} = -\frac{C_0}{2\pi D_0} \exp\left(-\frac{h(r,t)}{D_0}\right) \tag{3.7}$$

where C_0 is a constant and $C_0 / 2\pi = \gamma_{(air-water)} + \gamma_{(oil-water)} - \gamma_{(oil-air)}$, and D_0 is the length characteristic decay length of hydrophobic interaction. $\gamma_{(air-water)}$ is 72.8 mN/m at 20℃. The interfacial tension $\gamma_{(oil-water)}$ and $\gamma_{(oil-air)}$ in the time frame of AFM force measurements were determined by interfacial tension measurements.

The total interaction force F(t) is determined using eq 3.8 based on the Derjaguin approximation.[86, 113, 117, 124]

$$F(t) = 2\pi \int_0^\infty \left[p(r,t) + \prod\left(h(r,t)\right)\right] r dr \tag{3.8}$$

3.3 Results and Discussion

3.3.1 Asphaltene Surfaces.

AFM was used to image the topographic characteristics of the asphaltenes surfaces, and a typical AFM image of asphaltenes surfaces is displayed in Figure S3.1. The root-mean-square (rms) roughness was determined as 0.30 nm, indicating that the prepared

asphaltenes surfaces were smooth, thus the surface roughness of asphaltenes had negligible effect on the surface force measurements using ITFDA. The water contact angle on the asphaltenes surfaces in air showing the static water drop was found to be ~100°, as shown in Figure S3.1B, indicating the asphaltenes surface is hydrophobic.

3.3.2 Air Bubble-Asphaltenes Surface Force Measurements using ITFDA

An ITFDA was applied to characterize the forces of air bubbles interacting with asphaltenes surfaces in an aqueous medium, and the effects of solution chemistry (e.g., salt concentration, pH) were investigated. Figure 3.3A shows the snapshots of air bubbles interacting with asphaltenes surfaces under various aqueous solution conditions captured at the different stages (as illustrated in Figure 3.1) in the ITFDA tests. The dynamic interaction processes are displayed in the Supplementary Video S3.1-S3.4. It was found from Video S3.1 and S3.2 that at low salt concentration condition (i.e., 1 mM NaCl, pH 5.6 and pH 10), no obvious "jump in" behavior was observed and the air bubble was deformed when it was pressed against the asphaltenes surfaces; in contrast, when the salt concentration was relatively high (i.e., 100 mM NaCl, pH 5.6 and pH 10, Video S3.3 and S3.4), an obvious "jump in" behavior (viz., the bubble jumped to attach the asphaltenes surface to form the air-water-asphaltenes three phase contact) was observed. It was also found that the air bubbles were stretched during the retraction processes (Figure 3.3A, Video S3.1-S3.4) which was more obvious for the high salinity cases, indicating the strong bubble-asphaltenes adhesion. Figure 3.3B-D displays the force measurement results for air bubbles interacting with asphaltenes surfaces in (B) 1 mM NaCl at pH 5.6, (C) 100 mM NaCl at pH 5.6, (D) 1 mM NaCl at pH 10 and (E) 100 mM NaCl at pH 10,

respectively. The surface forces measured under the different aqueous solution conditions show similar profiles. When the air bubbles were driven to approach the asphaltenes surfaces, no obvious force was detected by the bimorph. With the surface separation decreased till bubble-asphaltenes contact, the air bubbles were pressed against the asphaltenes surfaces, and repulsive forces were detected. When the air bubbles were kept under the maximum repulsion for 5 s, the repulsion forces remained almost constant. During the retraction process, the repulsive forces gradually decreased and changed to attraction which was accompanied with the stretching of the air bubbles (Figure 3.3A, Video S3.1-S3.4), because of the capillary bridge built between the deformed bubbles and asphaltenes surfaces. The adhesion forces were determined when the "jump out" behavior was observed. In an aqueous solution with low salt concentration (i.e., 1 mM NaCl), the adhesion force was measured to be ~0.20±0.02 mN at both pH 5.6 and pH 10, and the solution pH did not show significant influence. In contrast, when the salt concentration was relatively high (i.e., 100 mM NaCl), the adhesion force was increased to ~0.35±0.02 mN, yet the pH again did not have significant influence. The adhesion force measured under high salinity conditions was higher than that under low salinity conditions, which was mainly attributed to the suppressed EDL repulsion in aqueous solutions with high salinity.

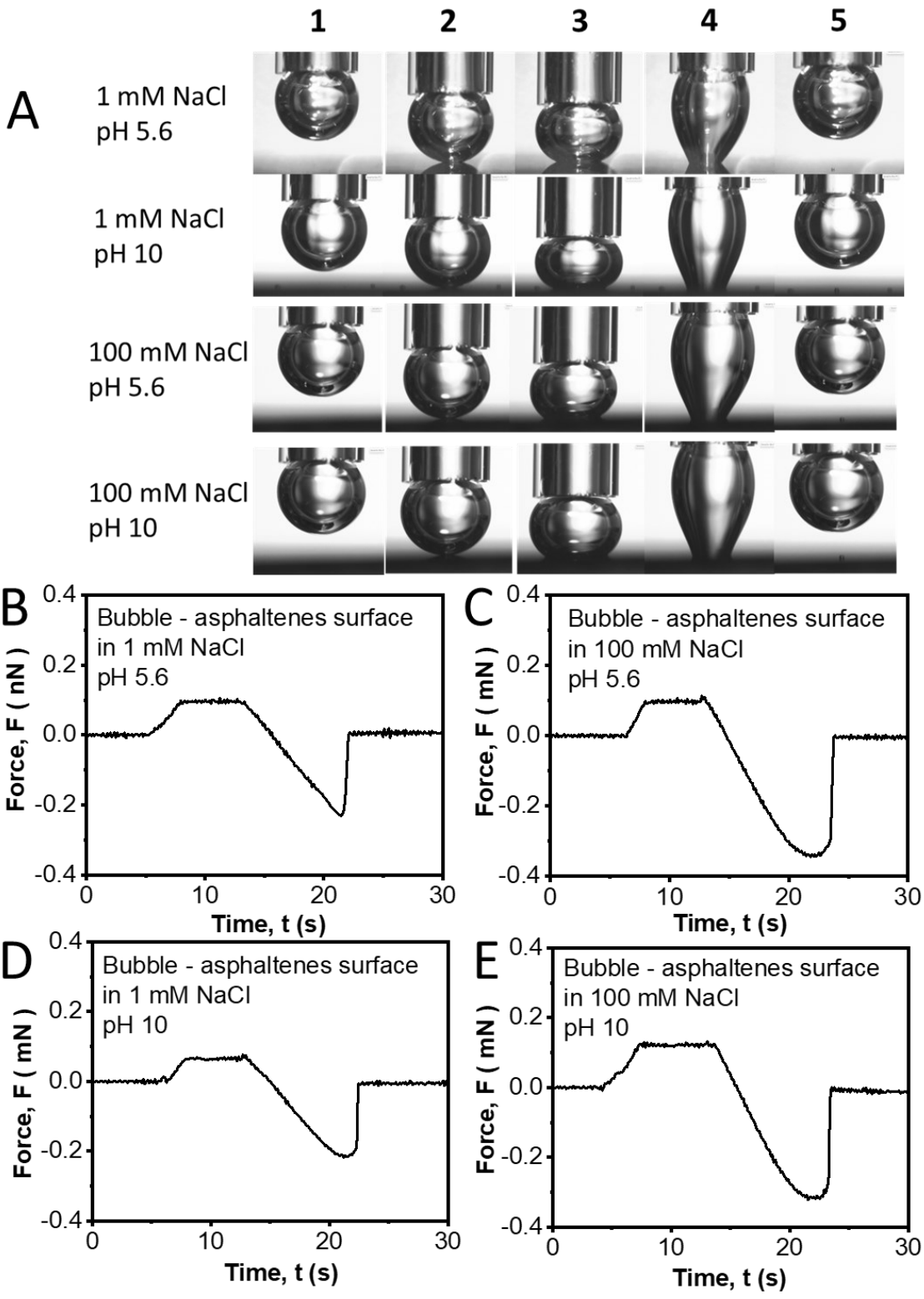

Figure 3.3. (A) Pictures of air bubbles interacting with asphaltene surfaces under various aqueous solution conditions in different stages of the ITFDA tests. (B-E) Force curves

measured during the interaction of a bubble (radius ≈1.9 mm) with an asphaltenes surface in different aqueous solutions: (B) 1 mM NaCl at pH 5.6, (C) 100 mM NaCl at pH 5.6, (D) 1 mM NaCl at pH 10, and (E) 100 mM NaCl at pH 10.

3.3.3 Surface Forces between Air Bubbles and Oil Droplets containing Asphaltenes

3.3.3.1 The Effects of Asphaltenes Concentration and Aqueous Solution Salinity

The bubble probe AFM technique was applied to quantify the forces of air bubbles interacting with oil droplets (i.e., toluene) in the absence and presence of different concentrations of asphaltenes under various aqueous solution conditions. The salt concentration was set at either 1 mM NaCl or 100 mM NaCl. The surface forces of bubbles and bare toluene droplets were first measured in an aqueous solution of 1 mM NaCl or 100 mM NaCl at pH 5.6, and the force curves are displayed in the Supporting Information Figure S3.2. Only repulsive forces were detected under both aqueous solution conditions. It is noted that the van der Waals interactions for air bubbles-water-toluene were repulsive. In 1 mM NaCl at pH 5.6, both the bubble and toluene drop surfaces were negatively charged, so that EDL force was repulsive. While in 100 mM NaCl, the EDL was much compressed (with a Debye length ~0.96 nm), and the EDL force could be neglected. Thus, the repulsive VDW interaction under both low and high salt concentration conditions and the repulsive EDL forces in low-salinity solution dominate the air bubble-water-toluene droplet interaction, preventing the surface contact.

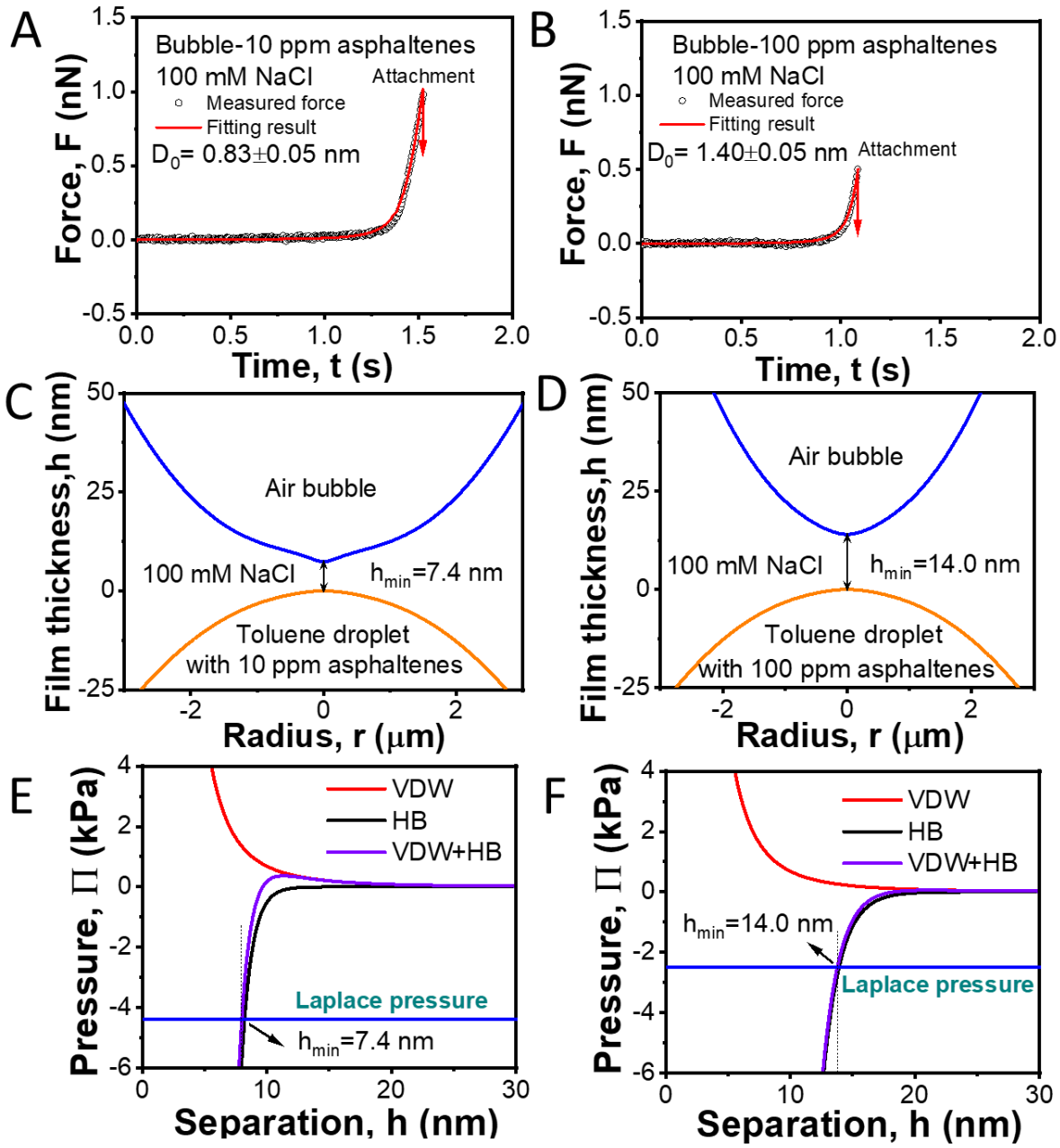

Figure 3.4. Experimentally measured force curves of air bubbles and asphaltenes-toluene droplets with (A) 10 ppm asphaltenes (bubble radius r_1 = 56 μm, oil droplet radius r_2 = 52 μm), and (B) 100 ppm asphaltenes (bubble radius r_1 = 43 μm, oil droplet radius r_2 = 50 μm) in 100 mM NaCl solution at pH 5.6 using the bubble probe AFM technique. Open symbols present the experimental results, and the solid red curves display the

theoretically fitted data. (C-D) The surface profiles of bubbles and oil droplets at the "jump in" positions during their approach when measuring the forces of air bubbles and asphaltenes-toluene drops containing (C) 10 ppm and (D) 100 ppm asphaltenes, where the blue curves denote the bubble profiles and yellow curves illustrate the droplet profiles at the minimum separation h_{min}. (E−F) Disjoining pressure curves arising from various surface interactions (i.e., HB and VDW) for the (E) 10 ppm and (F) 100 ppm asphaltenes cases.

Figure 3.4 shows the interaction behaviors of air bubbles and asphaltenes-toluene droplets in aqueous solutions with relatively high salt concentration. In Figure 3.4A, the bubble had a radius r_1 = 56 μm, and oil droplet radius was r_2 = 52 μm which contained 10 ppm asphaltenes. In Figure 3.4B, the bubble radius was r_1 = 43 μm and the oil droplet radius was r_2 = 50 μm which contained 100 ppm asphaltenes. Interestingly, different from the bare toluene droplet case (Figure S3.2), when 10 ppm or 100 ppm asphaltenes were present in the toluene droplets, after overcoming a weak repulsion force, the air bubble was observed to jump and attach to the asphaltenes-toluene droplet (referred as "jump-in" behavior). Because of the low driving speed 1 μm/s applied to the bubble probe, the effect of hydrodynamic forces was negligible.[158] The EDL interactions were also greatly suppressed in the aqueous solution of high salt concentration (i.e., 100 mM NaCl). The weak repulsion before the "jump-in" was mainly attributed to the repulsive VDW interactions, and the "jump-in" behavior must be driven by some attractive interactions. It is well known that asphaltenes are hydrophobic in nature (asphaltenes surface has water contact angle ~100° as shown in Figure S3.1) and asphaltenes adsorb to the oil/water

interface to build up a viscoelastic interfacial layer which inhibits emulsion coalescence. Thus, the hydrophobic attraction of the air bubbles and asphaltenes-toluene droplets was proposed to drive the "jump-in" behaviors. The experimental force results were fitted based on the SRYL model by including the disjoining pressure (see Figure 3.4A and 3.4B), and the hydrophobic interaction was found to show a decay length of D_0 ~0.83 nm and 1.40 nm for the bubble-oil droplet case with 10 ppm and 100 ppm asphaltenes, respectively. The bubble and drop profiles at the critical "jump in" positions during the force measurements of air bubbles and asphaltenes-oil drops with 10 ppm and 100 ppm asphaltenes are shown in Figure 3.4C and 3.4D, respectively. The minimum separation distance h_{min} of the confined thin water film was determined to be 7.4 and 14.0 nm for the 10 ppm and 100 ppm asphaltenes cases, respectively. Figure 3.4E and 3.4F display the disjoining pressure results arising from the different surface interactions (e.g., VDW, HB) for the 10 ppm and 100 ppm asphaltenes cases, respectively. These results demonstrate that (1) the addition of asphaltenes could enhance the hydrophobic attraction of air bubbles with asphaltenes-toluene droplets that was stronger than the VDW repulsion and led to "jump in" behaviors and surface contact of the two interacting objects in 100 mM NaCl, and (2) the hydrophobic attraction Π_{HB} became stronger with increasing asphaltenes concentration from 10 ppm to 100 ppm. As reported previously,[26, 140,92, 164] with increasing asphaltenes concentration, more asphaltenes could adsorb to the oil/water interface which enhanced their self-aggregation at the oil/water interface, forming more "rigid" films to protect the emulsion droplets. These behaviors could contribute to the enhanced hydrophobic interaction of oil droplets with air bubbles as detected in surface force measurements shown in Figure 3.4.

The effects of salt concentration on the interaction forces of bubbles and asphaltenes-toluene droplets have also been investigated. Figure 3.5A and 3.5B display the interaction force results between air bubbles and oil droplets containing asphaltenes concentration of 10 and 100 ppm, respectively, in 1 mM NaCl solution at pH 5.6. Only purely repulsive forces were detected under the low salinity condition as can be seen from Figure 3.5, and there was no attachment between air bubbles and asphaltenes-toluene droplets with either 10 or 100 ppm asphaltenes. Under the condition of low salt concentration (i.e., 1 mM NaCl, with Debye length ~9.6 nm), the EDL repulsion plays an important role in their bubble-oil droplets interactions. As discussed above, the VDW forces were also repulsive. Thus, the repulsive VDW forces and the long-range repulsive EDL interactions in low salinity solution could compete with the hydrophobic attraction (with the same HB decay length as that shown in Figure 3.5) between air bubbles and asphaltenes-toluene droplets, which inhibit their surface contact.

The force profiles in Figure 3.5A and 3.5B have been fitted using the SRYL theoretical model, and the surface potential of air bubbles was -25.0 mV in 1 mM NaCl at pH 5.6.[73, 168] By fitting the measured force data (open symbols) using the SRYL model (red curves), the surface potentials of the oil droplets containing 10 and 100 ppm asphaltenes were determined as -45.0±5 mV and -65.0±5 mV, respectively, in 1 mM NaCl at pH 5.6, close to the zeta potential values (Table S3.2). The oil/water interface became more negatively charged when the asphaltenes concentration in the oil phase increased, which agreed with the literature.[88] The repulsive EDL forces of air bubbles and asphaltenes-toluene droplets were strengthened by increasing the asphaltenes concentration. Figure 3.5C and 3.5D show the profiles of the confined aqueous solution

films between the air bubbles and the asphaltenes-toluene droplets under the maximum loading force (i.e., 10 nN) applied. The minimum aqueous film thickness h_{min} was determined to be 13.6 and 22.7 nm for the 10 ppm and 100 ppm asphaltenes cases, respectively, due to the competition among the repulsive VDW interaction (Π_{VDW}), repulsive EDL interaction (Π_{EDL}) and the attractive HB interaction (Π_{HB}). The corresponding disjoining pressure profiles (Π_{VDW}, Π_{EDL} and Π_{HB}) due to the three types of surface interactions are also shown in Figure 3.5E and 3.5F for the 10 ppm and 100 ppm cases, respectively.

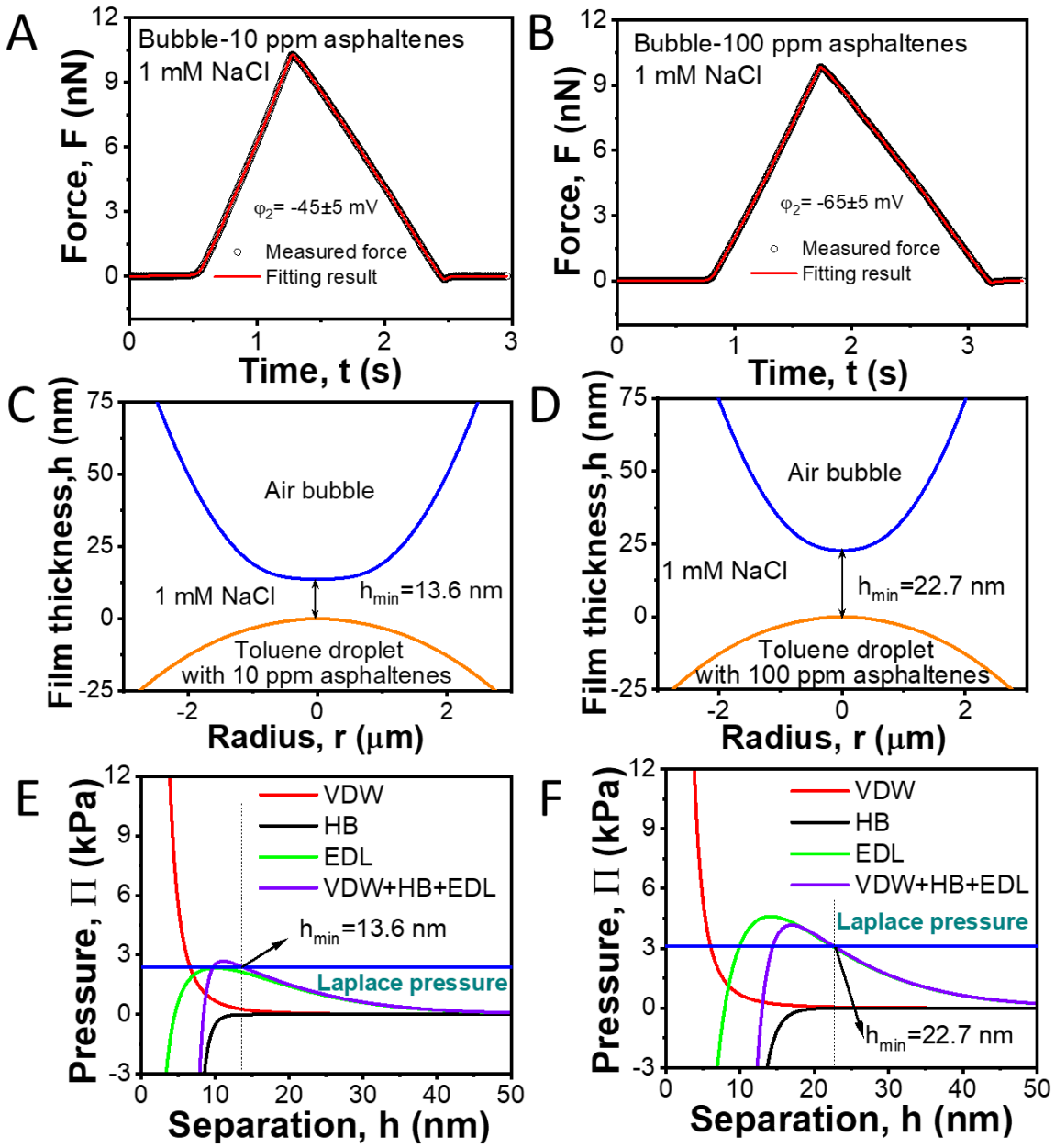

Figure 3.5. (A−C) Interaction force results for air bubbles interacting with asphaltenes-toluene droplets with (A) 10 ppm asphaltenes (bubble radius r_1 = 63 μm, oil droplet radius r_2 = 64 μm) and (B) 100 ppm asphaltenes (bubble radius r_1 = 43 μm, oil drop radius r_2 = 50 μm) in 1 mM NaCl solution (pH 5.6) using the bubble probe AFM technique. Open symbols refer to the experimental results, and the theoretical calculation results are shown in red curves. (C−D) Profile of air bubbles and asphaltenes-toluene

drops under the maximum loading force during surface approach for oil drops containing (C) 10 ppm and (D) 100 ppm asphaltenes, where the blue curves denote the bubble profiles and yellow curves illustrate the droplet profiles at the minimum separation h_{min}. (E−F) Disjoining pressure results arising from various surface forces (i.e., VDW, EDL and HB) for the (E) 10 ppm and (F) 100 ppm asphaltenes cases.

3.3.3.2 The Effect of Solution pH

The surface forces of air bubbles with oil droplets with 100 ppm asphaltenes under different pH conditions (i.e., pH 4, 7 and 10) were measured using the bubble probe AFM technique. Two salinity conditions were tested, i.e., 1 mM and 100 mM NaCl. Figure 3.6A, 3.6B and 3.6C show the measured surface force profiles in 100 mM NaCl solutions of pH 4, 7 and 10, respectively. In aqueous solutions of high salt concentration (i.e., 100 mM NaCl). the EDL interactions of air bubbles and oil droplets with 100 ppm asphaltene were greatly suppressed and became very short-ranged. The air bubbles were driven to interact with the asphaltenes-toluene droplets at 1 μm/s, and the hydrodynamic forces could be negligible as compared with other interactions. Therefore, the overall interaction forces were mainly dominated by the repulsive VDW force and attractive HB interactions. The experimentally measured interaction force profiles and theoretical calculation data using the theoretical model (Equations 3.1-3.3) are displayed as open circle symbols and solid red curves in Figure 3.6A-C, respectively. The surface force results show that after overcoming a critical repulsive force, jump-in behaviors were detected when air bubbles approached asphaltenes-toluene droplets for all the three pH cases, indicating bubble-oil droplet surface contact was achieved. The jump-in behaviors mainly resulted from the HB attraction that overcame the VDW repulsion. By analyzing the force curves based on

the theoretical model (Equations 1-3), the hydrophobic interaction showed a decay length D_0, fitted as ~1.46, 1.32, and 0.9 nm under pH 4, pH 7 and pH 10, respectively. The results indicate that increasing the hydrophobic attraction between the air bubbles and toluene droplets with 100 ppm asphaltenes could be weakened by increasing the aqueous pH. With increasing solution pH, polar groups containing heteroatoms (e.g., O, N, S) such as -COOH on asphaltenes molecules at the oil/water interface tend to face the aqueous phase and their dissociation makes the oil/water interface negatively charged, which in turn makes the asphaltenes-toluene droplet surfaces less hydrophobic, thus weakening the hydrophobic attraction with air bubbles.

The corresponding bubble and droplet profiles right before the "jump in" during the approaching process are shown in Figure 3.6D-F for the pH 4, 7 and 10 cases, respectively. The minimum separation distance h_{min} between air bubbles and asphaltenes-toluene droplets before "jump in" was determined to be 13.8 nm, 13.4 nm, and 9.0 nm at pH 4, 7 and 10, respectively. At the critical gap distance h_{min}, the total disjoining pressure was attractive which became higher than the Laplace pressure inside the bubble, causing the jump-in and contact of the air bubble to the apshaltenes-toluene droplet. The profiles of various disjoining pressure arising from the VDW and HB forces under the three different pH conditions are displayed in Figure 3.6G-I, confirming that attractive HB interaction became weakened with the h_{min} reduced when the pH increased.

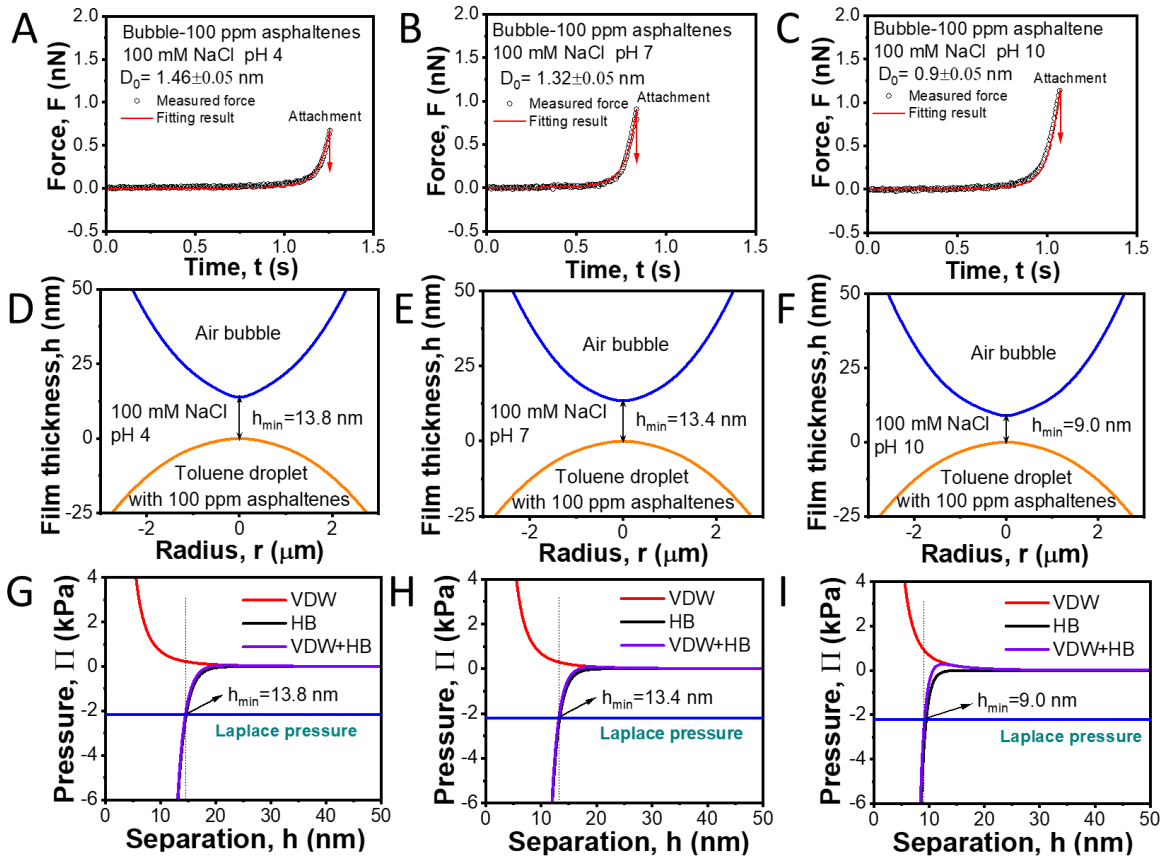

Figure 3.6. (A−C) Surface force results for air bubbles interacting with droplets of toluene-asphaltenes (100 ppm) in 100 mM NaCl with various pH conditions: (A) pH 4 (bubble radius r_1 = 58 μm, droplet radius r_2 = 54 μm), (B) pH 7 (bubble radius r_1 = 56 μm, droplet radius r_2 = 52 μm), and (C) pH 10 (bubble radius r_1 = 58 μm, droplet radius r_2 = 51 μm). Experimental results are shown in open symbols, and theoretical calculation results are shown in red curves. (D−F) Bubble and oil drop profiles at the minimum separation distance h_{min} right before "jump-in" in 100 mM NaCl with (D) pH 4, (E) pH 7 and (F) pH 10, where the blue curves denote the bubble profile and yellow curves refer to the droplet profiles at the minimum separation. (G−I) Disjoining pressure profiles arising from various VDW and HB interactions under (G) pH 4, (H) pH 7, and (I) pH 10.

Figure 3.7A-C show the surface force profiles of air bubbles interacting with toluene droplets with 100 ppm asphaltenes in 1 mM NaCl solution at pH 4, pH 7, and pH 10, respectively. No jump-in behaviors could be detected, which was mainly due to the repulsive EDL forces and VDW forces that overcame the attractive HB interactions. Analysis using the theoretical model (Equations 3.1-3.3) showed that the fitted surface potentials of oil droplets with 100 ppm asphaltenes in 1 mM NaCl at pH 4, pH 7, and pH 10 were -53 ± 5 mV, -68 ± 5 mV, and -90 ± 5 mV, respectively, close to the zeta potential values shown in Table S3.2. The thin water films between air bubbles and oil droplets under the maximum load (i.e., 10 nN) display profiles for the three pH cases in Figure 3.7D-F. The minimum separation distances h_{min} of the three cases were determined to be 18.3 nm, 24.2 nm, and 29.1 nm, respectively, at which the Laplace pressure was balanced by the overall disjoining pressure ($\Pi_{VDW} + \Pi_{EDL} + \Pi_{HB}$). Figure 3.7G-I show the calculated disjoining pressure results (i.e., Π_{VDW}, Π_{EDL} and Π_{HB}) arising from the VDW, EDL and HB interactions at pH 4, 7 and 10, respectively. As pH increased, the asphaltenes-toluene droplet became more negatively charged, leading to a strengthened repulsive EDL interaction; meanwhile the HB interaction decreased with increasing pH in 1 mM NaCl. Thus, the overall disjoining pressure became more repulsive at higher pH, resulting in thicker confined thin water film at higher pH with no bubble-oil drop attachment.

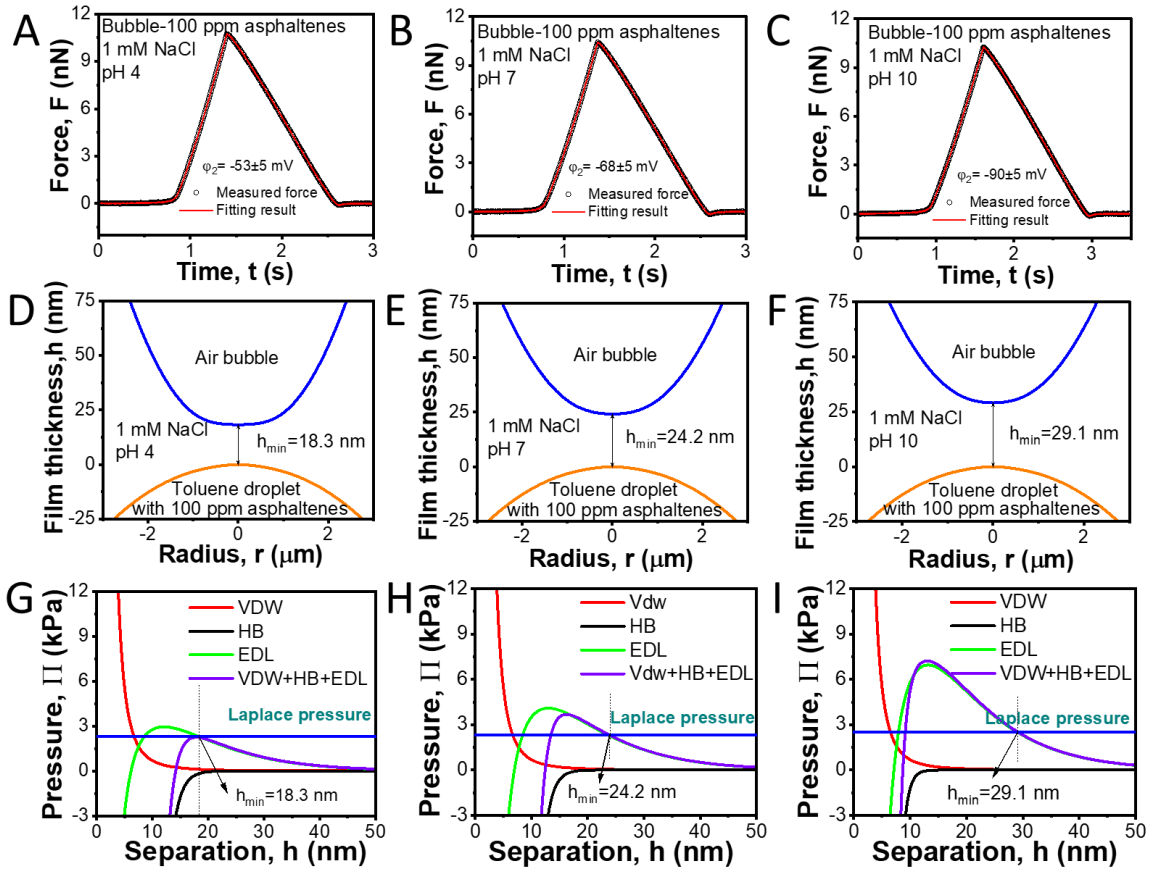

Figure 3.7. (A−C) Surface force results for air bubbles interacting with toluene-asphaltenes (100 ppm) droplets in 1 mM NaCl at various pH: (A) pH 4 (bubble radius r_1 = 62 μm, droplet radius r_2 = 55 μm), (B) pH 7 (bubble radius r_1 = 63 μm, droplet radius r_2 = 52 μm), and (C) pH 10 (bubble radius r_1 = 55 μm, droplet radius r_2 = 56 μm). Experiment results are shown in open symbols, and theoretical calculations using the model (Equations 1-3) are displayed in the red curves. (D−F) Profiles of confined aqueous solution films under the maximum load of 10 nN during the bubble-droplet approaching process in mM NaCl at (D) pH 4, (E) pH 7 and (F) pH 10, of which the blue curve presents gas bubble profiles and yellow curve shows liquid droplet shapes at the minimum separation. (G−I) Disjoining pressure results arising from VDW, EDL and HB interactions at (G) pH 4, (H) pH 7, and (I) pH 10.

3.3.3.3 Effects of Ca^{2+} ions

Ca^{2+} ions are commonly present in aqueous solutions in various engineering processes. It is important to also investigate how calcium ions affect the interactions between air bubbles and asphaltenes-toluene droplets. Figure 3.8A and 3.8B display the surface force results of air bubbles interacting with toluene-asphaltenes (100 ppm) in aqueous solutions with 100 mM NaCl at pH 5.6 and the addition of 1 and 10 mM $CaCl_2$, respectively. Jump-in and surface attachment behaviors were observed when the applied force load reached ~2.5 and 2.6 nN in aqueous solutions with 100 mM NaCl and additional 1 mM and 10 mM $CaCl_2$, respectively. within comparison with the results for air bubbles and toluene-asphaltenes (100 ppm) droplets in 100 mM NaCl without Ca^{2+}, the critical forces needed for the adhesive "jump in behavior" with the addition of Ca^{2+} ions are stronger. The interactions of Ca^{2+} ions with the polar moieties of asphaltenes such as carboxyl groups could impact the conformation of asphaltenes molecules and aggregates adsorbed at the oil/water interface and the interfacial properties.[151, 169-170] By analyzing the force results using the theoretical model (Equations 3.1-3.3), the hydrophobic interaction showed a decay length D_0 ~0.54 and 0.52 nm for the 1 and 10 mM $CaCl_2$ cases, respectively. The results suggest that increasing Ca^{2+} ion concentration led to more aggregation of the interfacial asphaltenes, which decreased the amount of hydrophobic moieties of the asphaltenes facing the aqueous phase, leading to weaker hydrophobic attraction of bubbles and asphaltenes-toluene droplets. The corresponding shapes of bubbles and asphaltenes-toluene droplets right before jump-in during the approaching process were shown in Figure 3.8C and 3.8D with the minimum separation

distances determined as 5.4 and 5.1 nm respectively for the 1 and 10 mM $CaCl_2$ cases. At such a critical distance, the hydrophobic attraction of air bubbles and asphaltenes-toluene droplet overcame the repulsive VDW force, which drove the two objects to jump into contact. The corresponding disjoining pressure results arising from the VDW and HB interactions for the cases of 1 and 10 mM $CaCl_2$ are presented respectively in Figure 3.8E-F. It should be noted that the aggregation and conformation changes of the interfacial asphaltenes induced by Ca^{2+} ions also led to repulsive steric interactions between the air bubbles and asphaltenes-toluene droplets, contributing to the stronger repulsion in Figure 3.8A and 3.8B, as compared with the case without Ca^{2+} ions in Figure 3.4B. Such complex steric interactions were included in the above theoretical analysis and the SRYL model, as no steric interaction model is suitable for the above complex interfacial interaction. Thus, it is noted that the decay lengths of the HB interactions in Figure 3.8A and 3.8B were underestimated and in practice, the attractive HB interactions overcame the VDW and steric repulsion to drive adhesive contact of air bubbles and asphaltenes-toluene droplets in 100 mM NaCl with 1 or 10 mM $CaCl_2$.

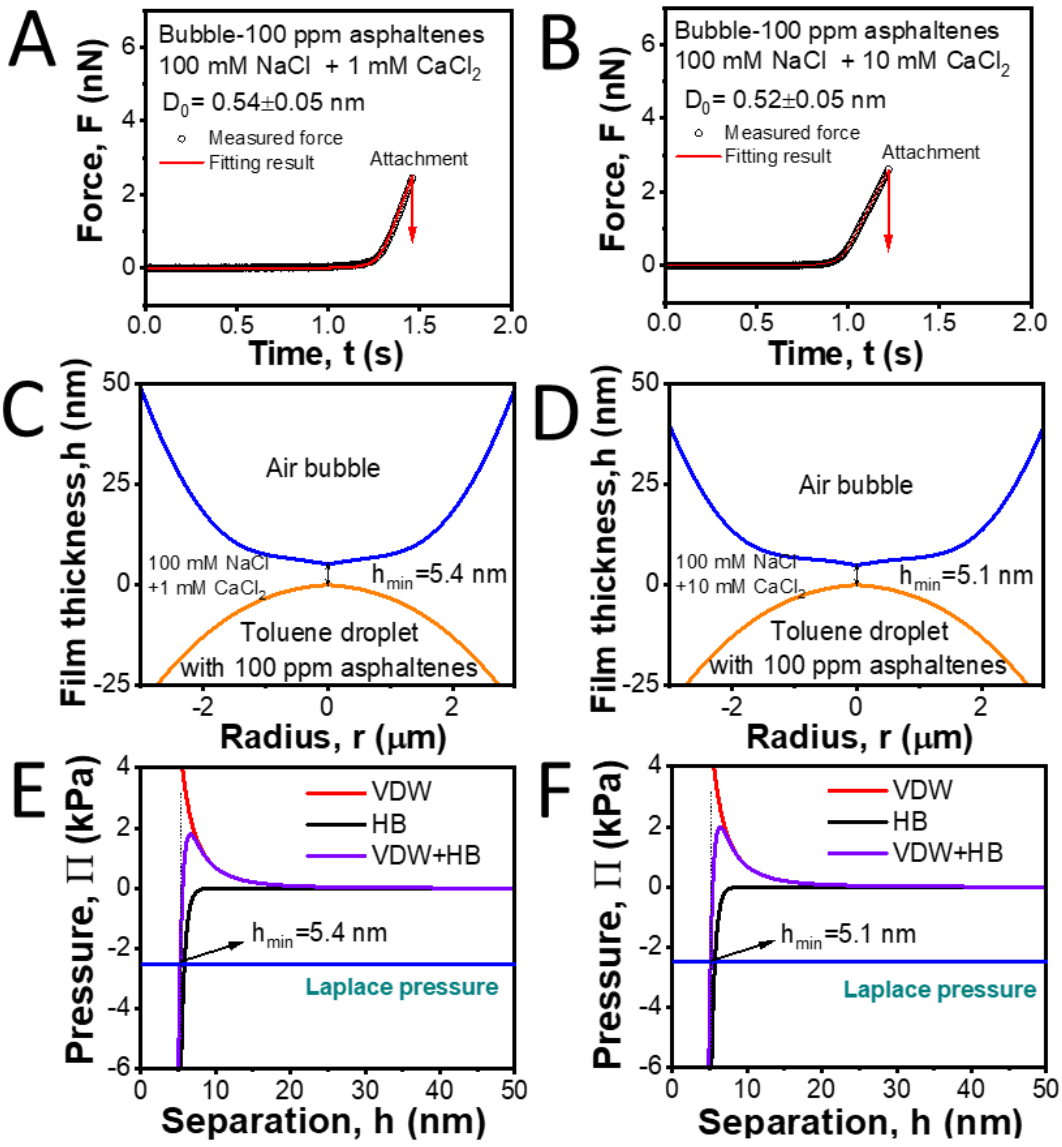

Figure 3.8. (A−B) Interaction force results for air bubbles interacting with asphaltenes-toluene droplet (100 ppm) in 100 mM NaCl with (A) 1 mM $CaCl_2$ (bubble radius r_1 = 50 μm, droplet radius r_2 = 49 μm), and (B) 10 mM $CaCl_2$ (bubble radius r_1 = 56 μm, droplet radius r_2 = 52 μm). The experimental results are presented as open symbols and the theoretical calculations are displayed as red curves using the model shown in Equations 1-3. (C−D) The local shapes of air bubbles approaching asphaltenes-toluene droplets at the minimum separation right before the two objects jumped into contact, where the blue

curves denote the bubble profiles and yellow curves present the droplet profiles in aqueous solutions of 100 mM NaCl with the addition of (C) 1 mM and (D) 10 mM $CaCl_2$. (E−F) Disjoining pressure results arising from VDW and HB interactions for the (E) 1 mM $CaCl_2$ and (F) 10 mM $CaCl_2$ cases, respectively.

3.3.3.4 The Effect of Surfactants

Interface-active species can influence the surface properties of the gas bubbles and liquid droplets, thus affecting their behaviors in industrial processes. In this research, two common interface-active chemicals, CTAC, and SDS, were applied as examples of surfactants to examine the influence surfactants have on the interactions of gas bubbles and liquid droplets. The forces for air bubbles interacting with droplets made of 100 ppm asphaltenes in toluene were examined in an aqueous solution of 100 mM NaCl and 1 mM $CaCl_2$ utilizing the bubble-probe atomic force microscope technique. Upon addition of the cationic surfactant CTAC and the anionic surfactant SDS, the jump-in and surface contact behaviors of bubbles and asphaltenes-toluene droplets were suppressed as shown in Figure 3.9A and 3.9B, with only repulsive forces detected. Without the interface-active CTAC and SDS, the hydrophobic attraction of bubbles with asphaltenes-toluene droplets overcame the VDW repulsion to cause the two surfaces to jump into contact (Figure 3.8A). In contrast, by introducing CTAC and SDS, the surfactant molecules were able to attach to the bubble/water and oil/water interfaces, resulting in increased steric repulsion that hindered the air bubbles from attaching oil droplets.

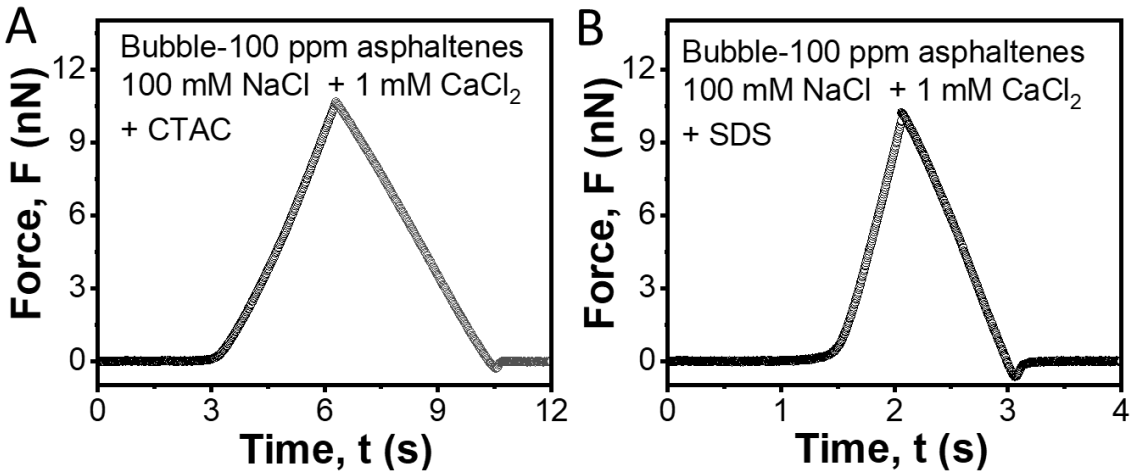

Figure 3.9. Surface force results for air bubbles interacting with asphaltenes-toluene (100 ppm) droplet in aqueous solutions of 100 mM NaCl and 1 mM $CaCl_2$ with the addition of surfactants: (A) 0.2 mM CTAC (bubble radius r_1 = 69 μm, droplet radius r_2 = 62 μm), and (B) 0.2 mM SDS (bubble radius r_1 = 65 μm, droplet radius r_2 = 63 μm). During the interaction, the driving speed of the cantilever was chosen as 1 μm/s, and the upper limit of the load was set at 10 nanonewtons.

3.4 Conclusions

This study has quantitatively characterized the surface forces of air bubbles with asphaltenes or asphaltene-oil droplets in aqueous media. The effects of concentrations of asphaltenes and salts, aqueous pH, divalent cations and the surfactants were examined, as illustrated in Figure S3. The results based on ITFDA force measurements show that high salinity condition enhances the adhesion between bubbles and asphaltenes because of the significantly suppressed EDL interaction, and their surface attachment was mainly driven by hydrophobic attraction by overcoming the repulsive hydrodynamic, VDW and EDL interactions. In AFM force measurements, the influence of hydrodynamic interaction was

negligible due to the low driving velocity of air bubbles applied, and the results also showed that the high salinity condition facilitated the attachment of air bubbles and asphaltene-oil droplets in aqueous media and further demonstrated the critical role of hydrophobic interaction in their surface attachment, agreeing with the ITFDA data. It is also demonstrated that higher asphaltenes concentration in the oil droplets strengthens its hydrophobic attraction with air bubbles, leading to their surface contact. Under low salinity condition (i.e., 1 mM NaCl), the EDL and VDW repulsion dominates the bubble-oil interactions, preventing the bubble-oil attachment. In contrast, when the salt concentration is high, the repulsive EDL forces are greatly reduced, and the hydrophobic attraction drove the bubbles to attach to asphaltene-toluene droplets. Increasing solution pH from pH 4 to pH 10 makes both the air bubbles and asphaltenes-toluene droplets more negatively charged, which enhances the EDL repulsion and weakens the HB attraction, with no surface attachment observed under low salinity condition. The addition of divalent cations such as Ca^{2+} weakens the hydrophobic attraction of bubbles with asphaltenes-toluene droplets, as the Ca^{2+} ions induce alterations of conformation and clustering of interfacial asphaltenes. The inclusion of surfactant species (such as CTAC and SDS) in the aqueous solutions inhibits adhesion of air bubbles with asphaltenes-toluene droplets, which is attributed to the strong steric interaction caused by the interfacial adsorption of surfactant molecules.

Different from many previous studies mainly via optical observations, [5, 19, 58] this work has employed direct force measurements to reveal the underlying mechanisms how air bubbles, asphaltenes and oil droplets with asphaltenes interact in complex aqueous media. The findings offer useful insights for modulating interactions among gas

bubbles, particles and droplets involved in interfacial processes relevant to various engineering operations, such as froth flotation, oil extraction, and oily water treatment. It should be noted that the water chemistry in many industrial operations is generally very complex, containing many oil/water/solid interface-active species, organic residues and solid particles, which are conducted under non-ambient conditions.[151-153] More effort is needed in future studies on uncovering how environmental conditions impact the interfacial interactions.[147, 164]

3.5 Supporting Infromation

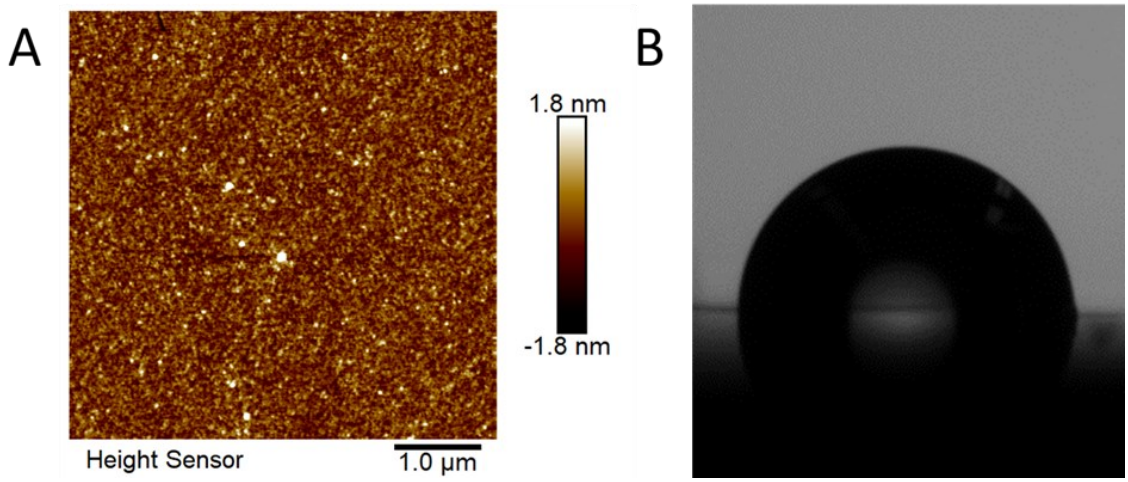

Figure S3.1. (A) Topographic AFM image of asphaltenes surface in air. The image size was 5 µm × 5 µm. (B) A picture of static water contact angle on asphaltenes surface.

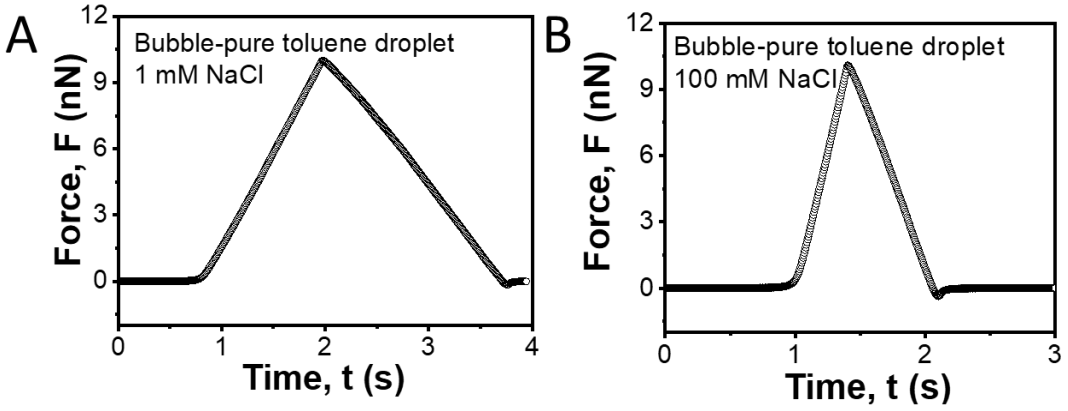

Figure S3.2. Interaction force curves measured between air bubbles and pure toluene droplet in aqueous solutions with (A) 1 mM NaCl (bubble radius r_1 = 51 μm, droplet radius r_2 = 53 μm), and (B) 100 mM NaCl (bubble radius r_1 = 50 μm, droplet radius r_2 = 51 μm).

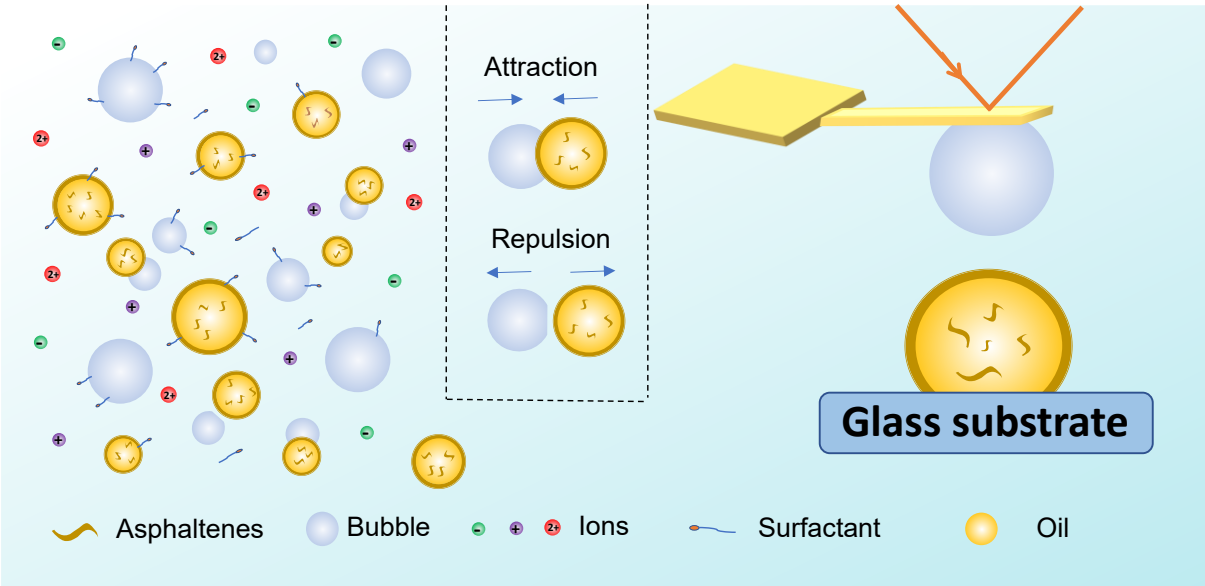

Figure S3.3. Illustration of the surface interactions of gas bubbles with oil droplets in a complex aqueous medium when interface-active oil components and surfactants are present.

Table S3.1. The dielectric constant ε and refractive index n of air, water[79], and toluene[171] at 20°C.

	Dielectric constant, ε	Refractive index, n
Air	1	1
Water	80	1.3333
toluene	2.38	1.4969

Table S3.2. Comparison of measured zeta potential values and theoretically fitted surface potential values of oil droplet.

Asphaltenes concn (ppm)	solution condition	measured zeta potential (mV)	Fitted surface potential (mV)	Air bubble zeta potential used for fitting (mV)[73, 168]
0	1 mM NaCl, pH=5.6	-33.0±4	-34.0±5	-25.0
10	1 mM NaCl, pH=5.6	-46.0±3	-45.0±5	-25.0
100	1 mM NaCl, pH=5.6	-63.0±3	-65.0±5	-25.0
100	1 mM NaCl, pH=4.0	-50.1±3	-53.0±5	-12.0
100	1 mM NaCl, pH=7.0	-65.2±3	-68.0±5	-33.0
100	1 mM NaCl, pH=10.0	-88.3±3	-90.0±5	-43.0

Video S1. The dynamic interaction video of an air bubble and asphaltenes surface in 1 mM NaCl, pH 5.6 solution during the ITFDA test.

Video S2. The dynamic interaction video of an air bubble and asphaltenes surface in 1 mM NaCl, pH 10 solution during the ITFDA test.

Video S3. The dynamic interaction video of an air bubble and asphaltenes surface in 100 mM NaCl, pH 5.6 solution during the ITFDA tests.

Video S4. The dynamic interaction video of an air bubble and asphaltenes surface in 100 mM NaCl, pH 10 solution during the ITFDA tests.

CHAPTER 4. Probing the Surface Forces between Air Bubbles and Bitumen via Direct Force Measurements: Effects of Aqueous Chemistry

4.1 Introduction

Air bubbles are ubiquitous in aqueous solutions and have some interesting characteristics including large surface area, low density, and hydrophobic nature,[172] which enable bubbles to selectively adsorb to specific materials (e.g., positively charged or hydrophobic species) in aqueous media. [72, 173-174] Therefore, bubbles have been used in a broad spectrum of engineering applications,[175-177] such as bitumen froth flotation,[101] surface cleaning,[178] wastewater treatment,[179] and drug/gene delivery.[100, 180] In these applications, the surface attachment between air bubbles and target materials plays a critical role in selective separation, which is mainly dominated by their interfacial interaction forces. In aqueous solutions, the interfacial interaction forces between two objects act on their surfaces via disjoining pressures, which arise from the molecular interactions across the thin water films between the objects. The disjoining pressure strongly depends on the separation distance between the objects and the composition of the surrounding aqueous media. The overall forces on the objects is determined by the balance between the disjoining pressures and the hydrodynamic pressure, significantly influencing the interaction behavior of these objects in aqueous solutions, such as their surface attachment or detachment.[181-183] Hence, characterizing and comprehending the interface interaction behaviors of bubbles and material surfaces in different fluid media during specific processes holds crucial practical and fundamental significance.

In oil sands industry, surface mining is employed to extract bitumen from oil sands deposits with the buried depth < 75 m. Warm water is used to extract bitumen from oil sands ores. In this technology, bitumen is liberated from oil sand ores and captured by air bubbles in aqueous media, forming bitumen froth. The surface forces of air bubbles and bitumen across the aqueous media have significant impacts on the recovery and quality of bitumen.[2, 184-185] Therefore, characterizing and understanding these surface forces is essential for modulating and optimizing the interfacial processes in bitumen extraction. Significant progress has been made in recent years towards understanding the air bubble-bitumen interaction behavior and the thin film drainage process under different water chemistry conditions.[29-30, 186-187] Many studies have been conducted to investigate the interaction forces of various surfaces in aqueous solutions, primarily using nanomechanical technologies such as the atomic force microscope (AFM) and surface forces apparatus (SFA).[27-28, 188-190] A combination of the bubble/drop probe AFM technique and theoretical computation has been employed for studying the interactions of deformable objects, such as gas bubbles and emulsion droplets, with other objects.[72, 74, 109] The interaction process and force measurement results are frequently analyzed using a theoretical model that relies on Reynolds lubrication theory and augmented Young-Laplace equation.[80-81] The surface forces and dynamic thin film drainage process during the interfacial interactions involving deformable bubbles/droplets can be experimentally monitored using the bubble/drop probe AFM technique, and then theoretically analyzed using the theoretical model. Surface forces resulting from van der Waals and electric double layer interactions, commonly referred to as Derjaguin-Landau-Vervey-Overbeek (DLVO) forces, hydrophobic and other interactions, among air/water/oil/solid interfaces

can be precisely quantified using the nanomechanical tools.[109, 163, 183] Previous studies show that interfacial processes, where bitumen and asphaltenes (the heaviest fraction of bitumen) are involved, are significantly influenced by surrounding fluid and environmental conditions, such as pH and salinity in aqueous solutions, organic solvent, and temperature, as illustrated in Figure 1A.[29-32] However, the impact of water chemistry factors on the interactions occurring between air bubbles and bitumen surfaces has not been well understood and quantified.

In this work, two different bitumen samples from northern Alberta have been systematically characterized using the Dean-Stark method, thermogravimetric analysis (TGA), elemental (CHNS) analysis, and Fourier transformation infrared spectroscopy (FTIR). The bitumen surface energy was characterized via contact angle measurements using three probe liquids, and AFM imaging was used to investigate the surface morphology of bitumen in different aqueous solutions (varying ionic concentration and solution pH). The bubble-bitumen surface forces in aqueous solutions of varying salinity, pH, type of ions and surfactants have been quantified. The force measurement results were subjected to analysis using a theoretical model founded on Reynolds lubrication theory and augmented Young-Laplace equation. The study has improved the basic understanding of how bubbles and bitumen interact on a nanoscale level in complex water-based solutions. The findings offer valuable insights for controlling the interactions of gas bubbles and liquid droplets in many relevant industrial processes.

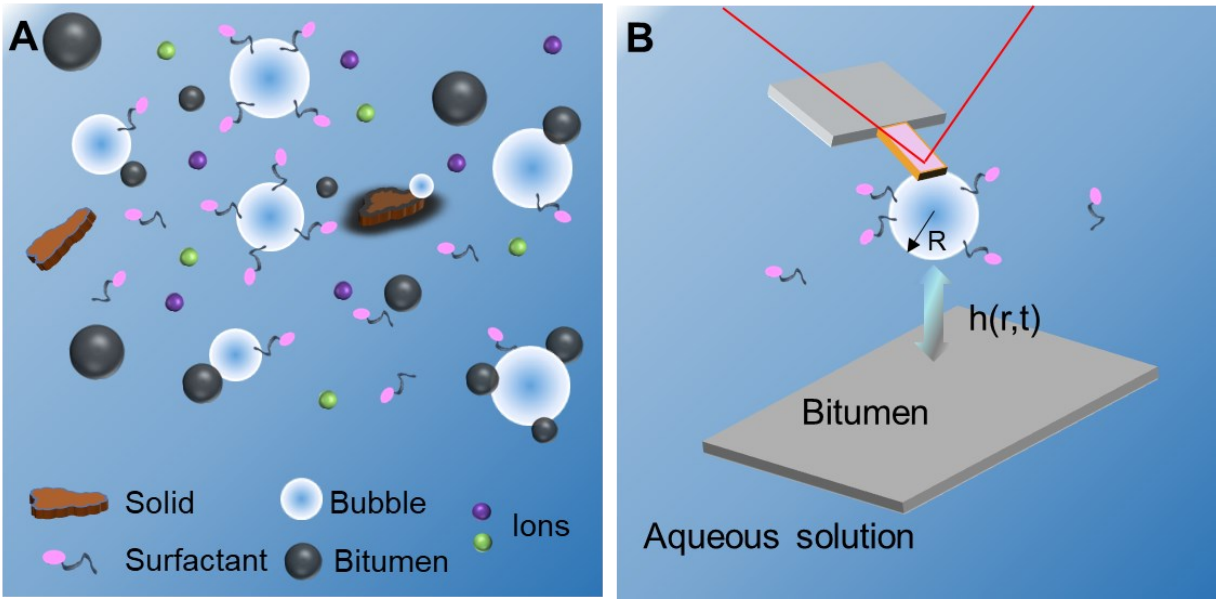

Figure 4.1. Schematics of (A) warm water-based bitumen extraction process in which the interactions among air bubbles, bitumen and solids in aqueous solutions of varying pH, salts and surfactants play a critical role, and (B) experimental setup of using the bubble probe AFM force to measure the interaction forces between air bubbles and bitumen surfaces in aqueous solutions.

4.2 Materials and Methods

4.2.1 Materials

Two types of Athabasca bitumen samples were collected from northern Alberta. Sodium chloride (NaCl, ACS reagent grade), calcium chloride ($CaCl_2$, ACS reagent grade), hydrochloric acid (HCl, ACS reagent grade), toluene (≥ 99.5%), and sodium hydroxide (NaOH, ACS reagent grade) were purchased from Fisher Scientific. Sodium dodecyl sulfate (SDS), diiodomethane, and diethylene glycol were provided by Sigma-Aldrich, Canada. All chemicals were used as received without further purification. All

aqueous solutions were prepared using Milli-Q water with a resistivity ⩾18.2 MΩ·cm.

4.2.2 Characterization of Bitumen

The composition and properties of two Athabasca bitumen samples used in this work were characterization using Dean-Stark method, thermogravimetric analysis (TGA), elemental (CHNS-O) analysis, and Fourier transform infrared spectroscopy - attenuated total reflectance (FTIR-ATR). The Dean-Stark apparatus was used to determine the water, bitumen, and solids contents in the oil sands sample. TGA analysis (TA instrument Q500) was conducted in the temperature range of 25-200°C with a heating rate of 5°C·min^{-1} under nitrogen gas flow (60.0 mL min^{-1}), and the weight loss of bitumen samples was recorded as a function of time (or temperature). Additionally, the primary elemental composition (i.e., C, H, N, S, O) of bitumen samples was measured using a CHNS-O Flash2000 Elemental Analyzer (Thermo Fisher Scientific).

4.2.3 Preparation and Characterization of Bitumen Surfaces

To study the surface forces between bitumen and air bubbles in aqueous solutions, bitumen-coated surfaces were prepared using spin coating method using the two bitumen samples. Briefly, bitumen sample was dissolved in toluene to obtain a concentration of 3 mg/mL, then the mixture was centrifuged at 7000 rpm for 30 minutes to remove possible solids. The bitumen in toluene solution was filtered with a PTFE membrane (pore size of ~0.2 μm) and used to prepare bitumen thin films coated on silicon wafer substrates via spin coating method. The as-prepared bitumen surfaces were kept under vacuum overnight (>12 hours) to removal residual toluene prior to further tests.

The zeta potential of bitumen surface in aqueous solution was estimated by measuring the zeta potential of bitumen-in-toluene droplets in aqueous solutions. Briefly,

the bitumen-in-toluene solution after filtration was dispersed in NaCl aqueous solution under sonication to obtain an oil-in-water emulsion, and the emulsion was then used for zeta potential measurement using a Zetasizer Nano ZSP device (Malvern Instruments, UK). The surface energies of as-prepared bitumen surfaces were determined using three-probe-liquid method [191-192]. Diiodomethane, water, and ethylene glycol were used as the three probing liquids, and their contact angles on the bitumen surface were measured by a goniometer using sessile drop technique. The surface energy of bitumen was calculated based on the relationship between surface energies and contact angles of probe liquids on the bitumen surface, and the detailed calculation procedure was provided in the Supporting Information (SI). The surface morphology and roughness of bitumen surfaces in air and in aqueous solutions were characterized by AFM imaging using the tapping mode (MFP-3D AFM, Asylum Research, Santa Barbara, CA, USA). The surface chemical properties of bitumen surfaces were characterized by Fourier transform infrared (FTIR) spectroscopy.

4.2.4 AFM Force Measurements

The interaction forces between air bubbles and bitumen surfaces in aqueous solutions were directly measured using the bubble probe AFM technique (see Figure 4.1B). In a typical force measurement using the bubble probe AFM, an air bubble with a diameter of ~50 μm was anchored on the free end of the customized tipless rectangular silicon AFM probe (400×70×2 μm^3). There was a circular gold patch (radius of ~32.5 μm) at the free end of tipless AFM probe, which was hydrophobized using 1-decanethiol for stable bubble attachment in aqueous solutions.[72-74] The tipless AFM probe acted as a force spring, calibrated as 0.3-0.4 N/m using the method proposed by Hutter and

Bechhoefer.[111] In force measurements, the bubble probe was driven to approach the desired substrate surface till reaching a specific load, and then it was driven towards and retracted away from the surface. In this work, bubble probe was driven at 1 μm/s so the hydrodynamic effect played a negligible role. During the force measurements, the deflection of AFM cantilevers, induced by bubble-bitumen interaction forces, was monitored in real time by an optical lever system, and the interaction forces was obtained using Hooke's law and captured through piezo displacement (or time).

4.2.5 Theoretical Model.

The interaction forces obtained from bubble probe AFM measurements were analyzed using a theoretical model based on Stokes-Reynolds-Young-Laplace (SRYL) model with the inclusion of disjoining pressure, which could provide useful information about the deformation of air bubbles and separation distance between the bubbles and bitumen surfaces during their surface interactions and force measurements.[112, 114-116, 193] The dynamic drainage of confined thin water film between air bubbles and bitumen surfaces can be analyzed using Reynolds lubrication theory. Assuming that both bubble/water and bitumen/water interfaces have non-slip boundary conditions, the dynamic drainage process of confined water layer is described by Equation 4.1 [194-195],

$$\frac{\partial h(r,t)}{\partial t} = \frac{1}{12\mu r}\frac{\partial}{\partial r}\left(rh^3 \frac{\partial p(r,t)}{\partial r} \right) \tag{4.1}$$

where $h(r,t)$ is the film thickness, r is the radial distance to the axis of the bubble, μ denotes dynamic viscosity of water, $p(r,t)$ represents the additional hydrodynamic pressure inside the thin water film compared to the bulk aqueous medium.

Air bubbles can be readily deformed during the interactions with flat substrates (i.e.,

bitumen coated on silicon wafer) in the force measurements due to external pressures such as hydrodynamic pressure and disjoining pressure. This process is generally given by the augmented Young-Laplace equation,[194-195]] as shown in Equation 4.2,

$$\frac{\gamma}{r}\frac{\partial}{\partial r}\left(r\frac{\partial h(r,t)}{\partial r}\right)=\frac{2\gamma}{R}-p(r,t)-\Pi\left[h(r,t)\right] \tag{4.2}$$

where γ is the surface tension of aqueous solution, R denotes the radius of the bubble probe, $\prod$ denotes the disjoining pressure caused by air bubble-bitumen surface forces.[47, 106, 119-122] Several surface interactions, such as hydrophobic interaction, van der Waals (VDW) interaction, and the electric double layer (EDL) interaction contribute to the overall disjoining pressure, which are expressed as Equations 4.3 to 4.5, respectively,[33, 123, 196] [74, 79]

$$\Pi_{HB}=-\frac{C_0}{2\pi D_0}\exp\left(-\frac{h(r,t)}{D_0}\right) \tag{4.3}$$

$$\prod_{VDW}=-\frac{A_H}{6\pi h^3(r,t)} \tag{4.4}$$

$$\Pi_{EDL}=\frac{2\varepsilon_0\varepsilon\kappa^2\left[\left(e^{+\kappa h}+e^{-\kappa h}\right)\varphi_1\varphi_2-\left(\varphi_1^2+\varphi_2^2\right)\right]}{\left(e^{+\kappa h}-e^{-\kappa h}\right)^2} \tag{4.5}$$

where Π_{HB}, Π_{VDW}, and Π_{EDL} are the disjoining pressures induced by hydrophobic, VDW, and EDL interactions, respectively, C_0 is a constant value related to the static water contact angle θ_w on bitumen surface and $C=2\pi\gamma\left(1-\cos\theta_w\right)$, D_0 is a characteristic decay length of hydrophobic interaction, A_{H} denotes the Hamaker constant between air bubble and bitumen surface across the aqueous solution, κ is the reciprocal of

Debye length, ε_0 is the vacuum permittivity, ε is the dielectric constant of the aqueous solution, φ_1 and φ_2 are the surface potentials of air bubble and bitumen surface in the aqueous solution, respectively. The total interaction forces of an air bubble and bitumen surface are determined by integrating the overall external pressure (i.e., hydrodynamic pressure and disjoining pressure) along the air bubble surface according to the Derjaguin approximation, as shown in Equation 4.6. [83, 124, 193]

$$F(t) = 2\pi \int_0^{\infty} \left[p\left(h(r,t)\right) + \prod\left(h(r,t)\right) \right] \cdot r dr \tag{4.6}$$

4.3 Results and Discussion

4.3.1 Properties of Athabasca Bitumen Samples

The water, solid, and bitumen contents of the two Athabasca bitumen samples from northern Alberta were determined using the Dean-Stark method and the results are summarized in Table 4.1. Although the two Athabasca bitumen samples have the same solids content (~0.1 wt%), the bitumen sample 1 has a much higher water content (18.6 wt%) than the bitumen sample 2. The bitumen contents of the two bitumen samples were determined to be 80.3 wt% and 96.8 wt%, respectively. The relatively high-water content in bitumen sample 1 was also confirmed by TGA and elemental analysis results. As shown in Figure 4.2, when the temperature was increased to 100°C, the bitumen sample 1 experienced an obvious mass loss (~ 20 wt%) that could be attributed to the evaporation of water or volatile components, while bitumen sample 2 only showed a slight mass loss. Table 4.2 displays the elemental analysis results of the two bitumen samples. Notably, the bitumen sample 1 has more hydrogen and oxygen yet less carbon elements as compared to the bitumen sample 2, which could be ascribed to the high-water content and low

bitumen content of bitumen sample 1.

Table 4.1. Composition of the two Athabasca bitumen samples

Composition	Bitumen sample 1	Bitumen sample 2
Solids (wt%)	0.1	0.1
Water (wt%)	18.6	0.6
Bitumen (wt%)	80.3	96.8

Table 4.2. Elemental analysis results of the two Athabasca bitumen samples.

Elemental composition (wt%)	Bitumen sample 1	Bitumen sample 2
Nitrogen	0.36±0.01	0.44±0.03
Carbon	69.26±0.47	83.26±0.11
Hydrogen	10.83±0.11	10.72±0.07
Sulfur	3.65±0.07	4.70±0.09
Oxygen	12.70±0.78	0.81±0.05

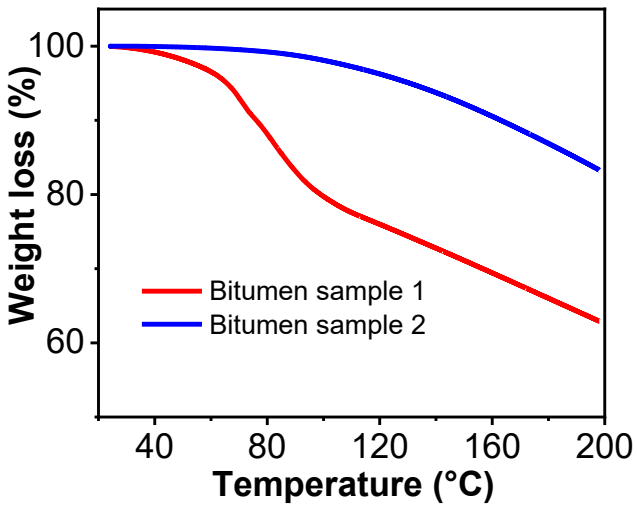

Figure 4.2. TGA results of the two Athabasca bitumen samples.

4.3.2 Characterization of Bitumen Surfaces

The surface energies of the two bitumen samples were characterized using the three-probe-liquid method (see Table S4.1 in the Supporting Information). The experimental details of the three-probe-liquid method are shown in the Supporting Information. Van Oss et al. reported that the surface energy (γ) has two primary components: Lifshitz-vdW component (γ^{LW}) and Lewis acid-base component (γ^{AB}, including electron acceptor γ^{+} and electron donor γ^{-}).[191-192] The surface energy components of the three probing liquids (i.e., diiodomethane, water, and diethylene Glycol) are shown in Table S4.1. Table S4.1 shows a larger contact angle of the polar probe liquid (e.g., water) on bitumen surfaces compared to that of the nonpolar probe liquid (e.g., diiodomethane), which indicates the hydrophobic nature of bitumen surfaces. The surface energies of the two types of bitumen surfaces (γ_1 and γ_2) were determined to be 44.42 mJ/m^2 and 45.23 mJ/m^2, respectively.

Notably, the free energies of Lifshitz-vdW (ΔG^{LW}_{A-W-B}) and Lewis acid-base interactions (ΔG^{AB}_{A-W-B}) between the air bubble and bitumen surfaces across aqueous solutions can be calculated based on the results of three-probe-liquid tests by using Equations 4.7 and 4.8 and the data in Table S4.1, [191-192]

$$\Delta G^{LW}_{A-W-B} = 2\sqrt{\gamma^{LW}_{W}}\left(\sqrt{\gamma^{LW}_{B}} - \sqrt{\gamma^{LW}_{W}}\right) \tag{4.7}$$

$$\Delta G^{AB}_{A-W-B} = 2\left[\sqrt{\gamma^{+}_{W}}\left(\sqrt{\gamma^{-}_{B}} - \sqrt{\gamma^{-}_{W}}\right) + \sqrt{\gamma^{-}_{W}}\left(\sqrt{\gamma^{+}_{B}} - \sqrt{\gamma^{+}_{W}}\right)\right] \tag{4.8}$$

where the subscripts *A*, *B*, or W stand for air, bitumen, and water, respectively. The positive value of ΔG^{LW}_{A-W-B} indicates that the VDW interaction is repulsive, which prevents

the air bubbles from attaching to the bitumen surface in water. The negative value of ΔG_{A-W-B}^{LW} denotes an attractive interaction, such as hydrophobic interaction, that induces the attachment of air and bitumen in water. The Lifshitz-vdW ΔG_{A-W-B}^{LW} values for the surfaces of bitumen 1 and 2 were calculated to be 17.4 and 18.95 mJ/m^2, respectively, suggesting that the repulsive vdW interactions between air bubbles and the two bitumen surfaces inhibit their attachment. However, the Lewis acid-base interactions (ΔG_{A-W-B}^{AB}) between air bubbles and surfaces of bitumen 1 and 2 were determined to be -82.94 and -92.9 mJ/m^2, respectively. The calculated negative Lewis acid-base interactions indicate the presence of strong attraction (e.g., hydrophobic interaction) between air bubbles and bitumen surfaces in aqueous solutions, which could contribute to their surface attachment.

Figure 4.3 illustrates the FTIR spectrum of the two bitumen surfaces, which show similar profiles. The absorption peak at 1705-1725 cm^{-1} can be attributed to the stretching vibration of C=O groups (such as ketone structure groups), and the peak at 1380-1465 cm^{-1} belongs to the stretching vibration of C-H bonds (e.g., -CH_3, -CH_2).[197] The absorption peak between 1000 cm^{-1} and 1100 cm^{-1} mainly corresponds to the S=O stretching vibration (and also possibly C-N stretching vibration) due to the relatively high sulfur content and low nitrogen content of the two types of bitumen (Table 4.2). The 900-995 cm^{-1} peak most likely corresponds to C-H bending. The FTIR spectra further confirms the presence of hetero atoms (e.g., N, S) and polar functional groups in both bitumen samples.

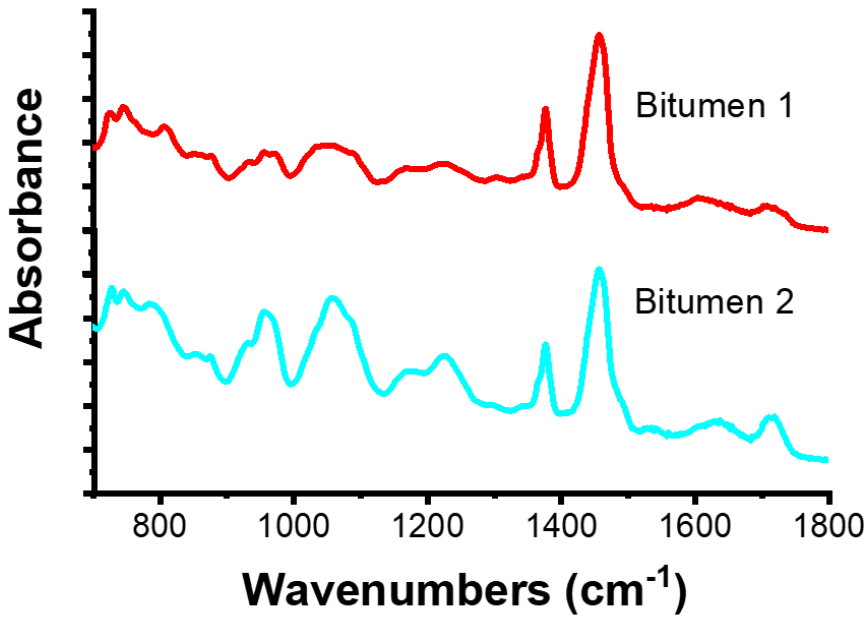

Figure 4.3. FTIR spectra of the two bitumen surfaces.

The wettability and morphology of bitumen surfaces were characterized using goniometer and AFM imaging, respectively. Figure 4.4 illustrates the water contact angle and AFM images of the two bitumen surfaces in air. The average static water contact angles of bitumen 1 and bitumen 2 surfaces were determined as 96.8°±0.6° and 100.6° ±0.8°, respectively. The root-mean-square (RMS) roughness of two bitumen surfaces were found to be ~0.31 nm and ~0.27 nm, respectively. These results indicate that the two bitumen surfaces prepared via spin-coating were hydrophobic and very smooth.

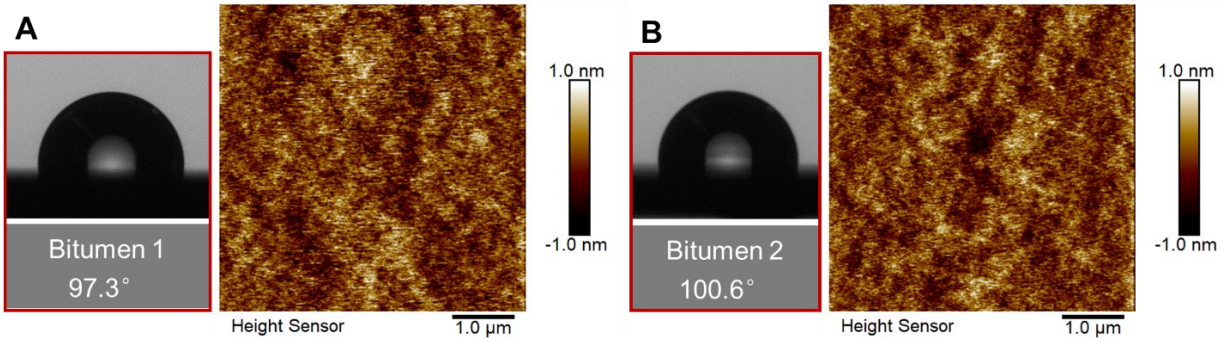

Figure 4.4. Image of static water contact angle and the AFM images of (A) Bitumen 1 surface and (B) Bitumen 2 surface. The scan size of the images was 5 μm × 5 μm.

The morphologies of two bitumen surfaces under different water chemistry conditions (i.e., ionic strength, pH) haves been investigated. As shown in Figure 4.5, the bitumen surfaces become much rougher in aqueous solution compared to those in air and show some features that are consistent with other types of bitumen surfaces reported previously.[186, 198] Both types of bitumen surfaces were submerged in aqueous solutions for at least 60 minutes prior to imaging, while the morphology did not show obvious change with further increase in the submerging time.

In 1 mM NaCl, when the aqueous pH was raised from pH 5.8 to 9, bitumen 1 surface showed a slightly increased RMS roughness (i.e., increasing from 0.51 to 0.56 nm, see Figure 4.5A and 4.5B); and for bitumen 2 surface, the roughness increased slightly from 0.62 to 0.68 nm (Figure 4.5E and 4.5F). Bitumen generally contains many natural interface-active species with polar functional groups (e.g., -COOH) which can deprotonate under alkaline environment.[20,50] So, the increased roughness of the bitumen/water interface as the pH rises, possibly ascribed to the dissociation of protons from polar functional groups and change of molecule conformations. In 100 mM NaCl solution, this roughening phenomenon of bitumen surfaces with increasing solution pH is more pronounced (see Figure 4.5C, 4.5D, 4.5G, and 4.5H, which show RMS roughness 0.92 nm, 2.18 nm, 1.05 nm, 1.54 nm, respectively). The primary reason for the lager surface roughness under high-salinity conditions is the decrease in electrostatic repulsion between the polar moieties present on the molecules or aggregates of bitumen. The slightly different roughness of the two bitumen surfaces could be linked to the different

amount of various polar groups contained in the two bitumen samples.

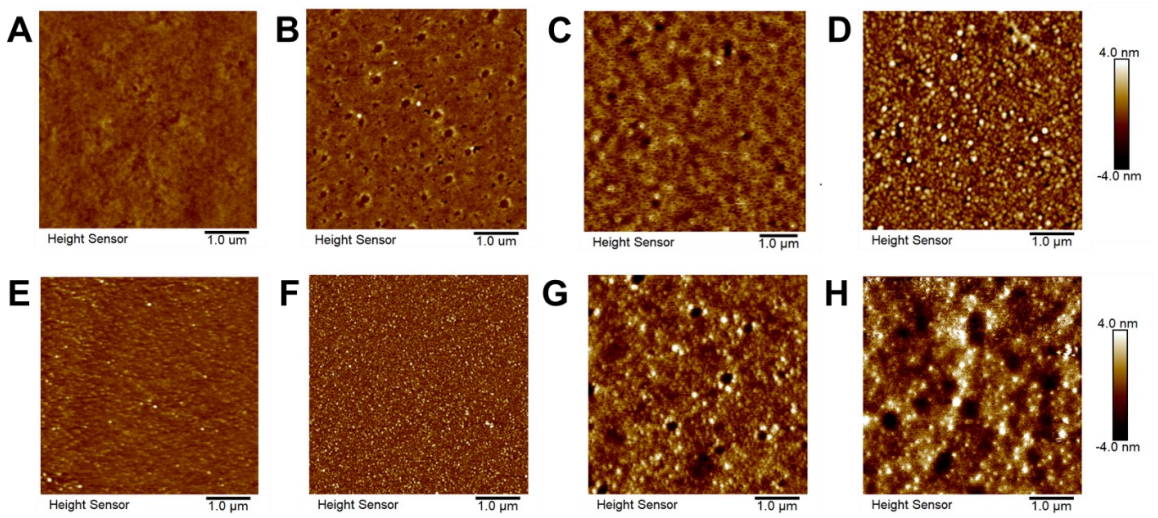

Figure 4.5. AFM images of the bitumen 1 surface in (A) 1 mM NaCl at pH 5., (B) 1 mM NaCl at pH 9, (C) 100 mM NaCl at pH 5.8, and (D) 100 mM NaCl at pH 9; and AFM images of the bitumen 2 surface in (E) 1 mM NaCl at pH 5.8, (F) 1 mM NaCl at pH 9, (G) 100 mM NaCl at pH 5.8, and (H) 100 mM NaCl at pH 9.

4.3.3 Bubble Probe AFM Force Measurement

4.3.3.1 Effects of pH

The surface forces of air bubbles and the two bitumen surfaces in different water solutions (i.e., varying pH, ionic strength, ion types) have been characterized using a bubble probe AFM technology. In this study, the pH of the aqueous solutions was fixed at pH 5.8 or pH 9, and the salinity was fixed at 1 mM or 100 mM NaCl to investigate the influence of pH and salt concentration. It is noted that pH 5.8 was the natural pH of the NaCl solutions and pH 9 is close to pH conditions (generally pH 8 to 10) used in bitumen flotation in oil sands production. Figure 4.6 illustrates the surface force profiles between

air bubbles and two bitumen surfaces in 100 mM NaCl solution at pH 5.8. For both bitumen samples, abrupt "jump-in" behaviors were observed during bubble approaching process after overcoming the repulsion force of ~7.5 nN (Figure 4.6A) and ~7.1 nN (Figure 4.6D), respectively, which indicate the attachment of air bubbles to the bitumen surfaces. For this air-water-bitumen system, the Hamaker constant (A_H) was calculated to be -1.8×10^{-20} J,[79] which indicates the vdW interaction was repulsive between air bubbles and bitumen surfaces across water and agrees with the results on free energies of Lifshitz-vdW (ΔG^{LW}_{A-W-B}) in section 4.3.2. Considering that both air bubbles and bitumen surfaces are negatively charged in the aqueous solution, their EDL interaction is also repulsive, though the EDL interaction is significantly suppressed under high-salinity conditions (Debye length of ~0.96 nm in 100 mM NaCl). Since the surfaces of both air bubbles and bitumen are hydrophobic, it is reasonable to infer that their attractive hydrophobic interaction significantly influences the bubble-bitumen attachment behavior. The bubble-bitumen interaction force curves were fitted using the SRYL model, and the characteristic length of hydrophobic interaction decay D_0 of bitumen 1 and bitumen 2 was determined to be about 0.97 nm and 1.0 nm, respectively. The evolution of bubble profiles during force measurements are illustrated in Figure 4.6B and 4.6E for bitumen 1 and bitumen 2, respectively. The minimum separation distances between the bubbles and bitumen surfaces before 'jump-in' occurrence were determined to be 9.6 nm and 10.0 nm for bitumen 1 and 2, respectively. The related profiles of disjoining pressures for the two cases are shown in Figure 4.6C and 4.6F. Due to the diminished EDL interaction and the repulsive van der Waals interaction in 100 mM NaCl, the primary factor governing the overall interaction is the attractive hydrophobic interaction, which triggers the attachment

of the air bubbles onto the bitumen surfaces. Although the two bitumen surfaces have slightly different surface chemistry, the strength and range of bubble-bitumen hydrophobic interactions in these two cases are almost the same.

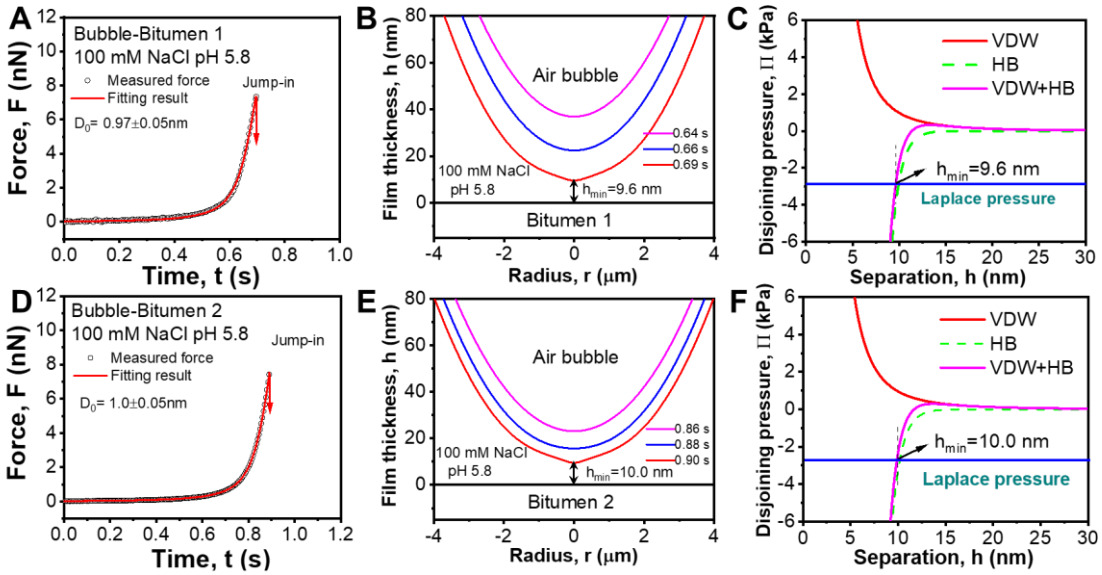

Figure 4.6. Representative force profiles, air bubble profiles and disjoining pressure results of air bubbles interacting with (A-C) Bitumen 1 surface (bubble radius R_b = 50 μm) and (D-E) Bitumen 2 surface (bubble radius R_b = 52 μm) in 100 mM NaCl solution at pH 5.8. Black open symbols represent experiment data, and red solid curves illustrate theoretical calculations based on the SRYL model. (B) and (E) The evolution of bubble profiles during force measurement with the red curve showing the bubble shape at the minimum separation distance immediately preceding "jump in" behavior. (C) and (F) The related disjoining pressure results induced by VDW and HB interactions.

The interaction forces between air bubbles and the two bitumen samples have been quantified under high salinity and high pH conditions, and the results are shown in Figure

4.7. Figure 4.7A and 4.7D illustrate the typical force profile of air bubbles and the surfaces of bitumen 1 and bitumen 2 in a solution containing 100 mM NaCl at pH 9.0, respectively. As the aqueous solution pH increased from pH 5.8 to 9, the jump-in behavior could still be observed and the interactions between bubbles and bitumen surfaces were dominated by the attractive hydrophobic interaction. According to the theoretical analysis, the hydrophobic interaction decay length D_0 for the bitumen 1 and bitumen 2 surfaces were determined to be 0.88 nm and 0.89 nm, respectively, which were less than those under pH 5.8 condition. The results indicate that the bubble-bitumen hydrophobic interaction was weakened with increasing aqueous solution pH. The critical separation distances before the jump-in behavior were determined to be 8.6 nm for bitumen 1 and 8.8 nm for bitumen 2 (Figure 4.7B and 4.7E), which were smaller than those under pH 5.8 condition. The decreased critical separation distance also indicates the weakened hydrophobic attraction in alkaline solution. These results also agree with previous studies which showed that the water contact angle of bitumen surface decreases when the aqueous solution pH increases.[199] It is noteworthy that the hydrophobic interaction results from the entropic effect caused by the disruption of the hydrogen bonding network of water molecules that are in proximity to the hydrophobic surfaces or moieties.[19, 79, 200] With increasing solution pH, some polar groups (e.g., carboxyl and phenolic groups) in bitumen (particularly the interface-active fractions such as asphaltenes) are deprotonated, which changes the wettability of bitumen surfaces and consequently affects the strength and range of hydrophobic interaction.[29, 47, 85, 201] The calculated disjoining pressure profiles due to VDW and HB interactions between air bubbles and bitumen surfaces in 100 mM NaCl at pH 9 are illustrated in Figure 4.7C and

Figure 4.7F for bitumen 1 and bitumen 2, respectively. The hydrophobic attraction overcame the VDW repulsion at a critical separation distance (h_{min}), inducing the bubbles to come into contact with the bitumen surfaces.

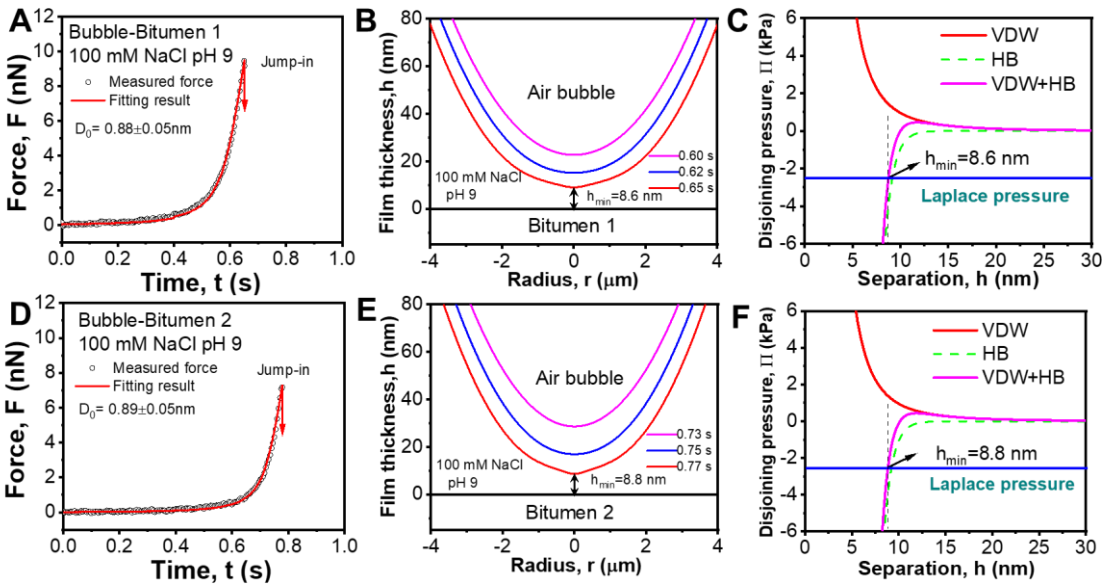

Figure 4.7. Representative force profiles, air bubble profiles and disjoining pressure results of air bubbles interacting with (A-C) bitumen 1 surface (bubble radius R_b = 56 μm) and (D-F) bitumen 2 surface (radius of bubble R_b = 51 μm) in 100 mM NaCl solution at pH 9. Black open symbols represent experiment measured results, and red solid lines illustrate theoretical fitting results based on the SRYL model. (B) and (E) The evolution of air bubble profiles in the force measurements, with the red curves show the bubble profile at minimum separation. (C) and (F) calculated disjoining pressure results arising from VDW and HB interactions.

4.3.3.2 Effect of Ion Strength

The interaction forces between air bubbles and the two bitumen samples have been also quantified under low salt concentration (i.e., 1 mM NaCl) to investigate the effect of ionic strength, and the results for two pH cases (i.e., pH 5.8, pH 9.0) are shown in Figure 4.7 and Figure 4.8. Figure 4.8A and 4.8D illustrate the representative surface force profiles between air bubbles and the surfaces of bitumen 1 and bitumen 2 in 1 mM NaCl at pH 5.8, respectively. Interestingly, there was no jump-in phenomenon detected, which could be ascribed to the strong and long-range EDL repulsion for bubble-bitumen under the low salinity condition. By using the SRYL model, the surface potentials of bitumen 1 and bitumen 2 in 1 mM NaCl at pH 5.8 were determined to be -45.0 ± 5.0 mV and -59.0 ± 5.0 mV, respectively, which were close to the measured zeta potential values of the two bitumen samples (Table 4.3). Figure 4.8B and 4.8E illustrate the profiles of air bubbles that were interacting with bitumen 1 and bitumen 2 surfaces, respectively, under the maximum load (30 nN). The minimal separation for the two cases were determined to be 19.6 and 23.6 nm for the bitumen 1 and bitumen 2 cases, respectively. Figure 4.8C and 4.8F illustrate the disjoining pressure profiles that arise from the various surface forces (i.e., VDW, hydrophobic, and EDL interactions) involved in the two cases.

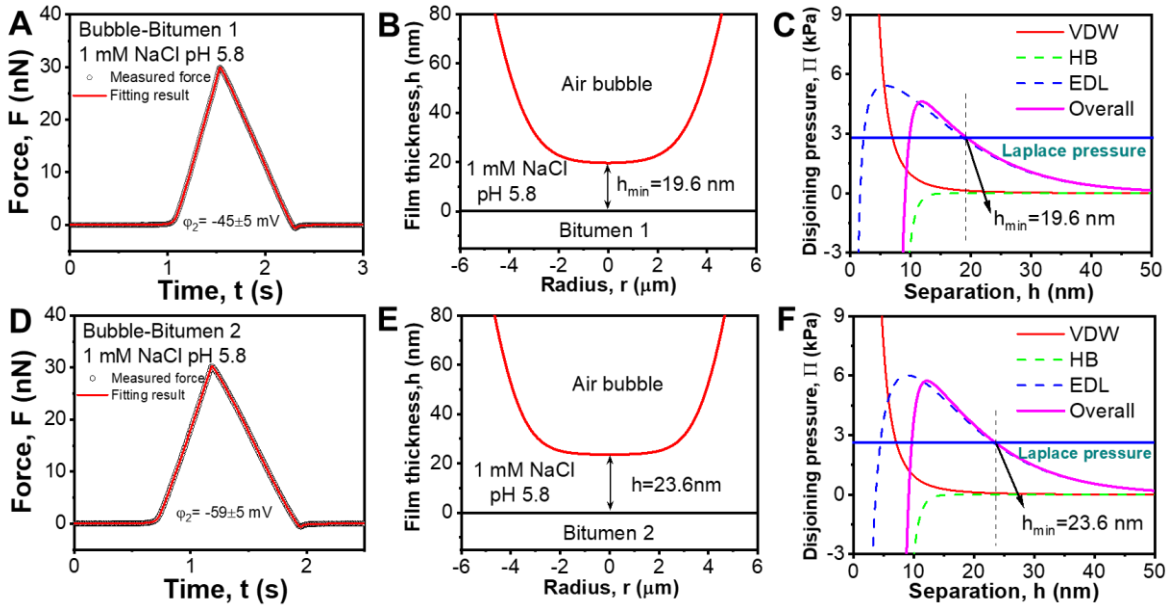

Figure 4.8. Representative force curves, air bubble profiles and disjoining pressure results of air bubbles interacting with (A-C) bitumen 1 surface (bubble radius R_b = 51 μm) and (D-F) bitumen 2 surface (bubble radius R_b = 55 μm) in 1 mM NaCl solution at pH 5.8. Black open symbols represent experiment results and red solid curves illustrate theoretical calculations based on the SRYL model. (B) and (E) The bubble profiles in the force measurement under the maximum force load applied (i.e., 30 nN). (C) and (F) Disjoining pressure results arise from various surface interactions (i.e., VDW, EDL and HB interactions).

Table 4.3. Comparison and summary of measured zeta potential results and theoretically determined surface potential values of bitumen surfaces and air bubbles.

		1 mM NaCl pH 5.8	1 mM NaCl pH 9
Bitumen 1	Measured zeta potential (mV)	-42.0±0.2	-61.9±0.3
	Fitted surface potential (mV)	-45.0±5.0	-65.0±5.0
Bitumen 2	Measured zeta potential (mV)	-57.4±0.4	-69.2±0.3
	Fitted surface potential (mV)	-59.0±5.0	-72.0±5.0
Air bubble[168]	Zeta potential =(mV)	-35.0	-50.0

In 1mM NaCl alkaline aqueous solution (pH 9.0), the jump-in behavior of air bubbles was not observed as shown in Figure 4.9, and fitted surface potentials of the bitumen 1 and bitumen 2 surfaces were determined to be -65.0 ± 5.0 mV and -72.0 ± 5.0 mV, respectively, by using the SRYL model. The minimal separation for the two cases were determined to be 27.8 and 29.5 nm for the bitumen 1 and bitumen 2 cases, respectively (Figure 4.9B and 4.9E). The more negative surface potentials of bitumen and bubble surfaces strengthened the EDL repulsion in the bubble-water-bitumen system, which resulted in the increased minimum separation distance between the air bubbles and bitumen surfaces under the maximum load (see Figure 4.9B and 4.9E). Such results are most likely caused by the following factors: 1) increasing adsorption amount of hydroxide ion on the air bubbles and bitumen surfaces in alkaline solution, and 2) dissociation of protons of polar groups (e.g., carboxyl, phenolic groups) of surface-active species in bitumen. As shown in Figure 4.9B and 4.9E, the central region of the air bubble surfaces was flattened under the applied load force, which is due to the balance between the overall repulsive disjoining pressure and the Laplace pressure. The profiles of calculated disjoining pressures between air bubbles and the surfaces of bitumen 1 and bitumen 2 in 1 mM NaCl solution are illustrated in Figure 4.9C and 4.9F, respectively. The results show that the repulsive EDL interactions play a key role in the bubble-water-bitumen system under the low salinity condition and dominate the behavior of air bubbles during the force measurement process.

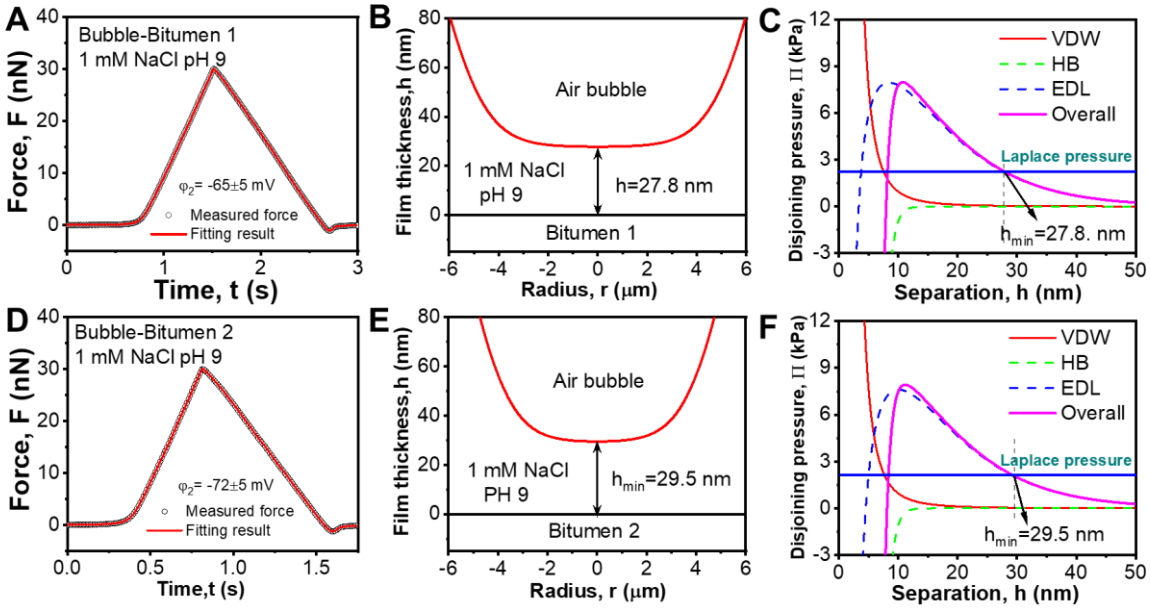

Figure 4.9. Representative force profiles, air bubble profiles and disjoining pressure results of air bubbles interacting with (A-C) Bitumen 1 surface (bubble radius R_b = 63 μm) and (D-F) Bitumen 2 surface (bubble radius R_b = 67 μm) in 1 mM NaCl solution at pH 9. Black open symbols represent experiment results and red solid curves illustrate theoretical calculations based on the SRYL model. (B) and (E) The bubble profiles during the approaching process under the maximum force load of 30 nN. (C) and (F) Disjoining pressure profiles induced by various surface interactions (i.e., VDW, EDL and HB interactions).

4.3.3.3 Effect of Calcium Ion

Calcium ion is one of the most common cations in produced water in oil sands production and other engineering processes, which has significant impacts on the bitumen extraction process. Therefore, in this work, the effect of Ca^{2+} ion on the interactions

between air bubbles and bitumen surfaces has been investigated. The AFM imaging results in Figure 4.10A and 4.10B illustrate the surface morphologies of the bitumen 1 and bitumen 2 in the aqueous solution containing 100 mM NaCl and 1 mM $CaCl_2$ at pH 5.8. With the addition of 1 mM Ca^{2+}, the morphologies of bitumen 1 and bitumen 2 surfaces became much rougher with many large aggregates, and the RMS roughness was determined to be 5.3 nm and 6.5 nm, respectively. It is most likely that Ca^{2+} ions have a strong interaction with certain polar groups (e.g., -COOH) of surface-active species in bitumen which causes the formation of large aggregates on the bitumen surfaces.

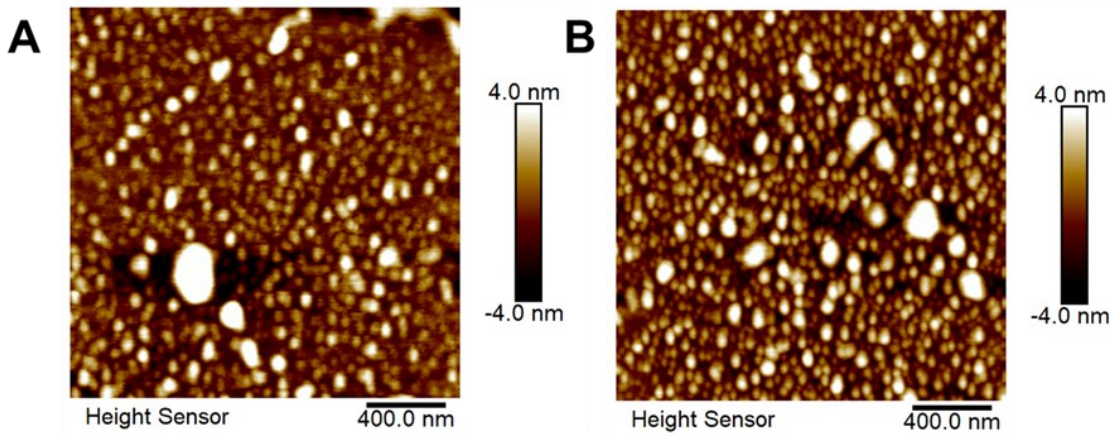

Figure 4.10. AFM images of (A) Bitumen 1 surface and (B) Bitumen 2 surface in 100 mM NaCl with 1 mM $CaCl_2$ solution at pH 5.8.

The effect of calcium ions on the interaction forces of air bubbles and the two types of bitumen has been quantified, and the results are shown in Figure 4.11. The representative force profiles between air bubble and the surfaces of bitumen 1 and bitumen 2 in the aqueous solution containing 100 mM NaCl and 1 mM $CaCl_2$ at pH 5.8 were shown in Figure 4.11A and 4.11D, respectively. A “jump-in” behavior was observed

during approaching process for both bitumen 1 and bitumen 2 surfaces, and the maximum repulsive forces before the "jump in" behavior were measured to be ~4.3 nN and ~4.1 nN, respectively. The decay length of hydrophobic interactions was determined to be ~1.28 nm and ~1.38 nm for bitumen 1 and bitumen 2 surfaces, respectively, by using the SRYL model. The critical central separations between the air bubbles and the two bitumen surfaces just before bubble jump-in behavior were calculated to be 12.8 and 13.6 nm, respectively (see Figure 4.11B and 4.11E). In the aqueous solution containing 100 mM NaCl and 1 mM $CaCl_2$, the hydrophobic interactions between air bubbles and bitumen surfaces are stronger than those in 100 mM NaCl solution (Figure 4.6A and 4.6D). The enhanced hydrophobic interaction was possibly attributed to the bridging effect of Ca^{2+} between carboxyl groups of interface-active species in bitumen, thus increasing the surface roughness (Figure 4.10) and exposing more hydrophobic moieties at the bitumen/water interface. Figure 4.11C and 4.11F illustrate the computed disjoining pressure results for bubble-bitumen in the aqueous solution containing 100 mM NaCl and 1 mM $CaCl_2$ at pH 5.8, which indicate that the attractive hydrophobic interaction plays a dominant role in the bubble attachment to the bitumen surfaces.

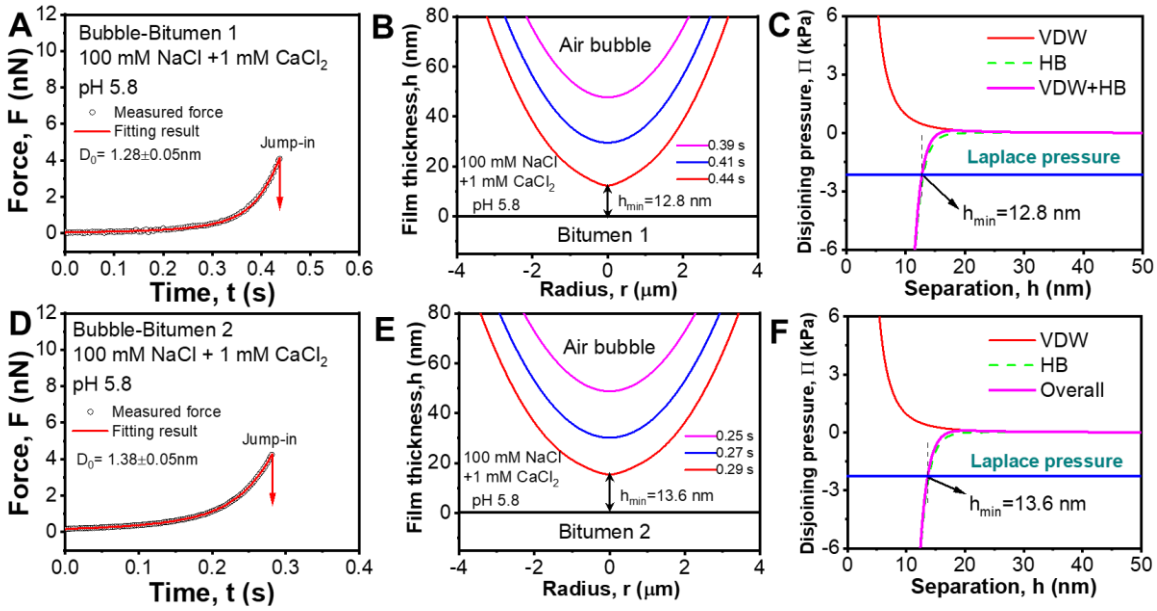

Figure 4.11. Interaction force curves, revolution of air bubble profiles and disjoining pressure results determined when air bubbles interact with (A-C) bitumen 1 surface (bubble radius R_b = 65 μm) and (D-F) bitumen 2 surface (bubble radius R_b = 62 μm) in 100 mM NaCl +1 mM $CaCl_2$ solution at pH 5.8. Black open symbol represent measured experiment results, and red solid curves stand for theoretical fitting results in (A) and (D). The changes in air bubble shape as the bubbles approach bitumen surfaces prior to jump-in, with the red lines indicating the profiles at the minimum separation distance just before the jump-in event (B, E). Disjoining pressure profiles caused by VDW and HB interactions (C, F).

4.3.3.4 Effect of Surfactant

It has been widely accepted that natural surface-active species play a key role in water-based bitumen extraction process, which modify the surface properties of bubbles, bitumen, and mineral solids (e.g., surface charge, wettability) and consequently affect the

interactions forces in this engineering system. In this work, to investigate the impact of surfactants on the bubble-bitumen interactions in various solutions, AFM coupled with a bubble probe was employed to directly quantify the forces involved, and sodium dodecyl sulfate (SDS) was selected as a representative surfactant. For ease of comparison, 100 mM NaCl solution was used as the control background solution. Figure 4.12A-C and Figure D-F show the measured surface forces between air bubbles and the surfaces of bitumen 1 and bitumen 2, respectively, under the following solution conditions: (A, D)100 mM NaCl + 1 mM SDS at pH 9, (B, E) 100 mM NaCl + 1 mM SDS at pH 5.8, and (C, F) 100 mM NaCl +1 mM $CaCl_2$ + 1 mM SDS at pH 5.8. In contrast to the SDS-free cases (see Figure 4.6, 4.7 and 4.11), the jump-in behavior of air bubbles disappeared during force measurements in aqueous solutions containing 1 mM SDS. The results and this change were mainly attributed to the adsorption of SDS molecules at both the air bubble/water and bitumen/water interfaces. The adsorbed SDS molecules lowered the hydrophobicity of air bubbles and bitumen surfaces, which consequently weakened their HB interaction, while the HB attraction was the driving force for the jump-in phenomenon. Additionally, the adsorption of SDS molecules could also introduce an additional steric repulsion between the air bubbles and bitumen surfaces, which also inhibits the jump-in behavior. It is noted that the impacts of pH and Ca^{2+} ions were not obvious in aqueous solutions containing the surfactant SDS, because the surface properties of bitumen and bubbles were mainly determined by the adsorbed SDS molecules.

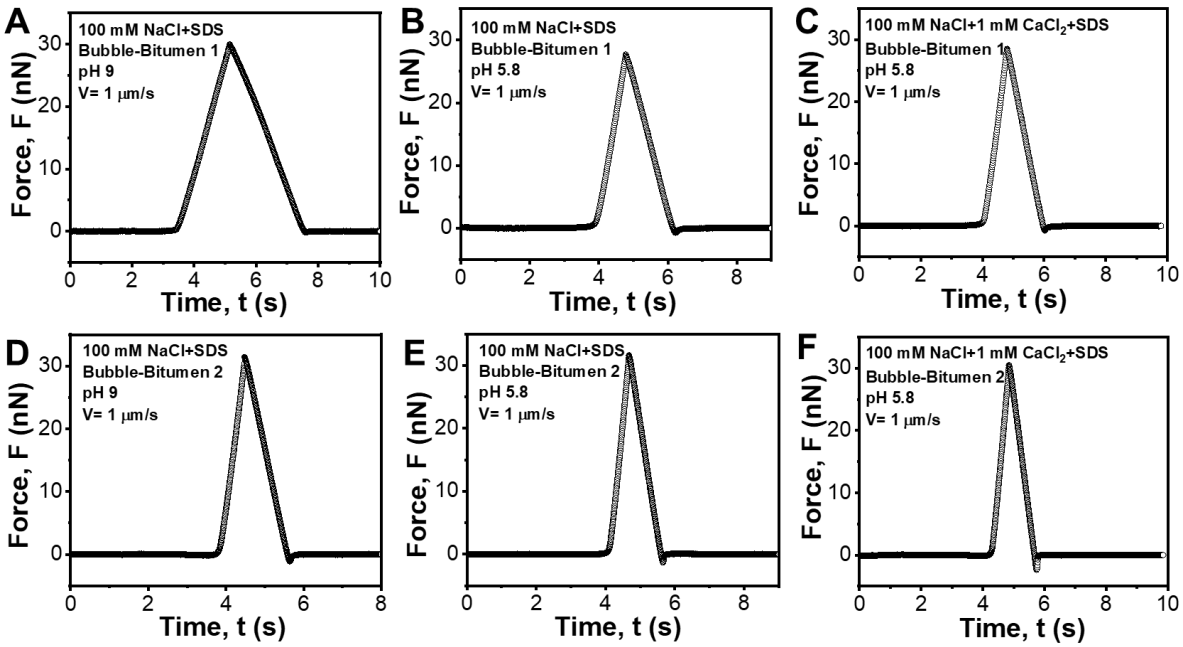

Figure 4.12. Representative surface force curves of air bubbles and the surfaces of (A-C) bitumen 1 in (A) 100 mM NaCl + 1 mM SDS solution at pH 9 (bubble radius R_b = 56 μm), (B) 100 mM NaCl + 1 mM SDS solution at pH 5.8 (bubble radius R_b = 53 μm), and (C) 100 mM NaCl +1 mM $CaCl_2$ + 1 mM SDS solution at pH 5.8 (bubble radius R_b = 59 μm). Representative force curves of air bubbles and the surfaces of (D-F) bitumen 2 in (D) 100 mM NaCl + 1 mM SDS solution at pH 9 (bubble radius R_b = 55 μm), (E) 100 mM NaCl + 1 mM SDS solution at pH 5.8 (bubble radius R_b = 58 μm), and (F) 100 mM NaCl +1 mM $CaCl_2$ + 1 mM SDS solution at pH 5.8 (bubble radius R_b = 60 μm).

4.4 Conclusions

In this work, two Athabasca bitumen samples collected from northern Alberta were characterized using various techniques. The surface forces of air bubbles and the two types of bitumen in various aqueous solutions were quantified via force measurements.

The influences of different factors, such as ionic strength, type of ions, pH, and addition of surfactant, on the interaction forces in bubble-bitumen system were systematically studied. The surface morphologies of both types of bitumen appears rougher with some distinct aggregation domains under high salt concentration and/or high pH conditions. During AFM force measurements, 'jump-in' behaviors of air bubbles to both bitumen surfaces were observed under high salinity conditions, which was mainly driven by the attractive hydrophobic interaction between the bubbles and bitumen surfaces. The hydrophobic interaction of air bubbles with bitumen 2 was found to be slightly stronger than that of the bitumen 1 case under the same solution conditions, due to their minor difference in surface hydrophobicity. In contrast, the repulsive EDL and VDW forces of bubble-bitumen for both cases were stronger than the hydrophobic interaction; thus, the jump-in event was not detected, and thin aqueous solution films of some critical thickness could be confined between the bubbles and bitumen surfaces during the approach process, which inhibits the intimate contact and attachment between the bubbles and bitumen.

The force measurement results indicate that solution pH and presence of calcium ions affect the bubble-bitumen surface forces by modulating their surface properties. Higher pH conditions could make the bitumen surfaces less hydrophobic, thus leading to weakened bubble-bitumen hydrophobic attraction. In contrast, Ca^{2+} ions could cause conformation rearrangement and aggregation of interface-active species of bitumen through their interactions with certain polar groups (e.g., -COOH) to expose more hydrophobic domains at the bitumen/water interface, as confirmed by AFM imaging, resulting in strengthened bubble-bitumen hydrophobic attraction. Interestingly, even under high salinity conditions, introducing a small quantity of surfactant such as sodium

dodecyl sulfate to the aqueous media could inhibit the attachment of air bubbles and bitumen, mainly attributed to the enhanced steric repulsion and reduced hydrophobic attraction. Such effects of surfactants on the bubble-bitumen forces are much more significant than that of solution pH and Ca^{2+}. This study has improved our understanding of the nanoscale surface interaction mechanisms of bitumen and air bubbles in complex aqueous media. The findings offer valuable insights into the manipulation of related interfacial interactions that involve deformable air bubbles in various industrial processes, including oil production, wastewater treatment, and froth flotation.

4.5 Supporting Information

4.5.1 Three-probe-liquid method

Van Oss et al. reported that the surface energy (γ) of has two primary components: Lifshitz-vdW component (γ^{LW}) and Lewis acid-base component (γ^{AB}, including electron acceptor γ^{+} and electron donor γ^{-}), as shown in Equation S4.1:

$$\gamma = \gamma^{LW} + \gamma^{AB} = \gamma^{LW} + 2\sqrt{\gamma^{+}\gamma^{-}} \tag{S4.1}$$

Based on Equation S4.1, we have the relationship between surface energies and contact angle (θ) of probe liquid on the bitumen surface, as shown in Equation S4.2:

$$\gamma_L\left(\cos\theta + 1\right) = 2\left(\sqrt{\gamma_B^{LW}\gamma_L^{LW}} + \sqrt{\gamma_B^{+}\gamma_L^{-}} + \sqrt{\gamma_B^{-}\gamma_L^{+}}\right) \tag{S4.2}$$

Where subscripts B and L refer to bitumen surface and probe liquid, respectively. According to Equation S4.2, we can determine the surface energy of the bitumen surfaces by measuring the contact angles of three different liquids with known surface energy

components. Therefore, the contact angles of three probing liquids (i.e., diiodomethane, water, and ethylene glycol) on the bitumen surface were measured by a goniometer (Ramé-Hart Instrument Co., NJ, USA) using sessile drop technique. The reported average contact angle for the two bitumen surfaces was tested by utilizing the same kind of liquids and three different testing locations. By using Equation S4.3, we can calculate the surface energy components of bitumen surfaces, and the results are summarized in Table S4.1.

$$\begin{pmatrix} \sqrt{\gamma_B^{LW}} \\ \sqrt{\gamma_B^{+}} \\ \sqrt{\gamma_B^{-}} \end{pmatrix} = \left\{ \left[2 \begin{pmatrix} \sqrt{\gamma_{L1}^{LW}} & \sqrt{\gamma_{L1}^{-}} & \sqrt{\gamma_{L1}^{+}} \\ \sqrt{\gamma_{L2}^{LW}} & \sqrt{\gamma_{L2}^{-}} & \sqrt{\gamma_{L2}^{+}} \\ \sqrt{\gamma_{L3}^{LW}} & \sqrt{\gamma_{L3}^{-}} & \sqrt{\gamma_{L3}^{+}} \end{pmatrix} \right]^{-1} \begin{pmatrix} \gamma_{L1}(\cos\theta_1 + 1) \\ \gamma_{L2}(\cos\theta_2 + 1) \\ \gamma_{L3}(\cos\theta_3 + 1) \end{pmatrix} \right\} \quad \text{(S4.3)}$$

Table S4.1. Surface Energy Components (mJ/m^2) of Three Probing Liquids Reported in the Literature, [191-192] Measured Contact Angle Values (°) of Three Probing Liquids (Diiodomethane, Water, and Diethylene Glycol) on Two Bitumen Surfaces, and Calculated Surface Energy Components (mJ/m^2) of Two Bitumen.

	γ^{LW}	γ^{+}	γ^{-}	γ^{AB}	γ	Measured contact angle (Bitumen 1)	Measured contact angle (Bitumen 2)
Diiodomethane	50.60	0.00	0.00	0.00	50.80	33.6±1.8	28.4±1.6
Water	21.80	25.50	25.50	51.00	72.80	97.3±1.3	100.6±1.5
Diethylene glycol	29.00	1.92	47.00	19.00	48.00	72.9±1.2	69.7±1.1
Bitumen 1(calculated)	42.70	0.67	1.15	1.75	44.42		
Bitumen 2(calculated)	44.87	0.37	0.09	0.36	45.23		

CHAPTER 5 Conclusions and Future Work

5.1 Major Conclusions and Contributions

Interfacial interactions among gas bubbles, solid particles and liquid drops drive numerous interfacial phenomena and biophysical and industrial processes, such as drug and gene delivery in bioengineering, bitumen flotation, oil/water separation, and water treatment. In this thesis work, the interfacial forces and interaction mechanisms between deformable air bubbles/oil drops and hydrophobic polymers, between air bubbles and asphaltenes or asphaltenes-toluene droplets, as well as between air bubbles and bitumen surfaces under complex aqueous solution conditions have been systematically quantified by using nanomechanical technologies. The effects of aqueous chemistry (e.g., ion type, ion concentration, pH, surfactants) and hydrodynamic conditions (i.e., interaction velocities) on their surface interactions have also been systematically investigated. This thesis work has significantly enhanced the fundamental understanding of the nanoscale surface interaction mechanisms between hydrophobic polymers, asphaltenes, bitumen, oil droplets, and gas bubbles in complex aqueous solutions. The research is entirely original, and the results in this thesis provide valuable insights into the effective modulation of interfacial interactions in various interfacial processes, such as oily water treatment, oil production and other interfacial processes.

The major conclusions and original contributions are listed below:

(1) The interaction forces between a model hydrophobic polymer (i.e., polystyrene of different molecular weights) and air bubbles or oil droplets in aqueous solutions have been systematically characterized and quantified for the *first* time. The effects of polymer molecular weight, solvent (i.e., addition of ethanol to water), the presence of surface-

active species (surfactants), and hydrodynamic conditions have been systematically investigated. PS surfaces of different molecular weights possess the same surface hydrophobicity. It was found that the PS of low molecular weight (i.e., PS590 and PS810) showed slightly weaker hydrophobic interactions with air bubbles or oil droplets, as compared to glassy PS of higher molecular weight (i.e., PS1110, PS2330, PS46300 and PS1M). The slightly weaker hydrophobic interaction of viscous PS of low molecular weights is likely due to (i) more flexible chain mobility of PS with low molecular weight in the viscous state at room temperature (i.e., PS590 and PS810) and (ii) increased surface roughness of PS590 and PS810 surfaces in 1 M NaCl as compared to that of the PS surfaces of higher molecular weight. The hydrophobic interaction between PS and air bubbles in 1 M NaCl aqueous solution with 10 vol % ethanol was weaker than that in the pure aqueous solution. Such effects on the hydrophobic interactions are possibly achieved by influencing the structuring/ordering of water molecules close to the hydrophobic polymer surfaces by tuning the surface chain mobility and surface roughness of polymers. The addition of three types of surfactants (i.e., CTAC, FC-127, or SDS) to the aqueous media was able to completely suppress the attachment of the hydrophobic polymer and air bubbles or oil droplets, which was most likely caused by the additional steric repulsion due to the adsorbed surface-active species at various bubble/ polymer/oil interfaces. It was also found that, in addition to the various surface forces, hydrodynamic conditions also significantly influence the interactions of hydrophobic polymers and deformable objects (i.e., bubbles, droplets). The higher the approaching velocity of bubbles or oil droplets to the polymer surfaces, the stronger the hydrodynamic repulsion, which could work jointly with the surface forces (e.g., VDW, EDL, and HB interactions)

to influence the related colloidal and interfacial phenomena. These results have improved the fundamental understanding of the interaction mechanisms between hydrophobic polymer surfaces and highly deformable bubbles or oil droplets. This part of the work also provides useful implications on developing effective approaches for modulating the related colloidal interactions in various engineering applications by tuning the solution chemistry, surface properties of substrates or hydrodynamic conditions.

(2) In the second part of the thesis work, surface forces of air bubbles with asphaltenes or asphaltene-oil droplets in aqueous media have been quantitatively characterized. The effects of various factors, such as the concentrations of asphaltenes and salts, aqueous pH, divalent cations and the surfactants were examined. The results demonstrate that the adhesion between bubbles and asphaltenes is enhanced under the high salt condition, mainly due to significantly suppressed EDL interaction. Interestingly, solution pH has limited effect on the adhesion. It is also demonstrated that higher asphaltenes concentration in the oil droplets strengthens its hydrophobic attraction with air bubbles, leading to their surface contact. However, under low salinity condition (i.e., 1 mM NaCl), the EDL and VDW repulsion dominates the bubble-oil interactions, preventing the bubble-oil attachment. In contrast, high salt concentrations reduce the repulsive EDL forces, and the hydrophobic attraction drove the bubbles to attach to asphaltene-toluene droplets. Increasing the solution pH from pH 4 to pH 10 results in both air bubbles and asphaltenes-toluene droplets becoming more negatively charged, enhancing the EDL repulsion and weakening the HB attraction, with no surface attachment observed under low salinity conditions. It is also found that the addition of divalent cations such as Ca^{2+} weakens the hydrophobic attraction of bubbles and asphaltenes-toluene droplets, as the

Ca^{2+} ions induce conformational changes and clustering of interfacial asphaltenes. Introducing surfactant species (such as CTAC and SDS) to the aqueous solutions inhibits the adhesion of air bubbles with asphaltenes-toluene droplets, which is because of the strong steric interaction caused by interfacial adsorption of surfactant molecules.

(3) In the third part of the thesis work, two different bitumen samples from north Alberta have been systematically characterized using the Dean-Stark method, thermogravimetric analysis, Elemental Analysis, and Fourier transformation infrared spectroscopy. The interaction forces between air bubbles and two types of Athabasca bitumen samples in aqueous media with varying pH, salinity, type of cations and surfactants have been directly measured by using a bubble probe atomic force microscope (AFM) technique. It was found based on AFM imaging that the bitumen surfaces become rougher when exposed to high concentrations of NaCl and $CaCl_2$ or alkaline environments. Surface force results reveal that ionic strength, solution pH, and the presence of surfactants significantly influence the interaction and attachment behaviors between bubbles and bitumen. It is found that a theoretical model based on Reynolds lubrication theory and augmented Young-Laplace equation, with the inclusion of disjoining pressure, could provide an accurate description of the force results. In solutions of low salinity (e.g., 1 mM NaCl), electric double layer (EDL) repulsion dominates the bubble-bitumen interaction, preventing attachment of the bubbles to bitumen surfaces, and such effects are further enhanced by increasing solution pH. Under high salinity conditions, the EDL interactions are significantly suppressed, and the hydrophobic interaction becomes dominant, which overcomes the van der Waals repulsion and causes bubble-bitumen attachment. Increasing the solution pH weakens the hydrophobic interaction, while the

addition of calcium ions strengthens the hydrophobic interaction which enhances the bubble-bitumen attachment. Interestingly, even under high salinity conditions, the addition of a small amount of surfactants to the aqueous media can suppress bubble-bitumen attachment, mainly due to weakened hydrophobic interaction and raised steric interaction. This work provides valuable nanoscale insights into the surface interaction mechanisms of bubbles and bitumen in complex aqueous media, with practical implications for manipulating related interfacial interactions in bitumen production, water treatment, and other industrial processes.

5.2 Prospects

In this study, we have improved the fundamental understanding of the nanoscale surface interaction mechanisms among air bubbles, oil droplets, hydrophobic polymers, bitumen, and asphaltenes in complex aqueous solutions. The research findings provide valuable insights for modulating related interfacial interactions in many industrial processes such as oil production and wastewater treatment. All these experimental measurements were conducted under ambient conditions. However, in practical applications, bubbles generally interact with other bubbles and objects (e.g., particles, emulsion droplets, cells) in complex fluids, often under harsh environmental conditions (e.g., high temperature, high pressure). Many of the nanomechanical technologies do not allow measurements under such harsh environmental conditions. Future studies in this field may focus on several areas to further advance the characterization and modulation of surface interactions among gas bubbles, oil droplets and solid particles/surfaces (e.g., bitumen, polymers), as listed below.

(1) Developing more effective bubble/drop manipulation methods to achieve precise control of bubble/drop behaviors and their surface interactions.

(2) Conducting experimental measurements under more complex fluid conditions (e.g., water chemistry, solvent conditions, interface-active species) which are close to practical industrial fluid chemistries.

(3) Developing nanomechanical technologies that allow surface force measurements under harsh environmental conditions (e.g., high temperature, high pressure, strong hydrodynamics), which are close to the environmental conditions in many industrial operations.

(4) Applying non-linear optical technique such as sum frequency generation vibrational spectroscopy to characterize the solid/fluid/gas interfacial properties, and correlating such molecular information to the surface force results and various interfacial phenomena.

Bibliography

1. Masliyah, J. H.; Czarnecki, J.; Xu, Z., Handbook on theory and practice on bitumen recovery from athabasca oil sands. **2011**.

2. Masliyah, J.; Zhou, Z. J.; Xu, Z.; Czarnecki, J.; Hamza, H., Understanding water-based bitumen extraction from Athabasca oil sands. *The Canadian Journal of Chemical Engineering* **2004,** *82* (4), 628-654.

3. Butler, R. M., Steam-assisted gravity drainage: concept, development, performance and future. *Journal of Canadian Petroleum Technology* **1994,** *33* (02), 44-50.

4. Khuntia, S.; Majumder, S. K.; Ghosh, P., Microbubble-aided water and wastewater purification: a review. *Reviews in Chemical Engineering* **2012,** *28* (4-6), 191-221.

5. Hiemenz, P.; Rajagopalan, R., Principles of Colloid and Surface Chemistry CRC Press. 1997.

6. Henry, W., III. Experiments on the quantity of gases absorbed by water, at different temperatures, and under different pressures. *Philosophical Transactions of the Royal Society of London* **1803,** (93), 29-274.

7. Ushikubo, F. Y.; Furukawa, T.; Nakagawa, R.; Enari, M.; Makino, Y.; Kawagoe, Y.; Shiina, T.; Oshita, S., Evidence of the existence and the stability of nano-bubbles in water. *Colloids and Surfaces A: Physicochemical and Engineering Aspects* **2010,** *361* (1-3), 31-37.

8. Hampton, M. A.; Nguyen, A. V., Nanobubbles and the nanobubble bridging capillary force. *Advances in colloid and interface science* **2010,** *154* (1-2), 30-55.

9. Najafi, A. S.; Drelich, J.; Yeung, A.; Xu, Z.; Masliyah, J., A novel method of measuring electrophoretic mobility of gas bubbles. *Journal of colloid and interface science* **2007,** *308* (2), 344-350.

10. Bunkin, N.; Suyazov, N.; Shkirin, A.; Ignat'ev, P.; Indukaev, K., Study of nanostructure of highly purified water by measuring scattering matrix elements of laser radiation. *Physics of Wave Phenomena* **2008,** *16*, 243-260.

11. Ohgaki, K.; Khanh, N. Q.; Joden, Y.; Tsuji, A.; Nakagawa, T., Physicochemical approach to nanobubble solutions. *Chemical Engineering Science* **2010,** *65* (3), 1296-1300.

12. Pugh, R.; Yoon, R., Hydrophobicity and rupture of thin aqueous films. *Journal of colloid and interface science* **1994,** *163* (1), 169-176.

13. Shaw, D. J., *Introduction to colloid and surface chemistry*. Butterworths: 1980.

14. Hunter, R. J., *Zeta potential in colloid science: principles and applications*. Academic press: 2013; Vol. 2.

15. Fukui, Y.; Yuu, S., Collection of submicron particles in electro-flotation. *Chemical Engineering Science* **1980,** *35* (5), 1097-1105.

16. Kubota, K.; GJ, J., A study of the electrophoretic mobility of a very small inert gas bubble suspended in aqueous inorganic electrolyte and cationic surfactant solutions. *Journal of chemical engineering of Japan* **1993,** *26* (1), 7-12.

17. Perkin, S.; Kampf, N.; Klein, J., Long-range attraction between charge-mosaic surfaces across water. *Physical review letters* **2006,** *96* (3), 038301.

18. Silbert, G.; Ben-Yaakov, D.; Dror, Y.; Perkin, S.; Kampf, N.; Klein, J., Long-ranged attraction between disordered heterogeneous surfaces. *Physical review letters* **2012,** *109* (16), 168305.

19. Meyer, E. E.; Rosenberg, K. J.; Israelachvili, J., Recent progress in understanding hydrophobic interactions. *Proceedings of the National Academy of Sciences* **2006,** *103* (43), 15739-15746.

20. Ducker, W. A.; Senden, T. J.; Pashley, R. M., Direct measurement of colloidal forces using an atomic force microscope. *Nature* **1991,** *353* (6341), 239-241.

21. Balasuriya, T. S.; Dagastine, R. R., Interaction forces between bubbles in the presence of novel responsive peptide surfactants. *Langmuir* **2012,** *28* (50), 17230-17237.

22. Cho, S.-H.; Kim, J.-Y.; Chun, J.-H.; Kim, J.-D., Ultrasonic formation of nanobubbles and their zeta-potentials in aqueous electrolyte and surfactant solutions. *Colloids and Surfaces A: Physicochemical and Engineering Aspects* **2005,** *269* (1-3), 28-34.

23. Zenit, R.; Feng, J., Hydrodynamic interactions among bubbles, drops, and particles in non-Newtonian liquids. *Annual review of fluid mechanics* **2018,** *50*, 505-534.

24. Tabor, R. F.; Wu, C.; Lockie, H.; Manica, R.; Chan, D. Y.; Grieser, F.; Dagastine, R. R., Homo-and hetero-interactions between air bubbles and oil droplets measured by atomic force microscopy. *Soft Matter* **2011,** *7* (19), 8977-8983.

25. Creux, P.; Lachaise, J.; Graciaa, A.; Beattie, J. K.; Djerdjev, A. M., Strong specific hydroxide ion binding at the pristine oil/water and air/water interfaces. *The Journal of Physical Chemistry B* **2009,** *113* (43), 14146-14150.

26. Zhang, L.; Shi, C.; Lu, Q.; Liu, Q.; Zeng, H., Probing molecular interactions of asphaltenes in heptol using a surface forces apparatus: implications on stability of water-in-oil emulsions. *Langmuir* **2016,** *32* (19), 4886-4895.

27. Pashazanusi, L.; Lwoya, B.; Oak, S.; Khosla, T.; Albert, J. N.; Tian, Y.; Bansal, G.; Kumar, N.; Pesika, N. S., Enhanced adhesion of mosquitoes to rough surfaces. *ACS applied materials & interfaces* **2017,** *9* (28), 24373-24380.

28. Zhang, X.; Kumar, A.; Scales, P. J., Effects of solvency and interfacial nanobubbles on surface forces and bubble attachment at solid surfaces. *Langmuir* **2011,** *27* (6), 2484-2491.

29. Liu, J.; Xu, Z.; Masliyah, J., Studies on bitumen− silica interaction in aqueous solutions by atomic force microscopy. *Langmuir* **2003,** *19* (9), 3911-3920.

30. Long, J.; Zhang, L.; Xu, Z.; Masliyah, J. H., Colloidal interactions between Langmuir− Blodgett bitumen films and fine solid particles. *Langmuir* **2006,** *22* (21), 8831-8839.

31. Natarajan, A.; Xie, J.; Wang, S.; Liu, Q.; Masliyah, J.; Zeng, H.; Xu, Z., Understanding molecular interactions of asphaltenes in organic solvents using a surface force apparatus. *The Journal of Physical Chemistry C* **2011,** *115* (32), 16043-16051.

32. Zhang, L.; Xie, L.; Shi, C.; Huang, J.; Liu, Q.; Zeng, H., Mechanistic understanding of asphaltene surface interactions in aqueous media. *Energy & Fuels* **2017,** *31* (4), 3348-3357.

33. Pushkarova, R. A.; Horn, R. G., Surface forces measured between an air bubble and a solid surface in water. *Colloids and Surfaces A: Physicochemical and Engineering Aspects* **2005,** *261* (1-3), 147-152.

34. Tabor, D.; Winterton, R. H. S., The direct measurement of normal and retarded van der Waals forces. *Proceedings of the Royal Society of London. A. Mathematical and Physical Sciences* **1969,** *312* (1511), 435-450.

35. Israelachvili, J. N.; Tabor, D., The measurement of van der Waals dispersion forces in the range 1.5 to 130 nm. *Proceedings of the Royal Society of London. A. Mathematical and Physical Sciences* **1972,** *331* (1584), 19-38.

36. Israelachvili, J. N.; Adams, G., Direct measurement of long range forces between two mica surfaces in aqueous KNO3 solutions. *Nature* **1976,** *262* (5571), 774-776.

37. Binnig, G.; Quate, C. F.; Gerber, C., Atomic force microscope. *Physical review letters* **1986,** *56* (9), 930.

38. Ashkin, A., Acceleration and trapping of particles by radiation pressure. *Physical review letters* **1970,** *24* (4), 156.

39. Ashkin, A.; Dziedzic, J. M.; Bjorkholm, J. E.; Chu, S., Observation of a single-beam gradient force optical trap for dielectric particles. *Optics letters* **1986,** *11* (5), 288-290.

40. Derjaguin, B.; Rabinovich, Y. I.; Churaev, N., Direct measurement of molecular forces. *Nature* **1978,** *272* (5651), 313-318.

41. Butt, H.-J.; Jaschke, M.; Ducker, W., Measuring surface forces in aqueous electrolyte solution with the atomic force microscope. *Bioelectrochemistry and Bioenergetics* **1995,** *38* (1), 191-201.

42. Israelachvili, J.; Min, Y.; Akbulut, M.; Alig, A.; Carver, G.; Greene, W.; Kristiansen, K.; Meyer, E.; Pesika, N.; Rosenberg, K., Recent advances in the surface forces apparatus (SFA) technique. *Reports on Progress in Physics* **2010,** *73* (3), 036601.

43. Shi, C.; Zhang, L.; Xie, L.; Lu, X.; Liu, Q.; He, J.; Mantilla, C. A.; Van den Berg, F. G.; Zeng, H., Surface interaction of water-in-oil emulsion droplets with interfacially active asphaltenes. *Langmuir* **2017,** *33* (5), 1265-1274.

44. Liu, J.; Cui, X.; Huang, J.; Xie, L.; Tan, X.; Liu, Q.; Zeng, H., Understanding the stabilization mechanism of bitumen-coated fine solids in organic media from non-aqueous extraction of oil sands. *Fuel* **2019,** *242*, 255-264.

45. Gong, L.; Zhang, L.; Xiang, L.; Zhang, J.; Fattahpour, V.; Mamoudi, M.; Roostaei, M.; Fermaniuk, B.; Luo, J.-L.; Zeng, H., Surface Interactions between Water-in-Oil Emulsions with Asphaltenes and Electroless Nickel–Phosphorus Coating. *Langmuir* **2020,** *36* (4), 897-905.

46. Shi, C.; Xie, L.; Zhang, L.; Lu, X.; Zeng, H., Probing the interaction mechanism between oil droplets with asphaltenes and solid surfaces using AFM. *Journal of colloid and interface science* **2020,** *558*, 173-181.

47. Xie, L.; Shi, C.; Cui, X.; Huang, J.; Wang, J.; Liu, Q.; Zeng, H., Probing the interaction mechanism between air bubbles and bitumen surfaces in aqueous media using bubble probe atomic force microscopy. *Langmuir* **2018,** *34* (3), 729-738.

48. Kegler, K.; Salomo, M.; Kremer, F., Forces of interaction between DNA-grafted colloids: an optical tweezer measurement. *Physical review letters* **2007,** *98* (5), 058304.

49. He, L.; Lin, F.; Li, X.; Sui, H.; Xu, Z., Interfacial sciences in unconventional petroleum production: from fundamentals to applications. *Chemical Society Reviews* **2015,** *44* (15), 5446-5494.

50. Drummond, C.; Israelachvili, J., Fundamental studies of crude oil–surface water interactions and its relationship to reservoir wettability. *Journal of Petroleum Science and Engineering* **2004,** *45* (1-2), 61-81.

51. Christenson, H. K.; Israelachvili, J. N., Direct measurements of interactions and viscosity of crude oils in thin films between model clay surfaces. *Journal of Colloid and interface Science* **1987,** *119* (1), 194-202.

52. Chen, S.-Y.; Kaufman, Y.; Kristiansen, K.; Seo, D.; Schrader, A. M.; Alotaibi, M. B.; Dobbs, H. A.; Cadirov, N. A.; Boles, J. R.; Ayirala, S. C., Effects of salinity on oil recovery (the "Dilution Effect"): Experimental and theoretical studies of crude oil/brine/carbonate surface restructuring and associated physicochemical interactions. *Energy & Fuels* **2017,** *31* (9), 8925-8941.

53. Zhang, J.; Zeng, H., Intermolecular and surface interactions in engineering processes. *Engineering* **2021,** *7* (1), 63-83.

54. Schäffer, E.; Nørrelykke, S. F.; Howard, J., Surface forces and drag coefficients of microspheres near a plane surface measured with optical tweezers. *Langmuir* **2007,** *23* (7), 3654-3665.

55. Lu, Q.; Wang, J.; Faghihnejad, A.; Zeng, H.; Liu, Y., Understanding the molecular interactions of lipopolysaccharides during E. coli initial adhesion with a surface forces apparatus. *Soft Matter* **2011,** *7* (19), 9366-9379.

56. Butt, H.-J.; Cappella, B.; Kappl, M., Force measurements with the atomic force microscope: Technique, interpretation and applications. *Surface science reports* **2005,** *59* (1-6), 1-152.

57. Israelachvili, J. N., Measurement of forces between surfaces immersed in electrolyte solutions. *Faraday Discussions of the Chemical Society* **1978,** *65*, 20-24.

58. Israelachvili, J.; Pashley, R., The hydrophobic interaction is long range, decaying exponentially with distance. *Nature* **1982,** *300* (5890), 341-342.

59. Zhang, J.; Xiang, L.; Yan, B.; Zeng, H., Nanomechanics of anion− π interaction in aqueous solution. *Journal of the American Chemical Society* **2020,** *142* (4), 1710-1714.

60. Lu, Q.; Oh, D. X.; Lee, Y.; Jho, Y.; Hwang, D. S.; Zeng, H., Nanomechanics of cation–π interactions in aqueous solution. *Angewandte Chemie* **2013,** *125* (14), 4036-4040.

61. Faghihnejad, A.; Zeng, H., Hydrophobic interactions between polymer surfaces: using polystyrene as a model system. *Soft Matter* **2012,** *8* (9), 2746-2759.

62. Xiang, L.; Gong, L.; Zhang, J.; Zhang, L.; Hu, W.; Wang, W.; Lu, Q.; Zeng, H., Probing molecular interactions of PEGylated chitosan in aqueous solutions using a surface force apparatus. *Physical Chemistry Chemical Physics* **2019,** *21* (37), 20571-20581.

63. Israelachvili, J., Thin film studies using multiple-beam interferometry. *Journal of Colloid and Interface Science* **1973,** *44* (2), 259-272.

64. Drake, B.; Prater, C.; Weisenhorn, A.; Gould, S.; Albrecht, T.; Quate, C.; Cannell, D.; Hansma, H.; Hansma, P., Imaging crystals, polymers, and processes in water with the atomic force microscope. *Science* **1989,** *243* (4898), 1586-1589.

65. Zeng, H., *Polymer adhesion, friction, and lubrication*. John Wiley & Sons: 2013.

66. Akamine, S.; Barrett, R.; Quate, C., Improved atomic force microscope images using microcantilevers with sharp tips. *Applied Physics Letters* **1990,** *57* (3), 316-318.

67. Yang, D.; Xie, L.; Mao, X.; Gong, L.; Peng, X.; Peng, Q.; Wang, T.; Liu, Q.; Zeng, H.; Zhang, H., Probing hydrophobic interactions between polymer surfaces and air bubbles or oil droplets: effects of molecular weight and surfactants. *Langmuir* **2021,** *38* (17), 5257-5268.

68. Cui, X.; Liu, J.; Xie, L.; Huang, J.; Liu, Q.; Israelachvili, J. N.; Zeng, H., Modulation of hydrophobic interaction by mediating surface nanoscale structure and chemistry, not monotonically by hydrophobicity. *Angewandte Chemie* **2018,** *130* (37), 12079-12084.

69. Cui, X.; Shi, C.; Zhang, S.; Xie, L.; Liu, J.; Jiang, D.; Zeng, H., Probing the effect of salinity and pH on surface interactions between air bubbles and hydrophobic solids: implications for colloidal assembly at air/water interfaces. *Chemistry–An Asian Journal* **2017,** *12* (13), 1568-1577.

70. Gong, L.; Wang, J.; Zhang, L.; Fattahpour, V.; Mamoudi, M.; Roostaei, M.; Fermaniuk, B.; Luo, J.-L.; Zeng, H., Fouling mechanisms of asphaltenes and fine solids on bare and electroless nickel-phosphorus coated carbon steel. *Fuel* **2019,** *252*, 188-199.

71. Liu, J.; Cui, X.; Xie, L.; Huang, J.; Zhang, L.; Liu, J.; Wang, X.; Wang, J.; Zeng, H., Probing effects of molecular-level heterogeneity of surface hydrophobicity on hydrophobic interactions in air/water/solid systems. *Journal of colloid and interface science* **2019,** *557*, 438-449.

72. Shi, C.; Chan, D. Y.; Liu, Q.; Zeng, H., Probing the hydrophobic interaction between air bubbles and partially hydrophobic surfaces using atomic force microscopy. *The Journal of Physical Chemistry C* **2014,** *118* (43), 25000-25008.

73. Xie, L.; Shi, C.; Wang, J.; Huang, J.; Lu, Q.; Liu, Q.; Zeng, H., Probing the interaction between air bubble and sphalerite mineral surface using atomic force microscope. *Langmuir* **2015,** *31* (8), 2438-2446.

74. Shi, C.; Cui, X.; Xie, L.; Liu, Q.; Chan, D. Y.; Israelachvili, J. N.; Zeng, H., Measuring forces and spatiotemporal evolution of thin water films between an air bubble and solid surfaces of different hydrophobicity. *ACS nano* **2015,** *9* (1), 95-104.

75. Gong, L.; Qiu, X.; Zhang, L.; Huang, J.; Hu, W.; Xiang, L.; Zhu, D.; Sabbagh, R.; Mahmoudi, M.; Fattahpour, V., Probing the interaction mechanism between oil-in-water emulsions and electroless nickel–phosphorus coating with implications for antifouling in oil production. *Energy & Fuels* **2018,** *33* (5), 3764-3775.

76. Qiao, C.; Yang, D.; Mao, X.; Xie, L.; Gong, L.; Peng, X.; Peng, Q.; Wang, T.; Zhang, H.; Zeng, H., Recent advances in bubble-based technologies: Underlying interaction mechanisms and applications. *Applied Physics Reviews* **2021,** *8* (1), 011315.

77. Ducker, W. A.; Xu, Z.; Israelachvili, J. N., Measurements of hydrophobic and DLVO forces in bubble-surface interactions in aqueous solutions. *Langmuir* **1994,** *10* (9), 3279-3289.

78. Butt, H.-J., Measuring electrostatic, van der Waals, and hydration forces in electrolyte solutions with an atomic force microscope. *Biophysical journal* **1991,** *60* (6), 1438-1444.

79. Israelachvili, J. N., *Intermolecular and surface forces*. Academic press: 2011.

80. Ivanov, I.; Dimitrov, D.; Somasundaran, P.; Jain, R., Thinning of films with deformable surfaces: Diffusion-controlled surfactant transfer. *Chemical engineering science* **1985,** *40* (1), 137-150.

81. Stevens, H.; Considine, R. F.; Drummond, C. J.; Hayes, R. A.; Attard, P., Effects of degassing on the long-range attractive force between hydrophobic surfaces in water. *Langmuir* **2005,** *21* (14), 6399-6405.

82. Manica, R.; Klaseboer, E.; Chan, D. Y., Dynamic interactions between drops—a critical assessment. *Soft Matter* **2008,** *4* (8), 1613-1616.

83. Manica, R.; Chan, D. Y., Drainage of the air–water–quartz film: experiments and theory. *Physical Chemistry Chemical Physics* **2011,** *13* (4), 1434-1439.

84. Manor, O.; Vakarelski, I. U.; Tang, X.; O'Shea, S. J.; Stevens, G. W.; Grieser, F.; Dagastine, R. R.; Chan, D. Y., Hydrodynamic boundary conditions and dynamic forces between bubbles and surfaces. *Physical review letters* **2008,** *101* (2), 024501.

85. Liu, J.; Xu, Z.; Masliyah, J., Colloidal forces between bitumen surfaces in aqueous solutions measured with atomic force microscope. *Colloids and Surfaces A: Physicochemical and Engineering Aspects* **2005,** *260* (1-3), 217-228.

86. Chan, D. Y.; Klaseboer, E.; Manica, R., Film drainage and coalescence between deformable drops and bubbles. *Soft Matter* **2011,** *7* (6), 2235-2264.

87. Manor, O.; Vakarelski, I. U.; Stevens, G. W.; Grieser, F.; Dagastine, R. R.; Chan, D. Y., Dynamic forces between bubbles and surfaces and hydrodynamic boundary conditions. *Langmuir* **2008,** *24* (20), 11533-11543.

88. Shi, C.; Zhang, L.; Xie, L.; Lu, X.; Liu, Q.; Mantilla, C. A.; van den Berg, F. G.; Zeng, H., Interaction mechanism of oil-in-water emulsions with asphaltenes determined using droplet probe AFM. *Langmuir* **2016,** *32* (10), 2302-2310.

89. Xie, L.; Lu, Q.; Tan, X.; Liu, Q.; Tang, T.; Zeng, H., Interfacial behavior and interaction mechanism of pentol/water interface stabilized with asphaltenes. *Journal of colloid and interface science* **2019,** *553*, 341-349.

90. Zeng, H.; Shi, C.; Huang, J.; Li, L.; Liu, G.; Zhong, H., Recent experimental advances on hydrophobic interactions at solid/water and fluid/water interfaces. *Biointerphases* **2016,** *11* (1), 018903.

91. Xie, L.; Shi, C.; Cui, X.; Zeng, H., Surface forces and interaction mechanisms of emulsion drops and gas bubbles in complex fluids. *Langmuir* **2017,** *33* (16), 3911-3925.

92. Zhang, L.; Xie, L.; Cui, X.; Chen, J.; Zeng, H., Intermolecular and surface forces at solid/oil/water/gas interfaces in petroleum production. *Journal of colloid and interface science* **2019,** *537*, 505-519.

93. Khademhosseini, A.; Langer, R.; Borenstein, J.; Vacanti, J. P., Microscale technologies for tissue engineering and biology. *Proceedings of the National Academy of Sciences* **2006,** *103* (8), 2480-2487.

94. Li, L.; Yan, B.; Yang, J.; Chen, L.; Zeng, H., Novel mussel-inspired injectable self-healing hydrogel with anti-biofouling property. *Advanced Materials* **2015,** *27* (7), 1294-1299.

95. Xue, D.; Ma, L.; Tian, Y.; Zeng, Q.; Tu, B.; Luo, W.; Wen, S.; Luo, J., Light-controlled friction by carboxylic azobenzene molecular self-assembly layers. *Frontiers in Chemistry* **2021,** *9*, 496.

96. Li, J.; Wang, A.; Zhao, L.; Dong, Q.; Wang, M.; Xu, H.; Yan, X.; Bai, S., Self-assembly of monomeric hydrophobic photosensitizers with short peptides forming photodynamic nanoparticles with real-time tracking property and without the need of release in vivo. *ACS applied materials & interfaces* **2018,** *10* (34), 28420-28427.

97. Mao, Z.; Xu, H.; Wang, D., Molecular Mimetic Self-Assembly of Colloidal Particles. *Advanced Functional Materials* **2010,** *20* (7), 1053-1074.

98. Liu, H.; Liu, X.; Meng, J.; Zhang, P.; Yang, G.; Su, B.; Sun, K.; Chen, L.; Han, D.; Wang, S., Hydrophobic interaction-mediated capture and release of cancer cells on thermoresponsive nanostructured surfaces. *Advanced Materials* **2013,** *25* (6), 922-927.

99. Janson, J.-C., *Protein purification: principles, high resolution methods, and applications*. John Wiley & Sons: 2012; Vol. 151.

100. Kataoka, K.; Harada, A.; Nagasaki, Y., Block copolymer micelles for drug delivery: design, characterization and biological significance. *Advanced drug delivery reviews* **2012,** *64*, 37-48.

101. Xing, Y.; Gui, X.; Pan, L.; Pinchasik, B.-E.; Cao, Y.; Liu, J.; Kappl, M.; Butt, H.-J., Recent experimental advances for understanding bubble-particle attachment in flotation. *Advances in colloid and interface science* **2017,** *246*, 105-132.

102. Wang, S.; Liu, K.; Yao, X.; Jiang, L., Bioinspired surfaces with superwettability: new insight on theory, design, and applications. *Chemical reviews* **2015,** *115* (16), 8230-8293.

103. He, K.; Duan, H.; Chen, G. Y.; Liu, X.; Yang, W.; Wang, D., Cleaning of oil fouling with water enabled by zwitterionic polyelectrolyte coatings: overcoming the imperative challenge of oil–water separation membranes. *ACS nano* **2015,** *9* (9), 9188-9198.

104. Hu, W.; Cui, X.; Xiang, L.; Gong, L.; Zhang, L.; Gao, M.; Wang, W.; Zhang, J.; Liu, F.; Yan, B., Tannic acid modified MoS2 nanosheet membranes with superior water flux and ion/dye rejection. *Journal of colloid and interface science* **2020,** *560*, 177-185.

105. Yu, L.; Chen, G. Y.; Xu, H.; Liu, X., Substrate-independent, transparent oil-repellent coatings with self-healing and persistent easy-sliding oil repellency. *ACS nano* **2016,** *10* (1), 1076-1085.

106. Cui, X.; Liu, J.; Xie, L.; Huang, J.; Liu, Q.; Israelachvili, J. N.; Zeng, H., Modulation of hydrophobic interaction by mediating surface nanoscale structure and chemistry, not monotonically by hydrophobicity. *Angewandte Chemie International Edition* **2018,** *57* (37), 11903-11908.

107. Tabor, R. F.; Grieser, F.; Dagastine, R. R.; Chan, D. Y., The hydrophobic force: measurements and methods. *Physical Chemistry Chemical Physics* **2014,** *16* (34), 18065-18075.

108. Chandler, D., Interfaces and the driving force of hydrophobic assembly. *Nature* **2005,** *437* (7059), 640-647.

109. Tabor, R. F.; Wu, C.; Grieser, F.; Dagastine, R. R.; Chan, D. Y., Measurement of the hydrophobic force in a soft matter system. *The journal of physical chemistry letters* **2013,** *4* (22), 3872-3877.

110. Vakarelski, I. U.; Lee, J.; Dagastine, R. R.; Chan, D. Y.; Stevens, G. W.; Grieser, F., Bubble colloidal AFM probes formed from ultrasonically generated bubbles. *Langmuir* **2008,** *24* (3), 603-605.

111. Hutter, J. L.; Bechhoefer, J., Calibration of atomic-force microscope tips. *Review of scientific instruments* **1993,** *64* (7), 1868-1873.

112. Lin, C. Y.; Slattery, J., Thinning of a liquid film as a small drop or bubble approaches a solid plane. *AIChE Journal* **1982,** *28* (1), 147-156.

113. Tabor, R. F.; Grieser, F.; Dagastine, R. R.; Chan, D. Y., Measurement and analysis of forces in bubble and droplet systems using AFM. *Journal of colloid and interface science* **2012,** *371* (1), 1-14.

114. Lin, C. Y.; Slattery, J., Thinning of a liquid film as a small drop or bubble approaches a fluid–fluid interface. *AIChE Journal* **1982,** *28* (5), 786-792.

115. Klaseboer, E.; Chevaillier, J. P.; Gourdon, C.; Masbernat, O., Film drainage between colliding drops at constant approach velocity: experiments and modeling. *Journal of colloid and interface science* **2000,** *229* (1), 274-285.

116. Carnie, S. L.; Chan, D. Y.; Lewis, C.; Manica, R.; Dagastine, R. R., Measurement of dynamical forces between deformable drops using the atomic force microscope. I. Theory. *Langmuir* **2005,** *21* (7), 2912-2922.

117. Chan, D. Y.; Klaseboer, E.; Manica, R., Theory of non-equilibrium force measurements involving deformable drops and bubbles. *Advances in colloid and interface science* **2011,** *165* (2), 70-90.

118. Chan, D.; Dagastine, R. R.; White, L. R., Forces between a rigid probe particle and a liquid interface: I. The repulsive case. *Journal of colloid and interface science* **2001,** *236* (1), 141-154.

119. Yoon, R.-H.; Flinn, D. H.; Rabinovich, Y. I., Hydrophobic Interactions between Dissimilar Surfaces. *Journal of Colloid and Interface Science* **1997,** *185* (2), 363-370.

120. Cui, X.; Shi, C.; Xie, L.; Liu, J.; Zeng, H., Probing interactions between air bubble and hydrophobic polymer surface: impact of solution salinity and interfacial nanobubbles. *Langmuir* **2016,** *32* (43), 11236-11244.

121. Shi, C.; Cui, X.; Zhang, X.; Tchoukov, P.; Liu, Q.; Encinas, N.; Paven, M.; Geyer, F.; Vollmer, D.; Xu, Z.; Butt, H.-J.; Zeng, H., Interaction between Air Bubbles and Superhydrophobic Surfaces in Aqueous Solutions. *Langmuir* **2015,** *31* (26), 7317-7327.

122. Shi, C.; Chan, D. Y. C.; Liu, Q.; Zeng, H., Probing the Hydrophobic Interaction between Air Bubbles and Partially Hydrophobic Surfaces Using Atomic Force Microscopy. *The Journal of Physical Chemistry C* **2014,** *118* (43), 25000-25008.

123. Pushkarova, R. A.; Horn, R. G., Bubble− solid interactions in water and electrolyte solutions. *Langmuir* **2008,** *24* (16), 8726-8734.

124. Manica, R.; Connor, J. N.; Dagastine, R. R.; Carnie, S. L.; Horn, R. G.; Chan, D. Y., Hydrodynamic forces involving deformable interfaces at nanometer separations. *Physics of fluids* **2008,** *20* (3), 032101.

125. Faghihnejad, A.; Zeng, H., Interaction mechanism between hydrophobic and hydrophilic surfaces: Using polystyrene and mica as a model system. *Langmuir* **2013,** *29* (40), 12443-12451.

126. Kajiyama, T.; Tanaka, K.; Takahara, A., Surface molecular motion of the monodisperse polystyrene films. *Macromolecules* **1997,** *30* (2), 280-285.

127. Satomi, N.; Takahara, A.; Kajiyama, T., Determination of surface glass transition temperature of monodisperse polystyrene based on temperature-dependent scanning viscoelasticity microscopy. *Macromolecules* **1999,** *32* (13), 4474-4476.

128. Tanaka, K.; Takahara, A.; Kajiyama, T., Film thickness dependence of the surface structure of immiscible polystyrene/poly (methyl methacrylate) blends. *Macromolecules* **1996,** *29* (9), 3232-3239.

129. Pinho, S. P.; Macedo, E. A., Solubility of NaCl, NaBr, and KCl in water, methanol, ethanol, and their mixed solvents. *Journal of Chemical & Engineering Data* **2005,** *50* (1), 29-32.

130. Zeng, H.; Maeda, N.; Chen, N.; Tirrell, M.; Israelachvili, J., Adhesion and friction of polystyrene surfaces around T g. *Macromolecules* **2006,** *39* (6), 2350-2363.

131. Blanchard, L.-P.; Hesse, J.; Malhotra, S. L., Effect of molecular weight on glass transition by differential scanning calorimetry. *Canadian Journal of Chemistry* **1974,** *52* (18), 3170-3175.

132. Abiad, M.; Carvajal, M.; Campanella, O., A review on methods and theories to describe the glass transition phenomenon: applications in food and pharmaceutical products. *Food engineering reviews* **2009,** *1* (2), 105-132.

133. Yen, T. F.; Chilingarian, G. V., *Asphaltenes and asphalts, 2: Part B*. Elsevier: 2000.

134. Maqbool, T.; Balgoa, A. T.; Fogler, H. S., Revisiting asphaltene precipitation from crude oils: A case of neglected kinetic effects. *Energy & Fuels* **2009,** *23* (7), 3681-3686.

135. Liu, D.; Li, Z.; Fu, Y.; Zhang, Y.; Gao, P.; Dai, C.; Zheng, K., Investigation on asphaltene structures during Venezuela heavy oil hydrocracking under various hydrogen pressures. *Energy & fuels* **2013,** *27* (7), 3692-3698.

136. Qi, Z.; Abedini, A.; Lele, P.; Mosavat, N.; Guerrero, A.; Sinton, D., Pore-scale analysis of condensing solvent bitumen extraction. *Fuel* **2017,** *193*, 284-293.

137. Ashoori, S.; Abedini, A.; Saboorian, H.; Nasheghi, K. Q.; Abedini, R., Mechanisms of asphaltene aggregation in toluene and heptane mixtures. *Journal of the Japan Petroleum Institute* **2009,** *52* (5), 283-287.

138. Ngai, T.; Bon, S. A., *Particle-stabilized emulsions and colloids: formation and applications*. Royal Society of Chemistry: 2014.

139. Adams, J. J., Asphaltene Adsorption, a Literature Review. *Energy & Fuels* **2014,** *28* (5), 2831-2856.

140. Rane, J. P.; Pauchard, V.; Couzis, A.; Banerjee, S., Interfacial rheology of asphaltenes at oil–water interfaces and interpretation of the equation of state. *Langmuir* **2013,** *29* (15), 4750-4759.

141. Langevin, D.; Argillier, J.-F., Interfacial behavior of asphaltenes. *Advances in colloid and interface science* **2016,** *233*, 83-93.

142. Zhang, J.; Li, C.; Shi, L.; Xia, X.; Yang, F.; Sun, G., The formation and aggregation of hydrate in W/O emulsion containing different compositions: A review. *Chemical Engineering Journal* **2022**, 136800.

143. Liu, J.; Xu, Z.; Masliyah, J., Interaction between bitumen and fines in oil sands extraction system: Implication to bitumen recovery. *The Canadian Journal of Chemical Engineering* **2004,** *82* (4), 655-666.

144. Rao, S. R., *Surface chemistry of froth flotation: Volume 1: Fundamentals*. Springer Science & Business Media: 2013.

145. Feng, L.; Zhang, Z.; Mai, Z.; Ma, Y.; Liu, B.; Jiang, L.; Zhu, D., A super-hydrophobic and super-oleophilic coating mesh film for the separation of oil and water. *Angewandte Chemie* **2004,** *116* (15), 2046-2048.

146. Rane, J. P.; Harbottle, D.; Pauchard, V.; Couzis, A.; Banerjee, S., Adsorption kinetics of asphaltenes at the oil–water interface and nanoaggregation in the bulk. *Langmuir* **2012,** *28* (26), 9986-9995.

147. Yarranton, H. W.; Alboudwarej, H.; Jakher, R., Investigation of asphaltene association with vapor pressure osmometry and interfacial tension measurements. *Industrial & engineering chemistry research* **2000,** *39* (8), 2916-2924.

148. Das, S.; Thundat, T.; Mitra, S. K., Analytical model for zeta potential of asphaltene. *Fuel* **2013,** *108*, 543-549.

149. Sztukowski, D. M.; Jafari, M.; Alboudwarej, H.; Yarranton, H. W., Asphaltene self-association and water-in-hydrocarbon emulsions. *Journal of colloid and interface science* **2003,** *265* (1), 179-186.

150. Li, L.; Jin, X.; Chen, J.; Wang, Z.; Wu, Y.; Zhao, M.; Dai, C., Anionic surfactant with enhanced interfacial wettability control capability for residual oil development. *Colloids and Surfaces A: Physicochemical and Engineering Aspects* **2022,** *655*, 130073.

151. Liu, J.; Zhang, L.; Xu, Z.; Masliyah, J., Colloidal interactions between asphaltene surfaces in aqueous solutions. *Langmuir* **2006,** *22* (4), 1485-1492.

152. Wu, X.; Laroche, I.; Masliyah, J.; Czarnecki, J.; Dabros, T., Applications of colloidal force measurements using a microcollider apparatus to oil sand studies. *Colloids and Surfaces A: Physicochemical and Engineering Aspects* **2000,** *174* (1-2), 133-146.

153. Rocha, J.; Baydak, E.; Yarranton, H.; Sztukowski, D.; Ali-Marcano, V.; Gong, L.; Shi, C.; Zeng, H., Role of aqueous phase chemistry, interfacial film properties, and surface coverage in stabilizing water-in-bitumen emulsions. *Energy & Fuels* **2016,** *30* (7), 5240-5252.

154. Shi, L.; Li, Z.; Yu, L.; Jia, H.; Zheng, L., Effects of surfactants and lipids on the preparation of solid lipid nanoparticles using double emulsion method. *Journal of dispersion science and technology* **2011,** *32* (2), 254-259.

155. Wei, Z.; Sun, W.; Wang, P.; Liu, D.; Han, H., A novel metal–organic complex surfactant for high-efficiency mineral flotation. *Chemical Engineering Journal* **2021,** *426*, 130853.

156. Mao, X.; Zhao, Z.; Yang, D.; Qiao, C.; Tan, J.; Liu, Q.; Tang, T.; Zhang, H.; Zeng, H., Facile and scalable surface functionalization approach with small silane molecules for oil/water separation and demulsification of surfactant/asphaltenes-stabilized emulsions. *Separation and Purification Technology* **2022,** *285*, 120382.

157. Wang, S.; Liu, J.; Zhang, L.; Xu, Z.; Masliyah, J., Colloidal interactions between asphaltene surfaces in toluene. *Energy & fuels* **2009,** *23* (2), 862-869.

158. Qiao, C.; Wang, D.; Zhao, Z.; Yang, W.; Wu, F.; Chen, H.; Yin, T.; Zhang, L.; Liu, Q.; Yang, D., Bench-scale oil fouling/antifouling tests under high temperature and high pressure conditions and the underlying interfacial interaction mechanisms. *Fuel* **2022,** *314*, 122720.

159. Harbottle, D.; Chen, Q.; Moorthy, K.; Wang, L.; Xu, S.; Liu, Q.; Sjoblom, J.; Xu, Z., Problematic stabilizing films in petroleum emulsions: Shear rheological response of viscoelastic asphaltene films and the effect on drop coalescence. *Langmuir* **2014,** *30* (23), 6730-6738.

160. Huang, J.; Stoyanov, S. R.; Zeng, H., A comparison study on adsorption and interaction behaviors of diluted bitumen and conventional crude oil on model mineral surface. *Fuel* **2019,** *253*, 383-391.

161. Huang, J.; Yan, B.; Faghihnejad, A.; Xu, H.; Zeng, H., Understanding nanorheology and surface forces of confined thin films. *Korea-Australia rheology journal* **2014,** *26* (1), 3-14.

162. Vakarelski, I. U.; Li, E. Q.; Thoroddsen, S. T., Soft colloidal probes for AFM force measurements between water droplets in oil. *Colloids and Surfaces A: Physicochemical and Engineering Aspects* **2014,** *462*, 259-263.

163. Tabor, R. F.; Lockie, H.; Mair, D.; Manica, R.; Chan, D. Y.; Grieser, F.; Dagastine, R. R., Combined AFM− confocal microscopy of oil droplets: Absolute separations and forces in nanofilms. *The Journal of Physical Chemistry Letters* **2011,** *2* (9), 961-965.

164. Zhang, S.; Zhang, L.; Lu, X.; Shi, C.; Tang, T.; Wang, X.; Huang, Q.; Zeng, H., Adsorption kinetics of asphaltenes at oil/water interface: Effects of concentration and temperature. *Fuel* **2018,** *212*, 387-394.

165. Russel, W. B.; Russel, W.; Saville, D. A.; Schowalter, W. R., *Colloidal dispersions*. Cambridge university press: 1991.

166. Hogg, R.; Healy, T. W.; Fuerstenau, D. W., Mutual coagulation of colloidal dispersions. *Transactions of the Faraday Society* **1966,** *62*, 1638-1651.

167. Stankovich, J.; Carnie, S. L., Electrical Double Layer Interaction between Dissimilar Spherical Colloidal Particles and between a Sphere and a Plate: Nonlinear Poisson− Boltzmann Theory. *Langmuir* **1996,** *12* (6), 1453-1461.

168. Yang, C.; Dabros, T.; Li, D.; Czarnecki, J.; Masliyah, J. H., Measurement of the zeta potential of gas bubbles in aqueous solutions by microelectrophoresis method. *Journal of Colloid and Interface Science* **2001,** *243* (1), 128-135.

169. Mullins, O. C., The modified Yen model. *Energy & Fuels* **2010,** *24* (4), 2179-2207.

170. Mullins, O. C.; Sabbah, H.; Eyssautier, J.; Pomerantz, A. E.; Barré, L.; Andrews, A. B.; Ruiz-Morales, Y.; Mostowfi, F.; McFarlane, R.; Goual, L., Advances in asphaltene science and the Yen–Mullins model. *Energy & Fuels* **2012,** *26* (7), 3986-4003.

171. Lata, S.; Singh, K.; Ahlawat, S., A study of dielectric properties and refractive indices of aniline+ benzene,+ toluene,+ o-xylene, and+ p-xylene at 298.15 K. *Journal of Molecular Liquids* **2009,** *147* (3), 191-197.

172. Fuerstenau, M. C.; Jameson, G. J.; Yoon, R.-H., *Froth flotation: a century of innovation*. SME: 2007.

173. Dickinson, E.; Ettelaie, R.; Kostakis, T.; Murray, B. S., Factors controlling the formation and stability of air bubbles stabilized by partially hydrophobic silica nanoparticles. *Langmuir* **2004,** *20* (20), 8517-8525.

174. Safouane, M.; Langevin, D.; Binks, B., Effect of particle hydrophobicity on the properties of silica particle layers at the air− water interface. *Langmuir* **2007,** *23* (23), 11546-11553.

175. Lindner, J. R., Microbubbles in medical imaging: current applications and future directions. *Nature reviews Drug discovery* **2004,** *3* (6), 527-533.

176. Prentice, P.; Cuschieri, A.; Dholakia, K.; Prausnitz, M.; Campbell, P., Membrane disruption by optically controlled microbubble cavitation. *Nature physics* **2005,** *1* (2), 107-110.

177. Yec, C. C.; Zeng, H. C., Nanobubbles within a microbubble: synthesis and self-assembly of hollow manganese silicate and its metal-doped derivatives. *ACS nano* **2014,** *8* (6), 6407-6416.

178. Liu, G.; Craig, V. S., Improved cleaning of hydrophilic protein-coated surfaces using the combination of Nanobubbles and SDS. *ACS Appl Mater Interfaces* **2009,** *1* (2), 481-7.

179. Meng, P.; Deng, S.; Lu, X.; Du, Z.; Wang, B.; Huang, J.; Wang, Y.; Yu, G.; Xing, B., Role of air bubbles overlooked in the adsorption of perfluorooctanesulfonate on hydrophobic carbonaceous adsorbents. *Environmental science & technology* **2014,** *48* (23), 13785-13792.

180. Ferrara, K.; Pollard, R.; Borden, M., Ultrasound microbubble contrast agents: fundamentals and application to gene and drug delivery. *Annu. Rev. Biomed. Eng.* **2007,** *9*, 415-447.

181. Ralston, J.; Fornasiero, D.; Hayes, R., Bubble–particle attachment and detachment in flotation. *International Journal of Mineral Processing* **1999,** *56* (1-4), 133-164.

182. Horn, R. G.; Asadullah, M.; Connor, J. N., Thin film drainage: hydrodynamic and disjoining pressures determined from experimental measurements of the shape of a fluid drop approaching a solid wall. *Langmuir* **2006,** *22* (6), 2610-2619.

183. Tabor, R. F.; Chan, D. Y. C.; Grieser, F.; Dagastine, R. R., Structural Forces in Soft Matter Systems. *The Journal of Physical Chemistry Letters* **2011,** *2* (5), 434-437.

184. Gafonova, O. V.; Yarranton, H. W., The Stabilization of Water-in-Hydrocarbon Emulsions by Asphaltenes and Resins. *Journal of Colloid and Interface Science* **2001,** *241* (2), 469-478.

185. Yarranton, H. W.; Hussein, H.; Masliyah, J. H., Water-in-hydrocarbon emulsions stabilized by asphaltenes at low concentrations. *Journal of colloid and interface science* **2000,** *228* (1), 52-63.

186. Wu, X.; Czarnecki, J.; Hamza, N.; Masliyah, J., Interaction forces between bitumen droplets in water. *Langmuir* **1999,** *15* (16), 5244-5250.

187. Legrand, J.; Chamerois, M.; Placin, F.; Poirier, J.; Bibette, J.; Leal-Calderon, F., Solid colloidal particles inducing coalescence in bitumen-in-water emulsions. *Langmuir* **2005,** *21* (1), 64-70.

188. Alcantar, N.; Israelachvili, J.; Boles, J., Forces and ionic transport between mica surfaces: Implications for pressure solution. *Geochimica et Cosmochimica acta* **2003,** *67* (7), 1289-1304.

189. Tian, Y.; Pesika, N.; Zeng, H.; Rosenberg, K.; Zhao, B.; McGuiggan, P.; Autumn, K.; Israelachvili, J., Adhesion and friction in gecko toe attachment and detachment. *Proceedings of the National Academy of Sciences* **2006,** *103* (51), 19320-19325.

190. Kristiansen, K.; Stock, P.; Baimpos, T.; Raman, S.; Harada, J. K.; Israelachvili, J. N.; Valtiner, M., Influence of molecular dipole orientations on long-range exponential interaction forces at hydrophobic contacts in aqueous solutions. *ACS nano* **2014,** *8* (10), 10870-10877.

191. Van Oss, C. J., *Interfacial forces in aqueous media*. CRC press: 2006.

192. Van Oss, C., Acid—base interfacial interactions in aqueous media. *Colloids and Surfaces A: Physicochemical and Engineering Aspects* **1993,** *78*, 1-49.

193. Tabor, R. F.; Grieser, F.; Dagastine, R. R.; Chan, D. Y., Measurement and analysis of forces in bubble and droplet systems using AFM. *J. Colloid Interface Sci.* **2012,** *371* (1), 1-14.

194. Chan, D. Y.; Klaseboer, E.; Manica, R., Theory of non-equilibrium force measurements involving deformable drops and bubbles. *Adv. Colloid Interface Sci.* **2011,** *165* (2), 70-90.

195. Chan, D. Y.; Dagastine, R. R.; White, L. R., Forces between a Rigid Probe Particle and a Liquid Interface. *J. Colloid Interface Sci.* **2001,** *236* (1), 141-154.

196. Tsao, Y.; Evans, D.; Wennerstrom, H., Long-range attractive force between hydrophobic surfaces observed by atomic force microscopy. *Science* **1993,** *262* (5133), 547-550.

197. Kalita, D.; Kaushik, N.; Mahanta, C. L., Physicochemical, morphological, thermal and IR spectral changes in the properties of waxy rice starch modified with vinyl acetate. *Journal of food science and technology* **2014,** *51* (10), 2790-2796.

198. Wu, X.; Dabros, T.; Czarnecki, J., Determining the colloidal forces between bitumen droplets in water using the hydrodynamic force balance technique. *Langmuir* **1999,** *15* (25), 8706-8713.

199. Zhou, J.; Li, H.; Zhao, L.; Chow, R., Role of mineral flotation technology in improving bitumen extraction from mined Athabasca oil sands: I. Flotation chemistry of water-based oil sand extraction. *The Canadian Journal of Chemical Engineering* **2018,** *96* (9), 1986-1999.

200. Israelachvili, J.; Pashley, R., The hydrophobic interaction is long range, decaying exponentially with distance. *Nature* **1982,** *300* (5890), 341-2.

201. Vargha-Butler, E.; Potoczny, Z.; Zubovits, T.; Budziak, C.; Neumann, A., Surface tension of bitumen from contact angle measurements on films of bitumen. *Energy & fuels* **1988,** *2* (5), 653-656.